Polymer microfluidic device for high-throughput single-cell encapsulation, lysis, and biological assay

by

Timothy Peter Brackbill

A dissertation submitted in partial satisfaction of the
requirements for the degree of
Doctor of Philosophy

in

Engineering - Mechanical Engineering

in the

GRADUATE DIVISION
of the
UNIVERSITY OF CALIFORNIA, BERKELEY

Committee in charge:
Professor Albert P. Pisano, Chair
Professor Liwei Lin
Professor Amy Herr

Fall 2012

Polymer microfluidic device for high-throughput single-cell encapsulation, lysis, and biological assay

Timothy Peter Brackbill

Abstract

Polymer microfluidic device for high-throughput single-cell encapsulation, lysis, and biological assay

by

Timothy Peter Brackbill

Doctor of Philosophy in Engineering - Mechanical Engineering

University of California, Berkeley

Professor Albert P. Pisano, Chair

Single cell analysis is the present and future of biological research. It's becoming clear that sub-populations of cells within a larger group can often be the culprit for diseases or malfunctions. In this work we aim to provide a tool that allows biological researchers to better analyze single cells within cell populations by removing the barrier to observing analytes contained within the cell's membrane. By providing physical access to the intracellular compounds in a single cell, we can analyze individual cells for levels of analytes that were previously only available through bulk measurements of a lysed cell population. The technique is similar to flow cytometry, but we will use droplets as a physical analog to cells in a flow cytometer-type configuration. This distinction allows for lysis of a single cell within a droplet and prevents diffusion of internal components outside of the droplet's barrier. Analysis of analyte levels is accomplished with fluorescence labeling and laser based querying of the fluorescence concentration. This work is accomplished through use of a plastic microfluidic network.

Contents

List of Figures

List of Tables

Acknowledgments

I'd like to thank my advisor, Professor Albert P. Pisano, for seeing me through this work. It was a long and rutted road and without his help, guidance, and political prowess I probably would not have seen it through. Many thanks to his understanding and acceptance of his student's differing styles.

Equally importantly, I'd like to thank Dr. Frans Kuypers at the Research Center of the Children's Hospital of Oakland (CHORI). Without his keen oversight on biological issues I would be fabricating devices with no cause. In his lab, a special thanks goes to Sandra Larkin, for tolerating and guiding an engineer through biological protocols.

Gratitude is due to Paul Lum of the Berkeley Biomolecular Nanotechnology Center, and Mick Franssen and Gordon Long of the Berkeley ME Student shop. These exemplary staff members provide exceptional student facilities well beyond the call of their jobs and make time spent there genuinely pleasant.

I'd also like to thank all the folks in the Berkeley Micromechancial Analysis and Design (BMAD) and Kuypers Lab at CHORI for shared time and thoughtful discussions. Special thanks to Dr. Won Chul Lee for previous work performed and insightful guidance on the device design.

Thanks to the NSF CBET program for providing current and hopefully future funding for this work.

Chapter 1

Introduction

1.1 Single cell analysis in Biology

The analysis of single cells is of interest in most current biological research. Techniques prior to flow cytometry relied upon testing large populations of cells to determine only average levels of analytes of interest. However, much data about individual cells, sub-populations of cells, and the mechanisms behind any anomalous populations are lost. Since the single cell is the fundamental building block of life, this is where the next crop of research and advances will originate.

1.1.1 Stochastic Differences in Cell Populations

It is convenient to picture a population of cells as many repetitions of the exact same fundamental unit. This is an overly simple model of many cells as there are significant variations between the individual cells inside of that population. One example of this variation is that stochasticity of genetic transcription has been shown to arise even in otherwise equal environments [4]. This stochasticity in expression is shown to be detrimental to cell regulation from fluctuating protein levels, but has the benefit of ensuring that there is variation between cells of the same type. This variation is crucial to natural selection, but also manifests selectively as low variation in potentially lethal changes and more so in non-lethal variation within the cell [5].

1.1.2 Survival of Microorganisms

In microorganisms, phenotypical variation between cells can ensure bacterial survival through times of stress without the need for any genetic mutations [6]. Due to the prevalence of cells with different expression levels of certain genes, some of the variations may live through stress cycles even when the majority of the cells have been eliminated. The prevalence of this variation can also allow a phenotypically heterogeneous population of cells to grow faster than a phenotypically optimized homogeneous population due to the naturally prevalent cycle of stresses on the population [7]. It is also postulated that a phenotype variation is responsible for "persistor" cells that provide for antibiotic resistance in bacteria [8; 9]. While the antibiotic eliminates most of the infectious cells, some low-growth persistor cells are able to withstand the attack. These persistors then further procreate and return both persistor and normal cells.

1.1.3 Disease Progression and Stem Cell differentiation

In higher organisms, variation between individual cells provides a key role in development of cells and the progression of diseases. In flies, random variation amongst stem cells determines where bristles will form on the fly's exterior, while other signaling forms empty areas around them [10]. Even more telling, in this type of cell population are hemopoietic stem cells; research [11; 12; 13] indicates that hematopoietic stem cells are primed for any of the lineages that the cell could be differentiated into. It is only subtle stochastic differences between expression in each individual stem cell that determines the ultimate fate of these cells.

Many recent studies are starting to shed light on the differences between cells within a population [14]. The analytes of interest and cell lines are numerous, but the current studies are mainly limited to differences that can be quantified by looking just at the surface of the cells with flow cytometry or by looking at cell viability. No technique exists for single cell analysis of other analytes in an efficient, high-throughput way. Some examples of these studies will be illustrated here. Some look at epigenetic variation of antigen 43 expressed on the outside surface of Escherichia coli bacteria [15; 16] as they are exposed to environmental stimuli. Others look at the expression of the multiple antigens on the surface of Trypanosoma brucei, responsible for African Sleeping

Sickness [17; 18]. The antigens expressed on the surface vary by stage of infection, and the cell only expresses certain ones at a time, leading to heterogeneity by disease progression. Plasmodium falciparum, responsible for malaria, also has population heterogeneity of the *var* antigen expressed on the outside of the cell [19; 20]. This antigen is of pharmaceutilogical interest in making an anti-malarial drug, and understanding why this variation is present is key to that process. What is interesting in all of these studies is that the mechanistic hypothesis of what is occurring inside of the cell is poorly understood. If a process such as ours existed to be able to correlate levels of analyte inside of the cell with expression on the exterior, much more mechanistic understanding of the full process would be available.

1.1.4 Importance of High Throughput Study

It is apparent that single cell analysis techniques will be vastly useful to study these and future trends in organisms. It is no longer an option to take an "average" value of a population of cells, as too much information about the individuals is lost. As genomic and disease pathway research continues, a new set of tools must be developed to query analytes in single cells. There are currently techniques for measuring certain parameters in single cells, but most all have shortcomings in various ways. Flow cytometry allows high throughput analysis, but is limited mainly to the exterior of the cell if no membrane permeable marker is available. It also only provides a single view of the cell with no temporal variation. Automated microscopy can add temporal and spatial resolution of cells, but is again limited to the exterior of the cell. Microwell techniques provide spatial and temporal analysis of cells, and also limit diffusion of contents and molecules from and to the cell. Finally for most intracellular measurements, we are mainly limited to bulk analysis of many lysed cells if a membrane permeable marker is not available. These techniques will be presented in the following sections along with some of their main shortcomings.

1.2 Available Cell Assay Methods

1.2.1 Batch Intracellular Analysis

This method for cellular analysis is fairly crude, and offers only cursory information about the cell population. A lysis buffer is added to a suspension of cells to form a cell lysate. During this step, the membranes of the cells are dissolved or broken and the contents released into the surrounding buffer. Assay kits are then used to determine the levels of the analyte of interest in the buffer. These assays can be absorbance, colorimetric, or fluorescent reporting based. To get the amount of analyte per cell, a crude average is performed by knowing the number of cells in the initial solution (by concentration) and the ending concentration of the solution. This method utilizes an implicit assumption that each cell in the population has exactly the same amount of analyte. This can be false in populations with differently aged cells, or populations where certain cells have mutations or diseases.

1.2.2 Flow Cytometry

Technology

Cytometry is a term for measuring properties of individual cells. This began with simple counting of cells via Coulter counting, but has since evolved to be able to measure many different cell properties. The first flow cytometer (FCM) [21] was designed to use the Coulter principle to determine the volume of a cell, encapsulate the cell in a droplet, then sort the cells based on volume. This was accomplished by charging droplets that exceeded a threshold for size, and using electrostatic deflection to separate charged and uncharged droplets. Human and mouse erythrocytes were separated using this technique. Further work added fluorescent imaging to this technique [22] and from this the first commercial flow cytometers were created.

In its current iteration, a flow cytometer consists of some main components. Most have a sheath fluid flowing around the stream of cells to hydrodynamically center the cells in the optical path of the channel. A laser is directed at the center of a channel and cells pass through its path. During the time the cell passes through, several concurrent quantitative measurements are taken. A forward scatter sensor, which allows the size of the cell to be determined, is placed opposing the laser. Side scatter sensors are placed at angles away from

the path of the laser, and allow complexity of the cell to be determined. As a cell contains more features, such as nucleii, mitochondria, and other organelles, the side scatter profile will change. Finally, several fluorescence detectors and associated filters are present to detect any fluorescent probes that have been attached to the cell. Different cytometers have different numbers of color channels available for sampling, so many different probes can be queried simultaneously.

Once the cell is analyzed, it is also possible to sort cells based on one of its quantities. This is commonly referred to as Fluorescence Activated Cell Sorting (FACS). Once the cells have passed by the laser, the fluid is broken up into droplets and the droplets are charged based on the data from the laser. Breakup is usually mediated by a vibrating element that forms an instability in the jet of buffer. By modulating the electric field once the cells are broken into droplets the cells can be sorted based on the charge that was applied for further analysis.

Strengths and Limits

Flow cytometry allows for very high throughput testing. Commercial tools can process between three and ten thousand events per second. In very short amounts of time, statistically significant populations of cells can be individually analyzed for markers. The limits of detection are also very good, generally measured as Mean Equivalent Soluble Flurophores (MESF) [23]. Quantification of the absolute amounts of fluorescent marker is somewhat ambiguous, thus requiring this measurement. It relates the amount of fluorescence detected to a quantity of that same fluorophore in a clean solution where dispersion and adsorption of fluorescent is not an issue. Typical practical ratings for this sensitivity are 300-600 MESF depending on the dye used (FITC, PE, APC, *etc*). Flow cytometry also has the ability to measure size and complexity of the passing cells. Because of the coherent light striking the cell, forward scattered photons can reconstruct the size of the cell. Side scattered light is an indication of the complexity of the cell, as more light scattered to the side indicates the presence of organelles and other structures.

While an extremely useful method whose applicability is still rapidly growing, FCM has several limitations. It offers a single temporal location, and activity inside of the cell cannot be correlated over time. While not an inherent drawback, other methods where the cell is immobilized in a reaction vessel can offer temporal data on enzyme activity and show insight into time variant

cellular functions.

FCM is also limited to a specific set of analytes. There are three main types of cellular analytes that FCM can successfully report on. The first type is for analytes present on the membrane of the cell. Examples of these are glycophorins that cross the structure of the cell and protrude outside of the cell membrane. Binding a marker to this type of molecule is simple and requires no complicated procedures. The second type is quantifiable bioreporters expressed inside of a genetically modified organism. If a biological process creates analytes as a function of its progression, the cell can be engineered to make fluorescently modified versions of this analyte. Without adding markers, these events can be reported. The third type requires gaining access to the intracellular region, either by poration or by a dye that is capable of diffusing through the cell membrane. Poration can be accomplished by application of a small AC electric field to generate small pores in the membrane of cells. These temporary pores can allow markers that are in solution with the cells to diffuse into the cells and bind with targets of interest. Other markers are able to simply diffuse across the cell membrane, accomplishing the same function.

1.2.3 Automated Microscopy

Automated microscopy is becoming a more viable single cell analysis method. Previously, if single cells were to be analyzed individually the counts were low due to the complexity entailed. With more acceptable performance from automated image analysis, microscope images from fluorescent microscopes can now be used with the same probe methods of FCM to get cell data. Purpose built tools are now available to automatically pan over areas of cell culture to get large amounts of cell data.

The benefits of these types of systems are that temporal data on cells is now available. Because the cells are in fixed locations, the same cell can be queried at different points in time to observe its progression. Combined with the probes and methods of FCM, this offers a convenient way to collect more data. The drawback of this method, in addition to mechanical complexity of the scanning system, is that the throughput is fairly low. Because full images must be taken, the process is limited by the amount of time that the shutter needs to remain open on a section of cells to receive enough light for an acceptable signal to noise ratio. As a result of this lower throughput, this method is more often used for screening cells for responses to large amounts of test compounds.

1.3 Research State of the Art of MEMS Cell Encapsulation

With the bloom in digital microfluidics, several researchers have attempted to create single cell encapsulation and analysis microfluidic assays. Common failing points of these systems tend to be low throughput or reliance on overly complex encapsulation schemes. A summary of relevant works in this space is found in Table 1.1.

For encapsulation of cells in droplets, several methods are used in the literature. The first and by far most simple is to just accept inherent stochasticity of cells in a suspension in a generic droplet generator [27; 28; 30]. In these generators, droplets can contain zero to four cells, all formed during an equivalent droplet breakup process. This variation is uncontrollable and during further analysis the results will be skewed by the excess number of cells in each drop. The devices tend to function at low capillary numbers due to high interfacial tension. Since stochasticity is accepted, little work is done to tailor the breakup of the cell containing jet.

An improvement on the stochastic cell encapsulation device is partial control over how many cells enter a droplet. One such implementation is by Zhang [31]. In this device, the viscosity of the cell containing suspension is increased by the addition of water soluble polyethylene glycol (PEG). Increasing the viscosity increases the inertial centering and separation phenomenon of particles, and with a sufficiently long inlet channel for the cells to traverse they will get to the droplet generation point evenly separated. Once droplet formation is timed to this progression, each drop should theoretically contain one droplet. However, these two phenemenon are not experimentally shown in the work and it is apparent that difficulties will be encountered between timing the separation and droplet generation.

More accurate droplet cell count can be achieved with external control of the chips, at the expense of throughput. Two such studies have been performed. Wu [25] shows that by external actuation of physical valves, containers for chip analysis can be formed by deforming PDMS. Unfortunately the throughput is very low (1 cell/hr) and the chip can only be used once before disposal is required. He [26] generates cell containing droplets by using optical tweezers to manipulate cells to the droplet breakup. This work does not elaborate on what is done with the excess droplets, but by manipulating a single cell it is

Table 1.1: Summary of experimental cell encapsulation literature. (A) indicates assumed rate of encapsulation.

Publication	**Encaps./ Single Cell**	**Rate** cells/min	**Analysis Method** -	**Lysis** -	**Summary** -
McClain [24]	No/-	7−12	Electrophoresis	AC Field	Lyse cell at separation channel. Fouling issues.
Wu [25]	Physical/-	0.016	Electrophoresis	Chemical	Very complicated. 1 cell per chip
He [26]	Yes/Yes	0.5 (A)[1]	Fluorescent binding	Laser	Extremely slow (optical tweezers)
Choi [27]	Yes/No	2 (A)	Not Reported	None	Illustrates encapsulation in a hydrogel
Shintaku [28]	Yes/No	2 (A)	Not Reported	None	Illustrates encapsulation in a hydrogel
Chabert [29]	Yes/Yes	72	None	None	Good encapsulation and sorting, only large cells possible
Quinto-Su [2]	No/-	0.5 (A)	Fluorescent binding	Laser	Accurate laser positioning vital, rapid diffusion of contents.
Konry [30]	Yes/No	Low	Fluorescent binding	None	Stochastic/poor cell encapsulation, long incubation
Zhang [31]	Yes/Partial	500 (A)	None	None	Inertial effects for cell separation, not demonstrated

[1] Rate not explicitly given, but can be approximated from information in the work

simple to make a cell containing droplet. The throughput is highly affected by this, and manual control of the process is required.

Finally, one approach allows for a single cell encapsulation to be both implemented at high throughputs and controlled passively by hydrodynamics. Chabert [29] utilizes a high capillary number flow regime to generate cell containing droplets (large) and empty droplets (small) in a high shear rate channel. This channel allows for sorting between positive and negative droplets hydrodynamically. In this work, very large cancerous cells were used, but the approach can be modified for more useful cells to be encapsulated. They did not perform any further tasks on the cells once encapsulated.

1.4 Thesis Outline and Description

The main goal of this thesis is to design, fabricate, and test a device that is capable of encapsulating, sorting, lysing, and characterizing any aspect of each cell in a population of cells. This extends flow cytometry to analytes that were not previously accessible. This thesis will also elucidate improved microfluidic device fabrication, testing, fluidic system characterization, and surfactant design. The final experimental results will show encapsulation of single cells and subsequent lysis. Much of the details presented in this work are those that are ignored or not sufficiently characterized in other similar microfluidic works. Through the details, improved design is possible in faster iterations. The fabrication is novel and extremely robust for fast and simple chip fabrication and testing that breaks conventional PDMS limitations.

1.4.1 Issues with State of the Art

No current experimental device, summarized in Table 1.1, presents a complete and useful tool for high throughput studies of cells. The modes of failure are many, including prevention of fouling, non-specific cell encapsulation, device complexity, or manual user interaction. This device will solve these issues, and the completed device is nearer to commercial viability than most other research-scale microfluidic devices.

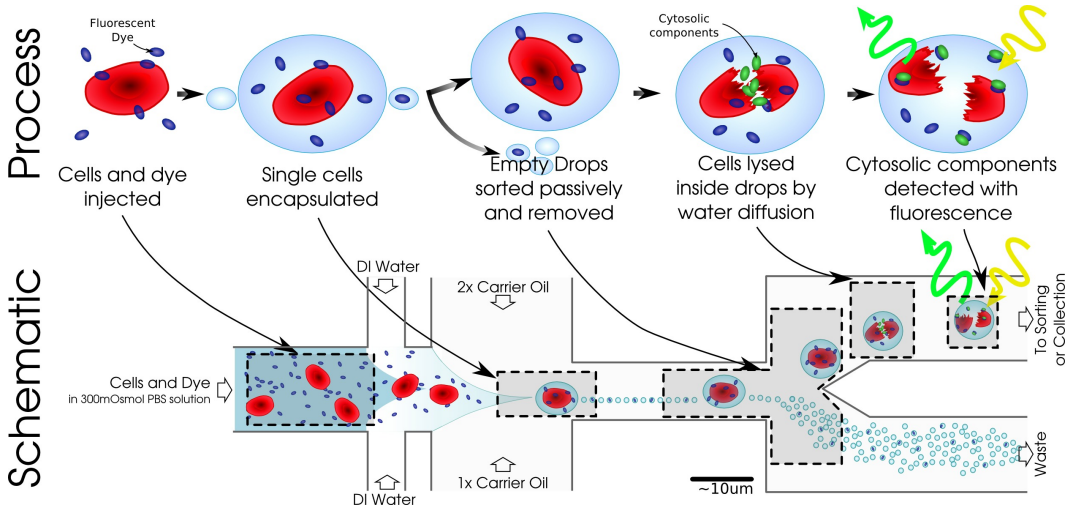

Figure 1.1: Process and schematic overview of the devices created in this work.

1.4.2 Capabilities of our Device

The devices themselves are small microfluidic networks that possess a footprint of 17 mm x 8 mm on a plastic film of approximately 0.5 mm thickness. These devices can be created by embossing of features and lamination of a capping surface in a high throughput manner. A buffer containing cells and a dye for an analyte inside of the cell is brought together with a lysing solution, and then this solution is broken into droplets in a flow focusing geometry. After the addition of this lysing buffer, the cells have a short time constant before they will break open inside the droplets that have been formed. Due to careful and exhaustive effort in tailoring and characterization of this focusing breakup, cell containing droplets are a larger size than those droplets containing no cell. This size difference is exploited along with a high shear region to sort between empty and cell-containing droplets. Once empty droplets are removed from the stream of cell containing droplets, lysis of the cells will occur in the drops. This allows internal cellular components to combine with the dyes that are also encapsulated in the drops. The dyes become fluorescent when combined with the analyte of interest, and a query of the droplets will then show the amount of that analyte that was present in each cell. This process is summarized in Figure 1.1

The shortcomings of previous devices in Table 1.1 are addressed in the current design. The channels themselves are fabricated in hydrophobic thermoplastics that have much lower porosity than PDMS. This means that fewer proteins and dyes will adsorb into the channel surfaces. To further prevent adsorption of hydrophobic molecules, the cells are encapsulated in droplets during their handling and lysis. Device complexity is reduced but specific cell encapsulation is still accomplished by using a passive sorting mechanism with no outside interaction. The fabrication method is able to produce channels of nearly an order of magnitude smaller size than comparable works without fouling or delamination issues. This allows us to work with smaller and more deformable cells (human erythrocytes) than other devices are able to handle.

1.4.3 Outline of this Thesis

This thesis is organized into three chapters. In Chapter 2 a better way to fabricate and test thermoplastic devices is presented. This includes the design of channel networks on chip, and all of the fabrication and sealing steps. Chapter 3 is a fluidic overview of the relevant phenomena to making this a functional chip. This includes characterization of the fluidic system, analysis of the breakup, and analysis of the droplet sorting. In Chapter 4 experimental results from the functioning devices are presented.

Chapter 2

Design

2.1 Specifications

Several specifications must be met to make this a successful device. They are summarized in Table 2.1 but the specifications and their importance will be discussed here. The main design specifications can be broken into three different categories: Fluidic, biological, and mechanical.

The main fluidic specification of importance is the throughput of this device in number of cells processed per second. To compete with or complement a flow cytometer this throughput has to be sufficiently high to give biologists large sample sizes in less than an hour. A reasonable throughput for a single channel can be set at 50 cells s^{-1}. Higher throughputs can be accomplished by either increasing the volume fraction of red blood cells in the sample (hematocrit) or by operating several of these devices in parallel.

Several fluidic specifications are related to feasibility of compressed air drive. The devices are shown to seal to pressures exceeding 1.5 MPa and this makes the pressure handling capabilities of the devices orders of magnitude larger than a safe pressure supply system. Since biohazardous liquids are used, care must be taken to prevent the aerosolization of fluids in the event of a leak which drives toward minimizing the supply pressure. The design point of the device's pressure drop is chosen at 60.4 kPa. This corresponds to an overall chip resistance of 620 Pa hr μL^{-1} at an oil flow rate of 32 μL hr^{-1}. The flow rate of the device is also the main factor to change when tailoring the capillary number of generation with a fixed interfacial tension.

Table 2.1: Design constraints along with the design point of important specifications of the devices. It is important to note that the experimental values of these parameters will vary based on the operating pressure and specific conditions used in the individual test.

Specification	**Units**	**Constraint Type**	**Constraint Value**	**Design Value**
		Fluidics		
Throughput	cells s^{-1}	Order	50	90
Device Pressure Drop	kPa	Max	1,500	60.4
Total Resistance (Carrier)	Pa hr μL^{-1}	Max	7,890	1,150
Carrier Flow Rate	μL hr^{-1}	Max	180	50
Carrier to sample flow ratio	-	Min	20	80.3
Generation Capillary number	-	Min	0.25	6.05
Eq. Interfacial Tension (IFT)	mN m^{-1}	Max	4.3	0.8
Carrier dynamic viscosity	mPa·s	Max	100	74.8
Lysis buffer to sample flow ratio	-	Min	2.3	3.0
Final droplet osmolarity	mOsmol	Max	130	75
		Biological		
Erythrocyte diameter	μm	Average	7.2	-
Sustained shear rate on cells	Pa	Max	300	104
Erythrocyte storage time	week	Max	1	-
Buffer osmolarity	mOsmol	Target	300	-
Droplet residence time (to lysis)	s	Min	3	4.1
Hematocrit	%	Max	15	5
		Mechanical		
Device footprint	mm^2	Max	20x10	15.8x7.8
Pressure supply	kPa	Max	275	103
Pressure supply accuracy	%	Max	1	0.1
Feature size	μm	Min	8	15
Feature depth	μm	Min	8	15
Feature aspect ratio	-	Max	1	1
Well Volume	μL	Min	20	25

At the point of droplet generation and cell encapsulation, the critical parameters for design are the carrier to sample flow rate ratio, capillary number, and interfacial tension between the two phases. Dimensional analysis and experimentation yields a minimum carrier to sample flow rate ratio of 20 and minimum capillary number of 0.25 for generating sufficiently small empty droplets without the presence of a cell. The flow rate ratio can be adjusted during experimentation by the presence of two precision air regulators, one on the aqueous phase and one on the carrier phase. The difference designed into the device is approximately 3 kPa and arises from the difficulty of creating high fluidic resistance on the aqueous inlet lines. The interfacial tension at equilibrium has a maximum value of 5 mN m^{-1} set by experimentation. If this value is allowed to increase the differentiation in size between empty and cell-containing droplets is too small to sort between since the cells are not stiff enough to cause a disturbance in the phase boundary.

The lysis buffer to sample flow ratio will determine the final osmolarity of the buffer that the cells are encapsulated into drops with, and thus drive the lysis of the cells. Since the initial buffer the cells are suspended in is 300 mOsmol, the ratio must be adjusted to lower the osmolarity past 130 mOsmol (the point at which all erythrocytes will lyse).

Several biological specifications also constrain the design space of this device. The diameter of a human erythrocyte guides the dimensions of the shear sorting channel. The shear channel dimension must be of the same order of magnitude of the cells to provide for proper hydrodynamic sorting. Across human red blood cells this averages 7.2 μm diameter, with a thickness of 2 μm. Erythrocytes are also shear sensitive and can be lysed by application of an excess of shear. Previous work [1] shows that shear lysis of cells will occur at a rate greater than 5% of cells past 3,000 dynes cm^{-2}, or 300 Pa. Prior to the designed point of cell lysis the erythrocytes must be handled with care to avoid unintended cell lysis.

Two handling specifications for the blood cells can be defined for the storage of erythrocytes prior to encapsulation. The handling buffer osmolarity must be kept physiological at 300 mOsmol. Typical blood handling practices include storing erythrocytes for less than a week, even once washed and resuspended in buffer.

The water diffusion lysis method used in these devices is dependent on allowing enough time for water to diffuse into the cells causing them to swell and burst. The time constant for lysis is 3 s. Thus, post-encapsulation cells

must be held on chip for more than this time to observe lysis within the chip. The design of the chip allows for 4.1 s of residence time, and further modification of the aqueous inlet allows for exposing the cells to a lowered osmolarity prior to encapsulation. This reduces the time necessary for cells to be encapsulated prior to their lysis.

Some constraints on the mechanical system are also present. For ease of fabrication and further paralleization of assays, the footprint of the device should be small, set at 20 mm x 10 mm. The pressure supplied to the devices should be small such that high pressure fittings and danger of forming a biohazardous aerosol is low. This supply pressure is set at 275 kPa. The supply accuracy should also be held accurately as flow metering errors will vary with pressure errors. This effect is somewhat minimized by linking the flow rates in the channels to the same pressure source, but during testing the carrier and dispersed phases are pressurized to different pressures. Thus, the relative accuracy of each source becomes important.

The minimum feature size is limited by the accuracy of photomask generation, or 8 μm. While more accurate photomasks are available, the embossing method is limited by the structural stiffness of PDMS in forming features in thermoplastics. With decreasing channel size more local variation will be present in the embossed features. This minimum feature size also limits the depth of fabrication as the aspect ratio of features should be kept to less than one. High aspect ratio cause mold feature destruction upon removal from the SU8 master and this can cause incomplete channel replication in the embossing stamp. Finally, for testing the wells should contain enough of the reagents to allow for at least 30 min of testing per chip. The wells must then be of a volume of half of the flow rate of the fastest reagent (carrier oil) in μL hr^{-1}.

2.2 Concepts of Design

The devices will be explained at a conceptual level here, and the details will be elucidated in further chapters. For reference a complete device is shown in Figure 2.1 a). The specific parts are shown here, and will be described in more detail below. The device is formed by a standard photolithographic process so all of the black areas are formed as channels at a constant depth. The depth was always made such that the smallest channel on the mask had an aspect ratio of 1. In this case the devices are 15 μm deep. A photo of the device next

Table 2.2: Dimensions of the microfluidic features and their associated resistances.

Channel	**Length** μm	**Width** μm	**Height** μm	**Narrowed** μm	**Resistance** Pa hr μL^{-1}
Cell inlet	24,500	30	15	17	1294
Lysis Agent	9,000	30	15	None	432
Carrier top	57.5	50	15	25	182
Carrier bottom	442	50	15	25	365
Sorting Channel	40	15	15	None	584
Outlets	6,800	600	15	25	904

to a USB connector for size reference is shown in Figure 2.1 b). The thickness of a completed device is 500 μm and the footprint is given in Table 2.1.

2.2.1 Flow Metering

Many microfluidics use external control for metering flow rates on chip. In this work, the inherent resistance in the chips is used to maintain flow and the proper ratio of reagents through the chip. A resistance map of the chip can be found in Figure 2.1 c).

The flow is configured in this device such that the ratio of cell containing buffer to lysis inlet is controlled by the on-chip resistance ratio $R_{lysis}/R_{cell} > 2.3$. This ratio is fixed on each chip design, and can only be modified post-fabrication by viscosity modification of the buffer or lysis agent. It must be greater than 2.3 to ensure that the cells will lyse in the osmolarity resulting from when the streams merge. In a similar fashion, the ratio of carrier fluid coming from the top and bottom is set by R_{ci1}/R_{ci2}. There is no constraint on this ratio, but it will set how far off the centerline of the shear channel droplet generation occurs. This distance is important to achieve proper sorting of empty and cell-containing droplets post-generation.

All of the reagents are loaded into the chip via an external well block that routes the fluid and provides pressurization on top of the wells liquid to drive the flow. The aqueous phases (cell containing buffer and lysis agent) are both pressurized and controlled by the output of a precision regulator (P1, red in

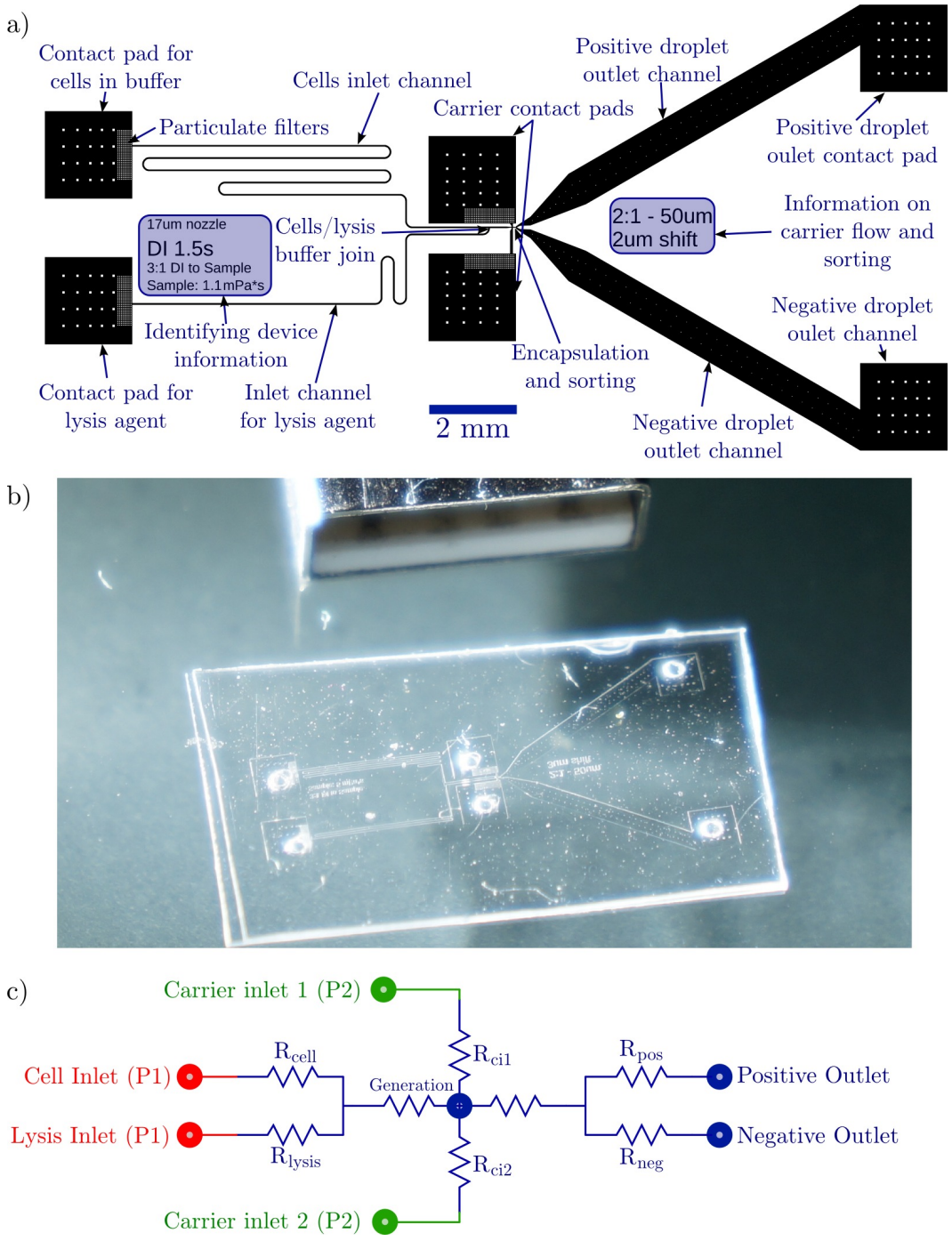

Figure 2.1: a) Mask used to form the devices, where the black sections are channels. Depth of channels is 15 µm. b) Photograph of a fabricated device next to a standard USB connector. The passthroughs have been formed onto the contact pad regions of the device. The thickness ofa device is 500 µm. c) Simplified resistance model of the devices. A separate regulator (P1, red) drives the aqueous phases than the carrier phase (P2, green).

Figure 2.1). The carrier phase inlets are both pressurized and controlled by a separate precision regulator (P2, green in Figure 2.1). By using two regulators that have separate control, the flow rate ratio of carrier phase to aqueous phase can be controlled. This ratio is important during droplet generation to ensure that empty droplets are formed at a size much smaller than a cell containing droplet. It should be noted that P1 ¡ P2. This separate flow control also allows the aqueous inlet channels to be shorter than if all the wells were pressurized by a single source. Once all the parameters of the chip are fixed it is possible to properly design all of the resistances onto the chip. The aqueous inlet channels would have to become much longer to account for their low flow rates at low viscosities compared to high flow rates and viscosities of the carrier phase.

The pre-encapsulation resistance and post-encapsulation resistance are important for overall pressure drop, but their relative values with respect to other locations are not important to the devices operation. The outlet resistances (R_{pos} and R_{neg}) should be equal. If this were not the case, the effect of hydrodynamic sorting would be compromised and the flow around the sorting barrier would be compromised by the resulting unequal flow distribution out of the outlets.

2.2.2 Contact pads

A point of failure in microfluidic testing is the point at which fluids are introduced to the chip. There is a chance of misalignment or leaking when connectors are used. In this work, the contact pads and passthroughs are designed to minimize problems associated with flow connection. The total footprint of the pad is 2 mm x 2 mm, and the thickness is that of the rest of the device (15 μm).

The pad has a very low aspect ratio, in that it is much wider than it is tall. As such, there is a chance that it will collapse during bonding. The chance of this occuring is discussed later in the work, but to prevent this from occuring posts are placed throughout the pad to support the feature. These posts are 40 μm x 40 μm squares separated in both directions by 240 μm.

The final feature in this section is the filter pads. To prevent particulate fouling in the device, the reagents must flow through a tortuous path to enter the exit channel of each of the pads. This section is composed of 16 μ square posts separated by 16 μm. This dimension is chosen to be nearly equal to the smallest dimension in the chip (15 μm). Any particulate that is present either

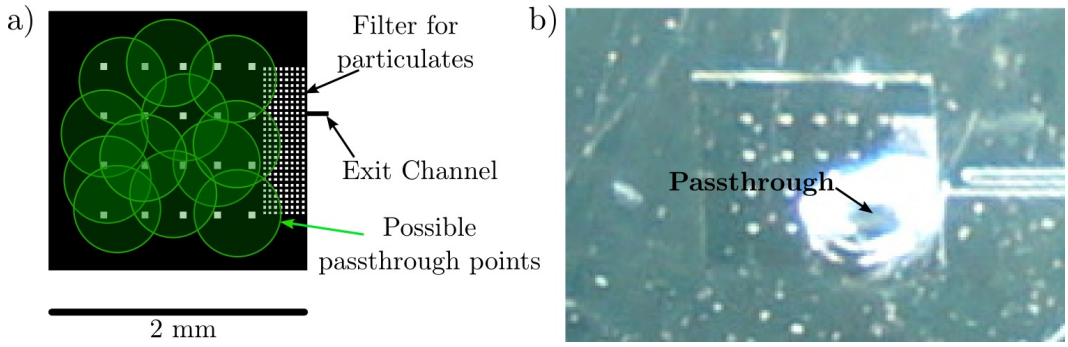

Figure 2.2: a) Mask view of a contact pad used in this work. The filter has 16 μm square posts. The green circles indicate the variability and approximate size of the passthroughs that are formed on the pads. b) A photograph of a pad with a passthrough formed at the lower right. Ideally this would be formed in the center but operator variability necessitates that the pads be large enough for placement within a certain area.

in the sample or oil phases will be trapped here. Even in the event of particulate matter trapping, the pressure drop is not negatively affected as there are many other paths through to the exit.

2.2.3 Generation region of the device

It is within this small region that encapsulation and sorting actually occur. Figure 2.3 shows this critical region. The cell containing buffer and lysis agent combine into the aqueous phase inlet for the droplet generator. This narrows to a smaller dimension (17 μ) before it enters the generator. The reason this narrowing occurs is that larger channels are easier to fabricate on the chip but for generation we want the aqueous inlet to be small to prevent interfacial tension breakup. Thus, the resistance region of the aqueous inlets are wider than this narrowed nozzle.

The carrier inlets are from the top and the bottom. The fluidic resistance of the top is one half that of the bottom even though the channel lengths are very different. Modeling of the overall resistance of the pad and composite features yields this geometry at a ratio of 2 to 1. Additionally, the carrier channel lengths are short because the flow rate and pressure drops are high in

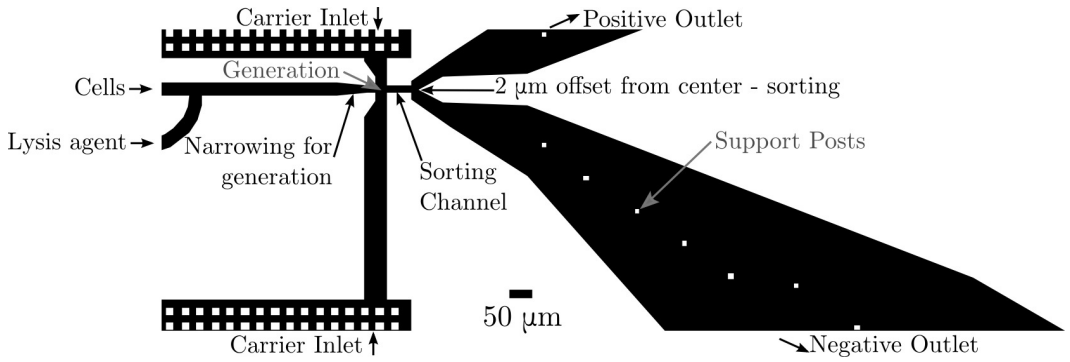

Figure 2.3: Mask view of the generation and sorting areas of the devices.

this region. Because the viscosity of the carrier is 75 times higher than that of the aqueous phase, to achieve the correct flow ratio between carrier and aqueous phases we must minimizs this resistance. Hence, the short top carrier inlet channel.

The sorting channel is a short narrow region of high shear. In this region the droplets that are formed are deformed and sorted based on the migration caused by this deformation. The length and other specifications of this channel will be derived in the fludic design section.

After being sorted hydrodynamically in this channel, the droplets enter a widened region where they can travel into one of two outlet channels. The sorting division is not centered on the shear channel, and is instead offset 2 μm to bias sorting to the positive channel. Since small empty droplets migrate very little in the sorting channel they will enter the negative outlet regardless of the positioning of this barrier. Larger cell-containing droplets will exit the sorting channel and inertia will drive them further out into the widened region where they will strike the sorting barrier. Since only cell-containing droplets will hit this, sorting is biased toward the positive outlet for them.

The outlet channels are shown, and are symmetric about the sorting barrier and identical. Since the features are wide (600 μm) to slow the flow and allow for cell lysis to occur in-channel, posts similar to those in the contact pads are added to prevent excessive feature deformation or collapse during bonding.

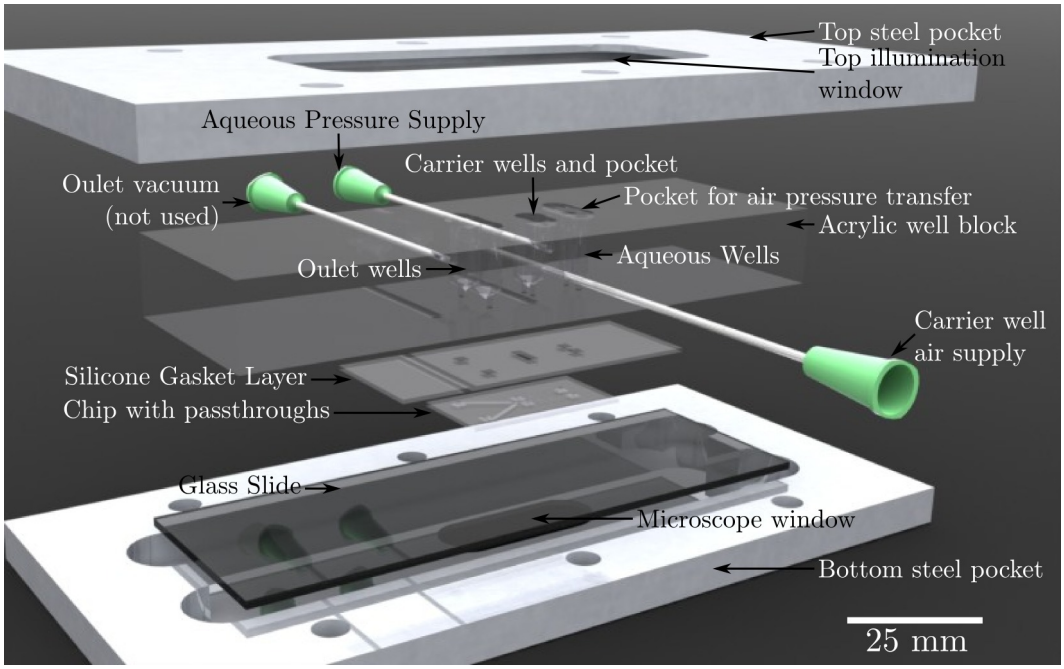

Figure 2.4: A rendering of the sealing jig used in this work. Note there is another acrylic piece placed on top of the acrylic well block that is not shown for simplicity in this figure. The components in the setup are UV and visible light transparent when important to allow for fluorescence and visible light imaging of the chips. The air supply lines are routed in the well block to an air pocket above the wells. In this way the pressure input to the well block drives the fluid through the devices.

2.2.4 Testing of Devices

In this work, the reagents are supplied to the devices via wells on top of the devices.‘ Because the devices are fabricated on 250 µm plastic films and bonded to another 250 µm film, the wells must be machined in a piece of acrylic above the chip. In Figure 2.4 the well block machined out of acrylic can be seen above a silicone gasket that seals the well block to the chips. The steel pockets on both top and bottom provide clamping force to seal between these different layers. The steel also serves to prevent excessive deformation of the plastic and glass. A glass slide is between the devices and the bottom steel pocket to keep the device flat and allow optical and UV access by a tissue microscope.

The device is tested in this way to allow for safety of working with biohazardous samples. After each run the chip can be discarded in biohazardous waste and the jig can be washed with 10% bleach solution. This minimizes waste and allows for any device with the same passthrough pattern to be tested in the same jig.

Chapter 3

Mechanical Design and Fabrication of Devices

3.1 Background

3.1.1 PDMS Issues

Soft lithography and the resulting PDMS device is currently the primary method for fabrication of most research scale microfluidic devices. It offers several attractive features that make it a simple and inexpensive method of device fabrication. Only one photolithography step is required to create an inverse of the channels to be formed, and this allows researchers to minimize costly etching or deposition steps in the clean room. Casting PDMS on the resultant wafer allows for excellent replication of photoresist features, and bonding the channels to either glass or a PDMS slab can be accomplished with UV or oxygen plasma activation. For specific applications such as valving, the elastomeric nature of cured PDMS allows for deformation and channel sealing to impede flow. Finally it offers gas permeability, which makes it useful for gas transfer membranes in certain applications. Despite these benefits, a few undesirable shortcomings diminish its effectiveness in this particular biosensor application.

A shortcoming of PDMS as a biological assay channel material is its network polymer structure. Because there is a lot of free volume in the chains, it tends to absorb liquids and other small biological molecules. This precludes the use in devices designed to perform assays on biological molecules or to keep a constant osmolality in a channel. A long term implantation of PDMS in canine

models resulted in a stable 0.91% weight gain for subcutaneous implantation times between 4 weeks and 2 years [32]. The makeup of the absorbed mass was mainly lipids, and no proteins or phospholipids were seen.

Many microfluidic systems are designed for drug discovery and quantitative analysis of targets, and PDMS can impede this goal to some extent. Toepke and Beebe [33] have shown that no molecules from a 1 μM Nile Red fluorescent dye reached a PMDS channel when filled during a 1 s interval. The dye injected accumulated in the PDMS wall of the filling port. This filling was repeated six times before visible amounts of dye reached the channel itself. After 20 fills, the PDMS around the channel was fluorescent. Washing with Alconox was ineffective at removing the dye from the PDMS. If an assay was performed in this device, the quantitative levels of fluorescence would be skewed as a result. Quinine was also tested in this study as a hydrophobic small molecule of pharmaceutical interest as a anti-malarial. It is autofluorescent, and thus easy to observe any absorption by the PDMS. It was shown that PDMS absorbs Quinine readily at pH 7, but the absorption is reversible at pH 2. This adsorption of hydrophobic molecules can add complexity to assays otherwise avoidable by material choice.

PDMS also absorbs hydrocarbon solvents and other molecules of solvent in hydrocarbons [34]. Absorption of solvent causes the PDMS to swell, changing the dimensions of the channels in the devices. Fluidic resistance is heavily dependent on the hydraulic diameter of a channel ($\propto D_h^4$) so any variations in channel dimension will adversely affect flow in the devices. In digital microfluidics, the use of certain carrier solvents will cause these problems.

The gas permeability of PDMS can affect osmolality of buffers inside PDMS devices. Heo *et al.* [35] set up an experiment to measure the osmolality of cell culture media as it varied with time. The media was constrained on one side with mineral oil and allowed to be in contact with varying thickness PDMS membranes on the other side. This apparatus was placed in a humidified chamber and allowed to sit for 4 days. The thinnest membranes displayed a doubling of osmolality due to evaporation of the liquid phase of the buffer. The problem was solved by adding a parylene coating to the PDMS. However, if one is not aware of the issue, diffusion of vapor across thin interfaces of PDMS can yield shifts in solution concentration.

The prior downsides of PDMS relate mainly to material and chemical incompatibilities. There are also several mechanical issues related to PDMS fabrication, sealing, and fluid delivery. The first of these are pressure rat-

ings. PDMS bonding and interconnections at normal conditions can withstand approximately 300 kPa and this is accomplished with very careful preparation [36; 37]. Modifying the testing setup with additional clamping and different interconnections, the pressure can be increased to approximately 700 kPa. Due to the varying nature of many of these fabrication steps, repeatability is not assured and variation can be seen from device to device, up to a three times difference in burst pressure [37]. The elastic modulus of PDMS is also low so even if the bonding isn't the failure mode of the chip, channel deformation can occur. In a device that is pressure controlled by fluidic resistances in the chip, this deformation will provide inaccuracies in flow metering.

When channel dimensions decrease to the nanoscale, PDMS molding is no longer a feasible option. In one work, dimensions that were designed at 380 nm x 400 nm were replicated in PDMS at 130 nm x 580 nm [38]. Although this size restriction is much smaller than most current microfluidics, it is a restriction that can be overcome with other polymer molding processes.

Finally, interconnects into PDMS can prove problematic. A good review of current methods of interconnects is given by Christensen [37]. The initial passthrough in the PDMS layer is formed by one of two methods. The first method is placement of an obstruction positioned during initial PDMS casting to form a void where the connection will be made. After the PDMS is cured and removed, this can then be removed and a connector can be put in its place. This method is sensitive to positioning errors in the location of the initial obstruction, and requires manipulation of small connectors to make the connection. The second method is to core through the PDMS post-cure to form a pass through. To deliver fluid a slightly larger diameter needle is placed in this through hole to seal. A common problem with this method is that the hole is prone to stress cracking when the delivery needle is inserted. If the fluid delivery rate is low enough, any leak from these interconnections can impeded flow inside of the device. Most current connection methods also increase the size of a PDMS device.

To overcome these material issues, efforts have been made to improve the viability of PDMS. Some groups have added a parylene coating [39], removed small chains from PDMS [34], formed SiO_2 particles in the structure [40], or pre-soaked the PDMS with proteins such as BSA to make absorption of analyte less possible. While these approaches can be effective at overcoming certain PDMS limitations, a shift to different materials can prove more effective at less cost.

3.1.2 Benefits of Thermoplastic Devices

Choosing a suitable polymer or thermoplastic can alleviate many of the problems of PDMS that were discussed before. Most successful commercial microfluidics already use thermoplastics (BioRAD QX100, RainDance RainDrop, *etc*) There is, however, no perfect material for all BioMEMS devices.

Cyclic Olefin Copolymer (COC) is a suitable choice for many biological applications. Its form is a transparent polymer with mechanical properties similar to PMMA. COC posses many properties that make it ideal for this application including UV transparency to 250 nm, an order of magnitude less water absorption than other thermoplastics, ease of injection molding, and resistance to polar solvents [41]. The ease of processing and ease of scaling to a real volume fabrication process make it an attractive option. It also offers good adhesion to metal layers, another essential function for BioMEMS devices. Detailed work has been done making disposable COC devices with metal electrodes [42].

A very real benefit from the use of thermoplastics is the capability for high volume manufacturing. Research scale fabrication of thermoplastic devices is more complicated than PDMS fabrication, but once set up the output is much faster and the devices less sensitive to contamination and processing parameters. Consider a typical soft lithography process. First, a SU8 master is fabricated. PDMS is then cast on this wafer, requiring at minimum an hour to cure. Once cured, the PDMS must then be removed and cored for fluidic passthroughs. This must then be bonded by UV or O_2 plasma exposure to a glass or PDMS substrate. Finally, fluid connections must then be made and the device can be tested. Start to end, with a SU8 wafer prefabricated, a researcher in a lab will get one wafer's worth of devices every 2-3 hours.

The fabrication method of devices in this work is faster than conventional fabrication. The SU8 wafer for this fabrication has the photoresist and cavities inverted. A PDMS stamp is then made off this wafer and cured. This stamp can emboss a wafer's worth of devices every 5 min. Passthroughs must still be made in the devices, and bonding takes a similar amount of time. Yet at worst, this process is at least 6 times faster to make the same amount of devices in a research setting. It can also be easily scaled to a true manufacturing environment by replacing the embossing step with an injection molding machine.

This large volume of devices can be a large benefit when working with biohazardous materials. In this work, to reuse devices would require cleaning

with a 70% alcohol or bleach solution. The bleach would oxidize the plastic and render the device unusable by changing surface properties. Conversely, not cleaning the devices is efficient and saves large amounts of time. It is very simple to just throw the devices in biohazard waste after use and use a new one for further testing. This also makes it easier to avoid cross-contamination between testing runs if the carrier solution is changed. If the device were reused some question would arise about concentrations of residual surfactant remaining in the channels.

3.2 Filter Design to Reduce Clogging

The devices were initially fabricated in PDMS. Particles were carried by the high velocities of the device and would foul the narrow shear channel of the devices. This occurred persistently and would cut the amount of testing that could be accomplished with a device too short to collect useful data. Images of particulate fouling of narrow PDMS channels observed in this work are shown in Figure 3.1 a). Note that the channels shown here are from early devices and the current channel design differs Additionally these channels are larger (40 μm wide) versus the current 15 μm shear channels. The aspect ratio of the entire device is held at 1:1 based on these shear channel features.

The solution to this problem is the design of particulate filtration on chip. A series of 16 μm square posts is fabricated at the inlet of each fluidic channel. These posts are spaced 32 μm apart for a large network of 16 μm channels leading from the inlet pad to the actual channels of the chip. These channels are large enough to easily pass biological cells without fear of cell lysing. They are small enough to catch particles that would move past and clog the shear channel of the device. This built-in sample filtration saves an external step of a technician filtering the fluids and taking care to prevent contamination of the fluids. It works very well, and since implementation no fouling of the shear channel has occurred during testing. An image of this filter design capturing a particle can be seen in Figure 3.1 b). This particle is approximately 35 μm by 16 μm and would have clogged the main shear channel had it gotten past the built in filter.

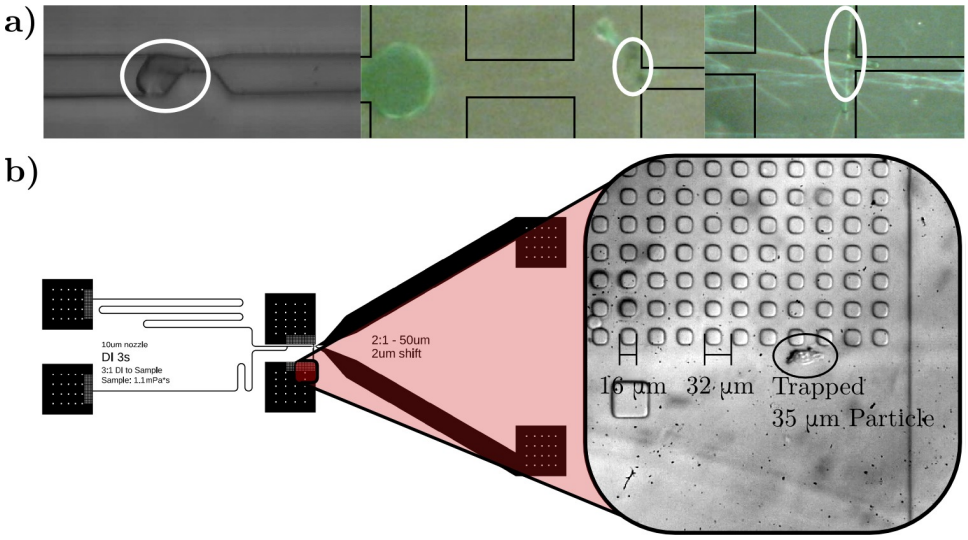

Figure 3.1: a) Illustration of three examples of particulate clogging in PDMS channels. The deposition occurs in the narrowest (15 µm width) shear channel. Channels are highlighted with black lines in poor contrast images. Note that these device designs are from Masks 1-3. b) The design of the fluidic filter in the inlets of the device. A particle of approximately 35 µm length and 16 µm width is seen successfully trapped by the filter. This particle would have otherwise passed into the device and blocked the 12 µm channel of the device.

3.3 Fluidic Resistances

3.3.1 Derivation from Navier Stokes

In this work, geometry dimensioning is used to determine flow rates and ratios on the actual chip. This is a great improvement over the use of supposed constant flow devices such as syringe pumps, as their actual control over flow metering is limited at best. To achieve a functioning chip based on resistance flow control, some modeling is necessary to determine design dimensions of channels. We can begin by determining the resistance of a single circular channel. Once the results are obtained for a trivial circular duct, the results will be appropriately modified to account for the actual crossection of our channels (rectangular). Finally, utilizing the results a simple code can be written to design flow rates into the devices based on the intended fluids.

In the formulation below, the following assumptions will be used:

1. No velocity in the radial or theta dimension
2. Axial velocity (u_z) is a function only of radius
3. Steady, incompressible flow of Newtonian Fluid
4. No slip velocity
5. Gravity force negligible to viscous forces on this length scale

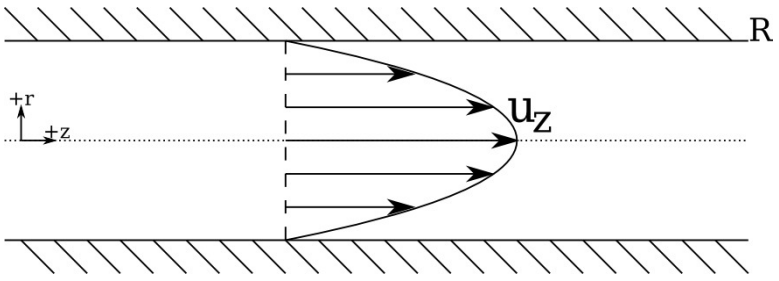

Figure 3.2: Theoretical channel solved for to find fluidic resistance of a single element of a fluidic channel in the device. R is the radius of the channel.

For a single circular channel illustrated in Figure 3.2, we can begin with the Navier-Stokes equation where $\mathbf{u}$ is the velocity field, ρ is fluid density, $\mathbf{f}$ is a body force on the fluid, P is the pressure, and μ is fluid dynamic viscosity.

$$\rho\left(\frac{\partial \mathbf{u}}{\partial t} + \mathbf{u}\cdot\nabla\mathbf{u}\right) = -\nabla P + \mu\nabla^2\mathbf{u} + \mathbf{f} \tag{3.1}$$

We'll look at the radial form of this equation, after simplifications are performed. Refer to the assumptions above.

$$\text{z}: \qquad 0 = -\frac{\partial p}{\partial z} + \mu\frac{1}{r}\frac{\partial}{\partial r}\left(r\frac{\partial u_z}{\partial r}\right) \tag{3.2}$$

All terms of the continuity equation cancel. It is:

$$\frac{1}{r}\frac{\partial}{\partial r}\left(ru_r\right) + \frac{1}{r}\frac{\partial u_\phi}{\partial \phi} + \frac{\partial u_z}{\partial z} = 0 \tag{3.3}$$

The boundary conditions on this equation are no slip at the walls, and the slope of axial velocity along the centerline is 0, since the flow is radially symmetric. These are:

- $u_z = 0$ @ $r = R$
- $\dfrac{\partial u_z}{\partial r} = 0$ @ $r = 0$

where R is the radius of the channel.

We can begin by integrating the z component of velocity to get the following. Note that the coefficient of integration disappears by applying the centerline differential of axial velocity equal to zero.

$$\frac{r^2}{2\mu}\frac{\partial p}{\partial z} = r\frac{\partial u_z}{\partial r} \tag{3.4}$$

Integration once more gives us:

$$\frac{r^2}{4\mu}\frac{\partial p}{\partial z} + c_2 = u_z \tag{3.5}$$

where c_2 is a coefficient of integration.

Applying the no-slip boundary condition at the walls allows us to solve for c_2 and find the velocity profile:

$$\frac{1}{4\mu}\frac{\partial P}{\partial z}\left(r^2 - R^2\right) = 0 \tag{3.6}$$

To determine the pressure gradient in the channel along the z-direction, we can integrate the velocity profile to get an average velocity (v_{avg}). This can then be used for the flow rate in the pipe, which can be related to the pressure drop down it. The differential element is shown in Figure 3.3.

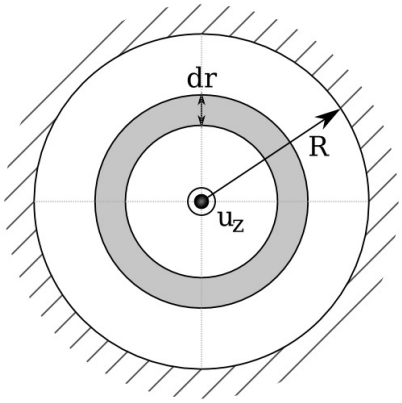

Figure 3.3: Integration scheme to obtain average velocity (v_{avg}). View is cross section of channel.

$$\begin{aligned} v_{avg} &= \frac{1}{\pi R^2}\int_0^R 2u_z \pi r dr \\ &= \frac{1}{\pi R^2}\int_0^R \frac{1}{4\mu}\frac{\partial P}{\partial z}\left(r^2 - R^2\right) 2\pi r dr \\ &= -\frac{R^2}{8\mu}\frac{\partial P}{\partial z} \end{aligned} \tag{3.7}$$

Since the partial differential of pressure with respect to the z direction is actually a constant, assuming developed flow, we can separate it. Dividing both sides by dynamic pressure, we can rewrite this as follows:

$$\frac{1}{f} = \frac{L\rho v_{avg}^2}{2D\Delta P} \tag{3.8}$$

where L is the length of the channel, D is the diameter, and the expression for f is:

$$f = \frac{64\mu}{\rho v_{avg} D} = \frac{64}{\mathrm{Re}} \tag{3.9}$$

This completes deriving a pressure drop for a single channel. The result will be further modified in the next section to account for the fact that we aren't dealing with ciruclar hydraulic ducts, and instead are interested in the rectangular channels that can be obtained by planar microfabrication techniques.

3.3.2 Square Channel Results

To this point (Eqn 3.9) we have been dealing with the derivation for a circular channel. Channels formed with lithographic techniques are actually rectangular in cross-section with some draft angle as a result of lithography or non-perfect etching, and modifications must be made to maintain accuracy on pressure drop calculations. Since the draft angle formed by SU8 exposure is negligible, we will treat the cross section as a perfect rectangle. Many different works have empirically derived correlations for rectangular channels, but we will use that proposed by Kakaç *et al.* [43]. In this case aspect ratio (α) is a function of the channel width (b) and height (a) and assumes the channels are wider than they are tall:

$$f = \frac{24}{\mathrm{Re}}\left(1 - 1.3553\alpha + 1.9467\alpha^2 - 1.7012\alpha^3 + 0.9564\alpha^4 - 0.2537\alpha^5\right)$$

$$\alpha = \frac{a}{b} \tag{3.10}$$

We also must account for the fact that there is no channel diameter as defined by the circular duct pressure drop expression. We introduce the concept of hydraulic diameter(D_h) as a function of area (A_h) and perimeter (P_h) of the channels:

$$D_h = \frac{4A_h}{P_h} = \frac{2ab}{a+b} \tag{3.11}$$

It can be easily seen that for circular cross sections, hydraulic diameter will be equivalent to the actual diameter of the channel.

3.3.3 Minor Losses

Another issue with this derivation is it neglects the increased pressure drop from the developing region of flow. To maintain accuracy while modeling the flow network with this method, we must ensure that the pressure drop contribution of the developing length of the flow is negligible compared to the drop along the length of the entire channel. Developing length (L_d) is conventionally expressed as:

$$L_d = 0.05 \mathrm{Re} D_h \tag{3.12}$$

where Re is the Reynolds number and D_h is the hydraulic diameter of the channel in question given in Equation 3.11.

The experimental literature [44; 45; 46] shows minor disagreement on Equation 3.12, with coefficients ranging from 0.05 to 0.6 for Reynolds numbers below 100. The discrepancy is minor and only high values are only observed at Reynolds numbers lower than used here, so the normal expression in Equation 3.12 will be used.

The channels used in this work are planar rectangular channels, so when looking at Equation 3.11 we can see that b will always be the depth of the photolithographic layer. If we make an infinitely wide channel ($a \to \infty$) we see that:

$$\lim_{a \to \infty} D_h = \lim_{a \to +\infty} \frac{2ab}{a+b} = 2b \tag{3.13}$$

The depth of the channels, b, is 15 μm, so for this work we can approximate the developing length to be:

$$\begin{aligned} L_d &\approx 0.05(20)(2b) \\ &\approx 2b \\ &\approx 30\mu\mathrm{m} \end{aligned} \tag{3.14}$$

This means that, at worst, the developing length is twice the depth of the channels, and at best it is simply the depth of the channels. The error incurred

by ignoring this effect is negligible and it will be disregarded for resistance calculation purposes.

Other minor losses can be safely ignored owing to the low operational Reynolds number and smoothing of corners and turns of the channels.

3.3.4 Viscous losses in oil inlets

The derivation of rectangular cross-section viscous losses describes most of the fluidic resistance of the devices, but neglects locations with more complicated geometries. For example, the inlet pads have a constant resistance that can't be modeled in a simple manner with analytical expressions. Connected to this, the oil inlet channels also have non-uniform cross-section. This section of the device in particularly important for setting the proper ratio of carrier fluid coming into the breakup junction. If the resistance is improperly designed, the flow rates will be off from the design point and only ancilliary video evidence will show the discrepancy. Thus, it is most important to properly model and design this section of the devices. An illustration of this location is provided in Figure 3.4. This illustration shows both top and bottom oil inlet pads in red and blue respectively. The intent of the design pictured is to have twice as much oil flow through the bottom (blue) pad as the top (red). The typical size and location of inlet pass-throughs during device fabrication are shown with green circles. The variation is caused by manual operator error of placing the hole by eye with a soldering pencil.

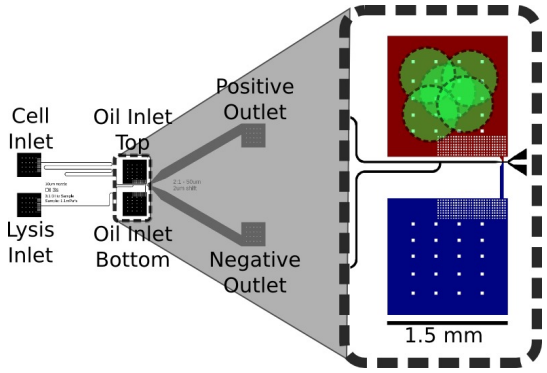

Figure 3.4: View of the area of resistance modeling. The right figure shows the entire device with the inlets and outlets marked, and the exploded view shows the oil inlet section specifically. The numerous green circles show possible locations of the actual fluid inlet, with variability caused by the manual nature of making the pass-through. These are identical to those that would appear on the bottom pad. Ideally the resistance from the red pad to the junction is half that of the resistance from the blue pad to the junction.

Numerical modeling in COMSOL multiphysics is used to solve this complex problem. Since this problem is inherently 3D, there is no way of simplifying the problem into a 2D domain. The progression of modeling will start with a full problem with a simplified rectangular channel (Figure 3.5, (a) and (b)) , and then move on to just the channel (Figure 3.5, (c) and (d)). Using the concept of fluidic resistances we can then combine the results with the analytical work to get meaningful design parameters.

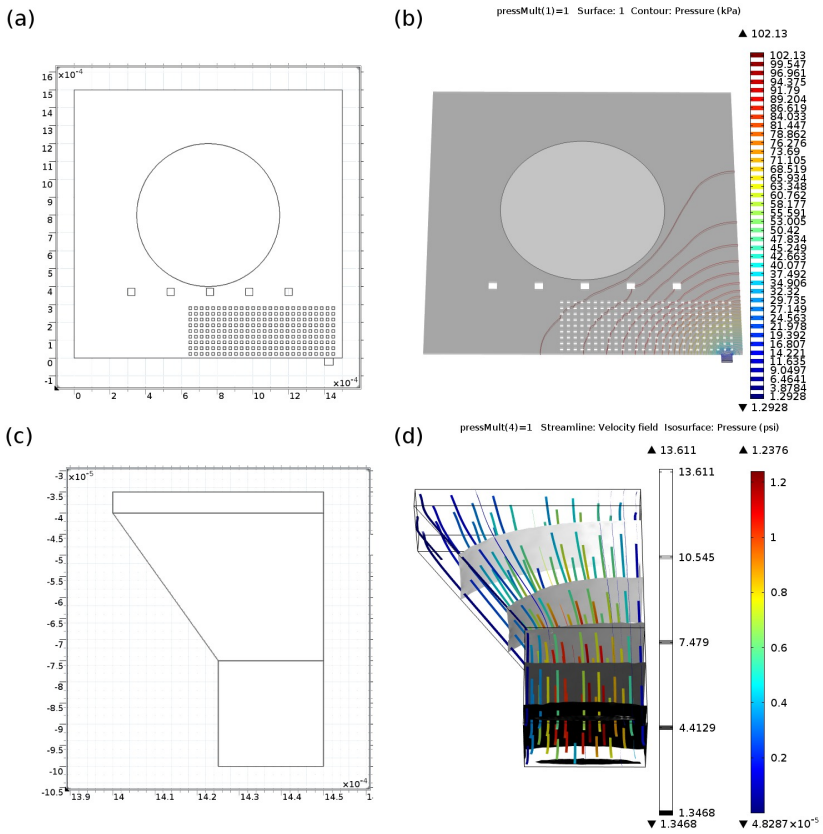

Figure 3.5: Parametric Sweeps run to determine fluidic resistances of complex oil inlet shapes. (a) 2D extrusion to form a pad. Not all posts are modeled since little flow goes above the inlet. (b) Pressure contours of running at 103 kPa with a 50 µm channel. (c) 2D extrusion to form a 60 µm overall length constricted channel. (d) Constricted channel run at 103 kPa. Grayscale iso-surfaces are pressure and streamlines are colored by velocity.

First, we begin by just modeling the pad with a trivial rectangular channel. Note the simple rectangular case channel is not feasible in the actual design as the area is too large for the junction of fluids. A pressure inlet boundary condition is applied on the circular region, simulating where a pass-through is formed with a soldering pencil in the top of the device. The walls are set as no slip boundary conditions, and a pressure outlet with a set pressure of 0 kPa is set at the end of the channel. For each geometry, the pressure variable on

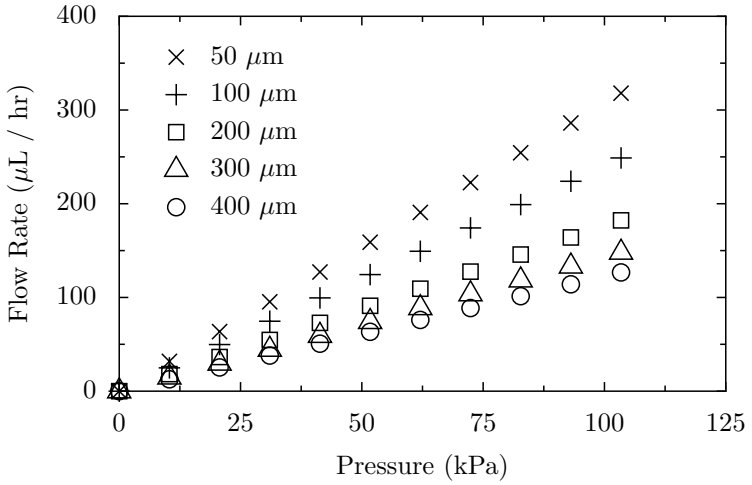

Figure 3.6: Flow rate versus pressure for pad and trivial channel geometry. The different data sets are the lengths of the channel.

the inlet is swept 10 steps between an inlet pressure of 0 and an inlet pressure of 103 kPa. The overall channel length is set at values of 50, 100, 200, 300, and 400 μm. The viscosity is set to 40 cP for this simulation to correspond to a 5% w/v Krytox FSH in Fluroinert FC70 carrier phase, but the results are broader than that. If the viscosity varies from this design point, the overall pressure drop will change but the ratio of flow between the two channels will remain fixed. This data is plotted in Figure 3.6. We can see that for each channel length, the trend is linear as we expect from our understanding of fluidic resistance. The flow rate also decreases with increasing channel length, which is to be expected. Characterizing this decreasing flow rate can back out the resistance of the pad.

The resistance of both the pad and the channel is found by taking the inverse of the slope of this line (in units of Pa hr μL^{-1}). Then a constant resistance is subtracted from all the simulation's resistance and this arbitrary value is adjusted to zero the y-intercept of plotting resistance sans pad vs channel length. As a result of this manipulation, the pad's resistance is found to be 274 Pa hr μL^{-1}. The resistances and adjusted resistance sans pad (or just the resistance of the channel) can be found in Table 3.1. In this assumption for calculating the pad resistance we do end up neglecting the developing length

Table 3.1: Resistances determined from COMSOL simulations. The pad resistance is found to be 274 Pa hr μL^{-1}

Channel Length μm	Resistance Pa hr μL^{-1}	Resistance Sans Pad Pa hr μL^{-1}
50	325	51
100	416	142
200	567	293
300	699	425
400	816	542

contribution for these channels. Recalling Equation 3.13 shows that the developing length for the 50 μm channel length case is 30 μm. Some error will be present in failing to account for this region, but the contribution will be small compared to other errors in the system, especially inlet pad location.

The resistance contribution from just the channel can now be determined. The oil inlet channels are essentially just 3 sections: the first is a wide rectangle of 50 μm width followed by a four sided polygon with one side constricting the final width to 25 μm followed finally by a 25 μm square to attach to the junction. The entire geometry is extruded 15 μm for the thickness of the devices. The rationale for shaping the inlet channel like this is to keep the channel is as wide as possible for as long as possible to keep the pressure drop down. This channel must then be constricted to a dimension appropriate for the junction. Of the three sections in Figure 3.5 (a), the top is elongated and the bottom constriction and small section are kept fixed to get the overall channel lengths tested. For this series of simulations the pressure is again swept from 0 to 103 kPa and the flow rates through the system are recorded. The resistance for each is then plotted versus its channel length in Figure 3.7. Adding the pad resistance to the linear fit displayed here gives a function that can be used to calculate the overall resistance from inlet to junction for an arbitrary length of this geometric configuration. This is written as

$$R_t(L) = 0.955L + 64.6 + 274 \tag{3.15}$$

where R_t is the total resistance in Pa hr μL^{-1}, L is the length of the channel in μm, and 274 is the pad resistance calculated previously.

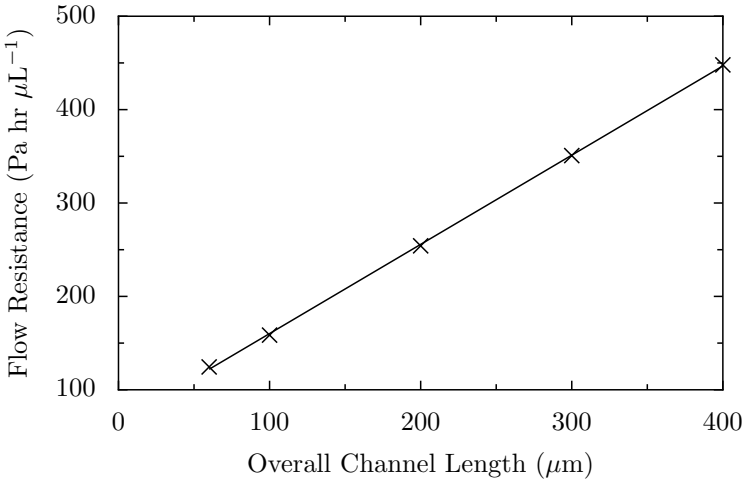

Figure 3.7: Fluidic resistance of 3-piece channel for varying channel lengths. Line of best fit plotted.

Since a method for finding the resistance of these channels has been found in Equation 3.15, it can be applied to finding the correct ratio of resistances. To keep the pressure drop in the system minimal the resistances should be as low as possible. This means the channel in Figure 3.4 should have the shortest possible travel possible with this geometry. This length is 60 µm, and the resistance of this length is 396 Pa hr µL^{-1} from Equation 3.15. To get a 2:1 flow rate ratio the second oil inlet must have a resistance that is twice this resistance. Back calculating, it is seen that a channel length of 475 µm will give us the desired flow rate ratio. This explains the length of the blue channel in Figure 3.4 and completes the characterization of the oil inlet channel resistances.

3.3.5 Application for Channel Design

With the specifics for finding the resistances of channels of given dimensions worked out in the previous sections, we can write code to help quickly iterate and design dimensions of our channels in the devices. This is implemented in Python with a class to return the resistance of a channel (TBChannel.py in Section 7.1). The device dimensions and intentions can be used in the control-

ling script (ChnNetwork.py in Section 7.1) to calculate important dimensions and lengths.

This design tool summarizes all of the fluidic resistances and calculates the correct dimensions to ensure that the devices will operate in a regime that lets encapsulation and lysis work. It prevents the need for complex fluidic simulations while offering the benefit of rapid and actionable results in design of the structures on chip. Before it was used to actually create mask designs, it was validated with FEM modeling which will be presented below.

3.3.6 FEM Confirmation

Once the devices were designed with the Python code based on analytical modeling, the mask was imported into COMSOL multiphysics. The objective was to validate that the code had properly modeled effects that it was intended for and that the flow rates were the design point. The flat 2D shape of the mask was extruded to the depth of the channels, and was meshed as such. A 2D approximation of this shape would be difficult because the main source of fluidic resistance in this design is the small height of the channels. Figure 3.8 shows a section of a particular design with the midplane colored by pressure. It should be noted that the contact pads were excluded from the simulation in the interest of keeping the degrees of freedom low enough for a reasonable solution. The beginning of the channels post-pad are used as the fluidic inlet.

The simulation was set up with the following boundary conditions. A constant pressure was applied on each of the inlets of the same value. The outlets were set as zero pressure, since the pressure that is applied to the inlets is actually a gauge pressure. A design point that was optimized by code was modeled here (34.4 kPa applied pressure). Once the solution converged and was checked for sufficient conservation of fluid (inflow and outflow nearly equal), the flow rates through each of the inlets was calculated by integrating the velocity along all of the inlets. The flow rate can then be compared to the design point to check for errors in distribution of fluid given that pressure. In this case, the flow rates varied less than 10% from the design, lending credibility to the simplified analytical model for fluidic resistance. This completes the numerical validation.

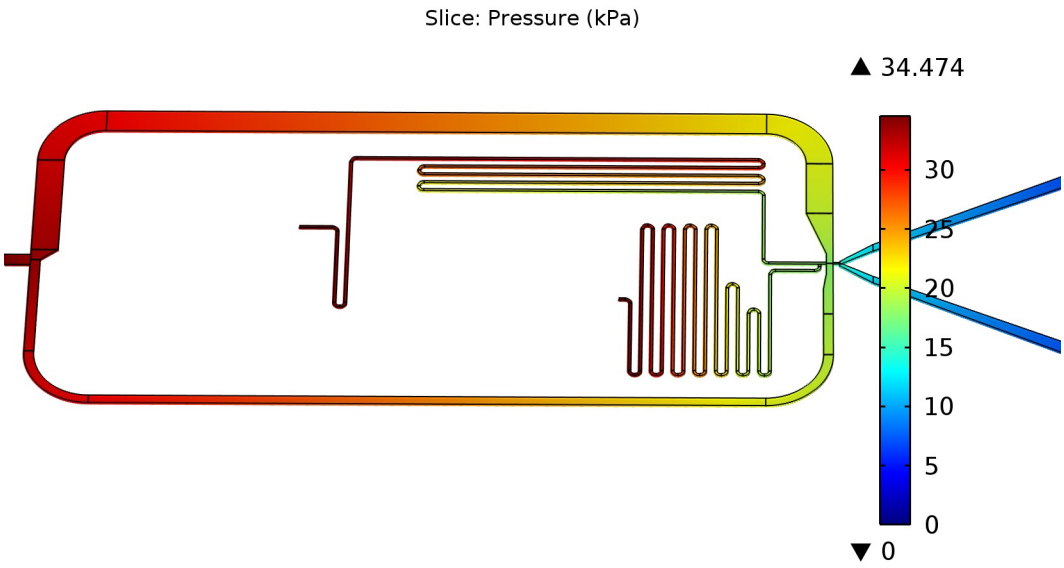

Figure 3.8: FEM model of a device. This model was used to validate the code written for calculating fluidic resistances and distribution of fluid. The inlet boundary conditions are an applied pressure and the outlets are zero pressure.

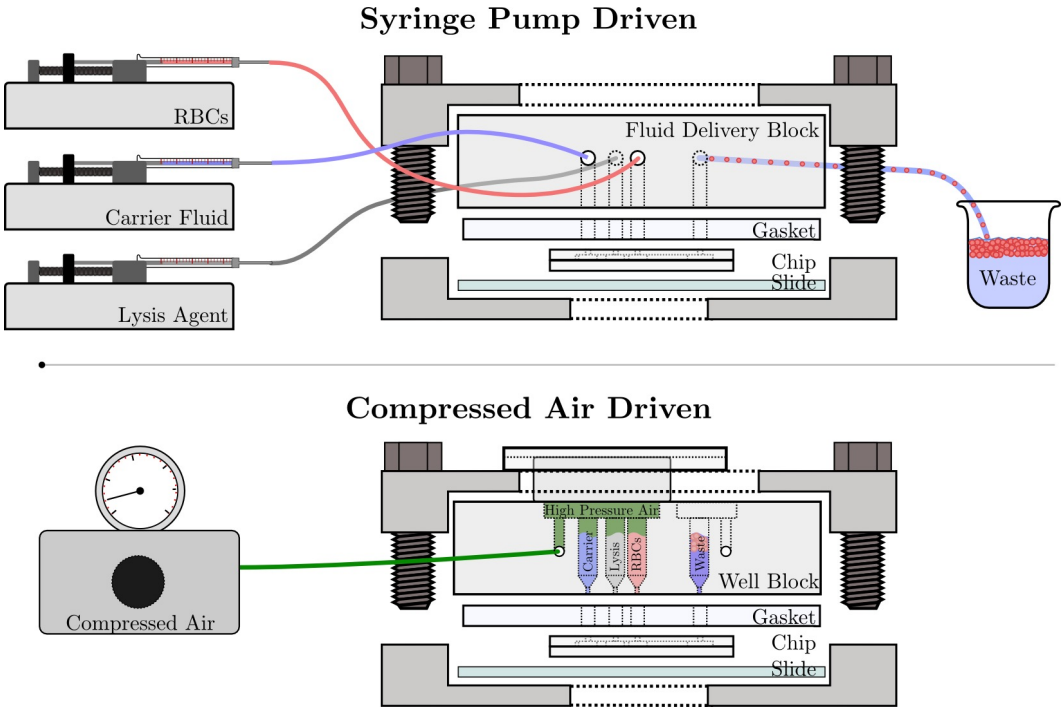

Figure 3.9: Differences in pumping system used in this work. Syringe pumps are used to individually provide a "constant" flow rate to each inlet. In the air driven method one single pressure is used to drive all of the inlets.

3.4 Pumping Methods

Pumping is not often a topic of interest among microfluidics researchers. For most larger and less sensitive devices, inconsistencies in delivery and rate are less likely to affect the operation of the device. The small sizes, high pressures, and low flow rates of these devices exacerbate the ordinary mechanical accuracy of these devices. The two methods of pumping are illustrated graphically in Figure 3.9.

3.4.1 Problems with Syringe Pumps

It is widely known that flexible tubing and disposable plastic syringes can cause flow metering inaccuracies [47; 48; 49; 50]. Using glass syringes and glass

capillary tubing is one method of dealing with this, but it is neither very practical nor useful. The reason is twofold. First, blood cells will non-specifically adhere [51] to clean glass substrates. This adhesion may cause unwanted modification of cellular processes or analyte levels. Though this adhesion can be slowed by the molecular deposition of a bio-compatible protein such as bovine serum albumin, these layers are not permanent and may introduce contamination into the results through stripping the protein from the glass. Second, the price and difficulty of cleaning small glass capillaries and glass syringes that have been contaminated with biohazardous materials make this an unnecessary and arduous clean up in between testing. In the long run this adds cost to the operation of the device.

An optimized syringe pumping system will address most of these issues, but no matter how perfect the fluidics system is there are still mechanical syringe plunger location inaccuracies inherent to the pumps. At the shortest observation times errors of up to 10% are seen in the flow rate metering of some syringe pumping systems [48]. If this 10% inaccuracy is on the syringe pump delivering cells or DI water, the entire flow regime of the device will be askew since the flow rate ratio will be largely affected by this error.

In this work both Chemyx Nanojet and New Era pumps were tested with Hamilton glass syringes (from 10 µL to 1 mL) and both 0.023 in ID Intramedic Polyethethylene tubing (Becton-Dickinson) and 150 µm fused silica tubing (LabSmith). It should be noted that due to space constrictions of the inverted microscope, a long length of tubing was required to reach from the syringe pumps to the devices. Due to this dead volume, the use of the smallest syringes of appropriate volume was limited. The small volume of fluid in these syringes is insufficient for filling all the dead volume prior to use.

Regardless of syringe and tubing type, flow metering errors were so prevalent that this system is of no use to this work. Errors in flow metering took one of two types, illustrated in Figure 3.10. Where the system was optimized to remove compliance (glass syringe, capillary tubing) the effect was similar to Figure 3.10 a) where only minor disruptions are present in the generation of droplets. Still, this variation in flow rate modifies capillary number ($Ca = \mu v/\gamma$) in such a way that the empty droplet volume is modified along with the spacing of the droplets. These drops must be sorted based on volume post-generation, and these deviations affect that efficiency.

The second and more drastic error can be seen in Figure 3.10 b). This type of error was present when larger syringes (1 mL) were used along with

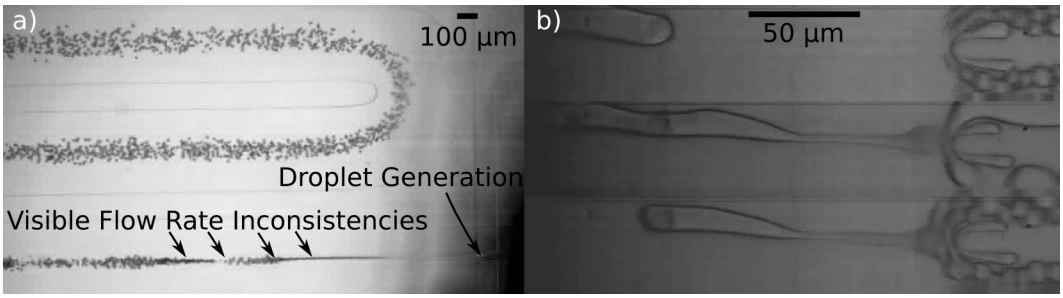

Figure 3.10: a) Inconsistency in flow rate delivered by syringe pump. Due to the variation in clustering of the droplets it is clear that the flow rate is varying in each step of the motor. b) Three frames from a video detailing stepping so severe that the flow is interrupted for periods.

plastic tubing and high pressures. This regime is where the stepper motors of syringe pumps are at their worst (low speed, high torque) and the excess pressure in the tubing is causing large deviations in the tubing due to its higher compliance. In this metering error mode, the forward flow of the sample line is actually interrupted and reestablished for each pulse of the stepper motor. Downstream generation of droplets is inconsistent due to variations in capillary number, and both jetting and droplet formation can be seen throughout the cycle of one pulse of the fluid. It is clear from many repetitions of this failure that this is not an acceptable method for metering flow for this project.

3.4.2 Compressed Air Drive

Providing a gas of constant pressure is a more effective solution than providing constant velocity required in a syringe pumping system. When metered through precision air regulators a very specific pressure can be supplied over a reservoir of liquid. This driving force is not subject to the stiction of a syringe plunger in the barrel, the mechanical location errors of the stepper motor, or compliance in any air lines. Regardless of the flow rate of the liquid, the driving force will remain constant. Using compressed air also offers three long term advantages. First, the contamination of a sample to be tested is minimized if it never comes in contact with a previously used syringe. Since these chips are disposable, the only biological material to come in contact with them is

the one that is currently being tested. Second, diagnostic labs already have air supplies in the building with which to provide this driving force. The gas is already clean (bottled nitrogen, argon, etc.) and present. For field work, gas can be compactly provided via cartridges of gas, such as carbon dioxide. For more rudimentary field work, other options can be pneumatic tires, air pumps, or even a small hand powered pump. Third, the chip becomes more self-contained, and the flow rates in the device are decided solely by fluidic resistances on chip. Since accuracy is more easily obtained while micro-milling an injection mold or microfabricating a stamp for device fabrication than while pumping fluid through each and every chip in the field this will give more repeatable long term results.

When the chips were redesigned for pressure driven operation, the idiosyncrasies present in Figure 3.10 from syringe pumping effects were completely eliminated. The flow will remain stable as long as liquid remains in the reservoirs. This arrangement does prevent varying the flow rate of the aqueous phases and the oil phase independently, but this can be solved by the use of two regulators with one pressure above the oil reservoir and a separate pressure over the water reservoirs. Exact flow rates cannot be determined with this method, but approximately determined by the velocity of droplets in the shear channel.

3.5 Plastic Fabrication

Since PDMS was determined to be a non-ideal material for this project, an alternate fabrication method must be determined. It must be simple and easy to perform at a research scale with a minimum of complex process steps. Six main polymer molding types are discussed frequently in the literature [52; 53], injection molding, reaction injection molding, hot embossing, injection compression molding, casting, and thermoforming. There are several others that have been used, but suffer from unnecessary complications, such as etching and polymer laser ablation [54]. Since these approaches aren't efficiently scalable they are not further investigated. Embossing will be studied here, which offers the advantage of scaling to large volumes. If even larger volumes are required, transitioning to injection molding utilizes the same general design and fabrication process.

Table 3.2: Printing parameters of different attempts. The mold and features are qualitative observations of quality of their respective parts based on how many defects, air voids, or unintended geometry features are present.

	Mold Material -	Angle deg	T deg C	Time at T min	Vacuum -	Cooling Time min	Pressure kPa	Mold -	Features -
1	Su8/Si coated	0	140	2	No	1	25	–	+
2	Su8/Si coated	0	110	2	No	1	29	-	-
3	Su8/Si coated	3	105	2	No	1	29	-	–
4	Su8/Si coated	5	107	10	No	1	29	–	–
5	Su8/Si coated	5	150	5	No	1	29	-	–
6	Su8/Si coated	0	145	12	Yes	6	32	-	+
7	Su8/Si coated	0	158	10	Yes	7	34	-	-
8	Su8/Si coated	0	155	52	Yes	6	32	-	–
9	Su8/Si coated	0	180	10	Yes	6	32	-	-
10	Su8/Si coated	5	160	10	No	2	29	-	+
11	Su8/Si coated	5	155	1	No	1	29	-	+
12	Su8/Si coated	10	145	5	No	2	29	-	+
13	6mm PDMS	0	158	10	No	2	29	+	+
14	2mm PDMS	0	158	5	No	2	29	++	+
15	12mm PDMS	0	155	5	No	1	29	+	+
16	12mm PDMS	0	155	5	No	2	29	+	+
17	12mm PDMS	0	155	5	No	8	29	+	++
18	8mm PDMS	0	145	6	No	6	29	++	++

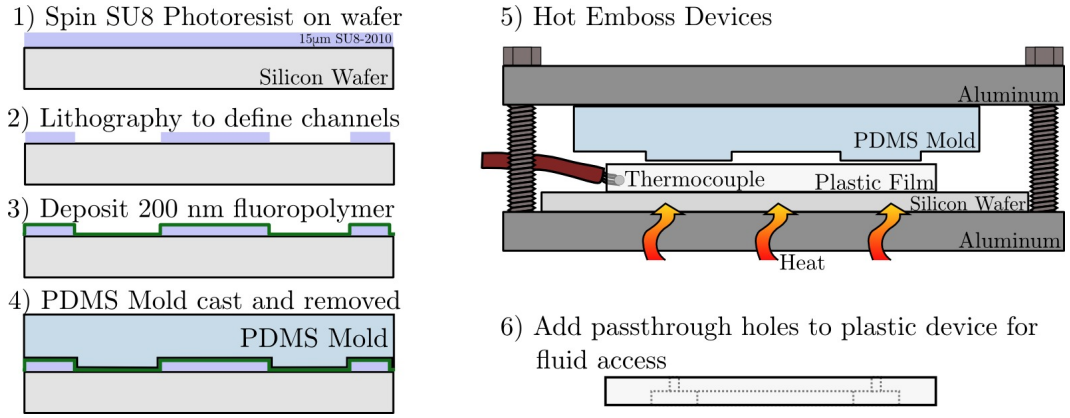

Figure 3.11: Embossing process using a PDMS mold. For tests just using the SU8/silicon master the features are inverted and the silicon wafer used as the embossing stamp.

3.5.1 Molding Attempts

To find an ideal molding process, main process parameters were tailored. The mold itself was either SU8 photoresist on a silicon wafer or a PDMS stamp. While the mold was brought into contact it was either angled or kept flat with respect to the plastic to be embossed in the hopes of reducing air accumulation around features. The temperature, pressure, and vacuum were also adjusted between different attempts. The method of embossing the plastic devices is described here, and is shown schematically in Figure 3.11.

First, an inverse mold of the features was made with SU8 (MicroChem) on silicon. The grade was varied depending on the thickness of the features, but SU8-2010 and SU8-3010 were most commonly used. These are similar viscosity photoresists, but 3010 has improved bare silicon adhesion. The proper datasheet provided by MicroChem was followed for the feature definition. A layer of fluoropolymer was deposited on the mold to ease release. The process parameters for this deposition using C_4F_8 were 50 sccm, 100 W of plasma power, 48 mTorr, 20 nm/min deposition. This was performed for 10 minutes for what should be a 200 nm coating of fluoropolymer. Using a hot embossing press with pressure and temperature control, several molds were used to emboss features on a cyclic olefin copolymer (COC, Topas 8007) film of 250 μm thickness. An overview of process parameters can be found in Table 3.2. Several problems

were encountered using this hard mold. First, air that was trapped in the polymer formed voids and tended to get trapped at the corner of features. In processes such as injection molding, the pressure of the incoming melt is high enough to condense trapped air to liquid. In the embossing performed here at low pressures, there is no such force available and this air becomes a problem. Second, the thermoplastic has a higher thermal coefficient of expansion than the SU8 and silicon master and during cooling the stresses placed on the SU8 can cause it to break free of the silicon. When this happens the mold is ruined. Third, finding an equilibrium between good feature patterning and too much melt is unsuitable for an academic setting.

To overcome the limitation of trapped air, this process was performed in a vacuum chamber pumped to low vacuum. Three molds were made, but the feature definition was still unacceptable. Air was still present, and getting the entire embossing setup into a higher vacuum is unsuitable for a research setting. To deal with trapped air more efficiently at low molding pressures a gas-permeable mold is used instead.

PDMS was chosen as a molding material because it's properties are optimal for this process. It is crosslinked and can withstand temperatures to 400°C without degrading [55]. Its gas permeability allows any entrained regions of air to diffuse into and through the mold, even at low pressures. Finally, it has a high coefficient of thermal expansion. This means that after molding is completed, it will contract faster than the thermoplastic during demolding and thus it's features will not be harmed by successive use of the molds. Others have used PDMS as a molding material for thermoplastic embossing [56; 57; 58; 59]. Several used it for patterning non-planar surfaces, and some others have used it for planar patterning of very small features. By using a PDMS mold in a small aluminum jig it is possible to pattern in any temperature controlled setup. It is with this combination that devices are produced.

3.5.2 Process Parameters

The ideal process for printing these devices will be outlined here. The jig is first disassembled and the parts of aluminum as seen in Figure 3.11 are separated. A silicon wafer is placed on top of the bottom aluminum piece to make sure the bottom of the plastic stays transparent and pattern-free. The blank plastic film is placed on top of this. The PDMS mold is placed feature side down on top of the plastic, and a thermocouple is placed between the PDMS

Table 3.3: Optimal printing temperatures for four thermoplastics. The pressure in each case is 30 kPa.

Material	T_G (°C)	T_{Press} (°C)
TOPAS 8007 (COC)	80	155
Polymethylpentene	26	250
Polycarbonate	145	190
Polyvinylidene fluoride	-35	190

and plastic for monitoring the temperature of the plastic during molding. The top piece of aluminum is added and the bolts are tightened in a star pattern with a torque wrench to the proper force. The entire assembly is placed on hot plate and the plastic temperature is monitored. Once the target temperature is reached, the assembly is removed and placed on a large aluminum heat sink to expedite cooling. The target temperature for different plastics is catalogued in Table 3.3. When the temperature of the plastic has cooled to below 50 °C, the aluminum is again disassembled and the devices removed. Since the PDMS has shrunk, there is no special demolding step required, and the mold and devices will separate with little force required.

3.5.3 SEM Images of Unbonded Devices

To ensure the patterning of features succeeded SEM images of devices produced in the above manner are taken. They can be found in Figure 3.12. These devices weren't kept adequately clean during transport to the SEM and dust particles have accumulated on the feature surfaces due to residual electrostatic charge in the plastic film. Between patterning and bonding, the devices can be kept contained with masking tape to prevent this type of particulate contamination.

3.6 Bonding of COC Films

Once the chips are fabricated, a method for enclosing the channels must be developed. Bonding plastic chips has been an area of difficulty in most plastic

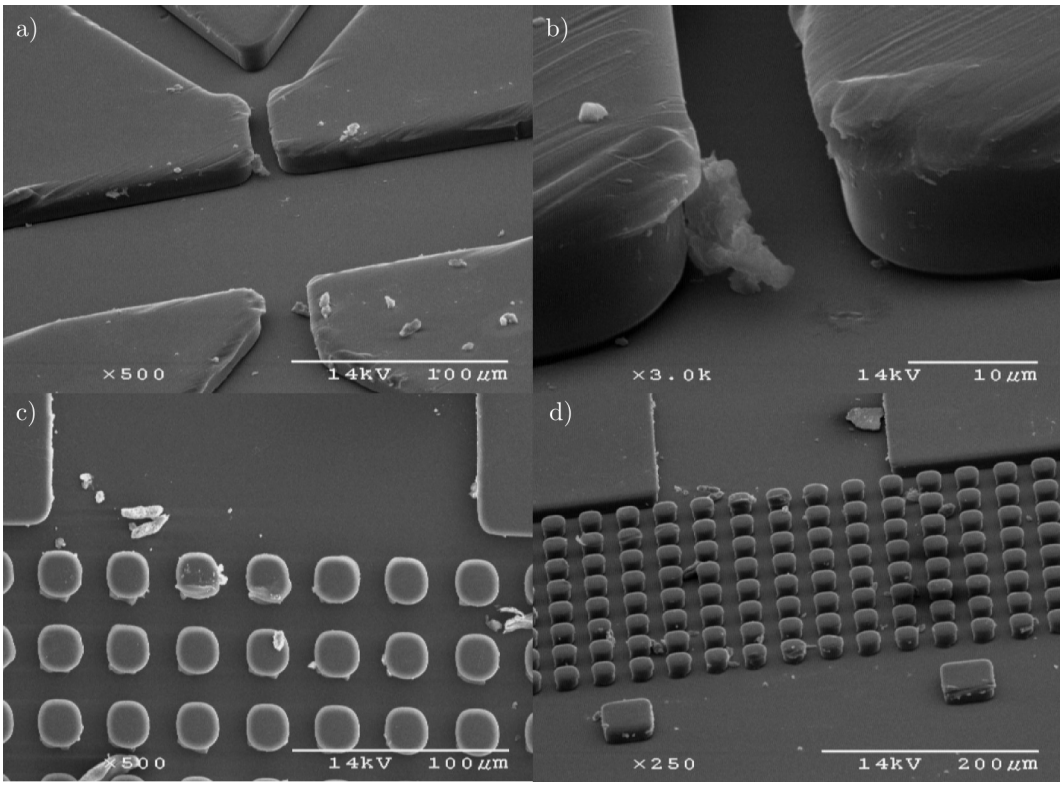

Figure 3.12: SEM images of printed device features before bonding. Note that dust had accumulated on the devices during transport to the SEM. a) 60 deg look at the smallest channel on the device, nominally 12x12 μm. b) Closer view of the smallest shear channel. c) Top view of the filter arrays at the entrance to channels. d) 60 deg view of the same posts.

microfluidic works. Unwanted side effects of bonding are common, such as surface property modification, channel deformation, or sagging of the bonding film. Finding a recipe that produces consistent and acceptable results can take a matter of weeks, if not months. Some common bonding methods include ultrasonic [60; 61], solvent [62], surface treatments [63], and thermal [64]. In this work, both solvent and thermal bonding have been attempted with better results coming from thermal bonding.

3.6.1 Solvent Bonding Methods

Several attempts at bonding COC with cyclohexane (Sigma) were performed, similar to work done by Mair *et al.* [62]. Cyclohexane vapor was contained in an inverted Pyrex container. The COC surfaces were treated in this container, varying the time and temperature of the vapor. Typical times were 20 s to 3 min, and temperatures from room to 40 °C were used. In different tests the capping layer, device layer, or both were exposed to cyclohexane vapor prior to bonding. After the allotted exposure time, the devices were removed and varying forces were applied to the devices to achieve bonding. The force was distributed via a flexible silicone gasket (McMaster).

The results of this solvent bonding were widely varying. In cases of too little solvent modification, the devices were incompletely or not at all bonded. In cases of too much solvent exposure, some or complete channel occlusion was observed. Similar trends were seen with bonding pressures. Conversations with industrial engineers in this field have confirmed that this type of method requires extremely strict process controls and even batch-to-batch variations in COC resin blends can entirely upset the bonding procedure. Some other combinations of solvents and thermoplastics were tested, but finding the razor edge of proper bonding conditions is not suitable for research scale bonding.

3.6.2 Thermal Bonding

Thermal bonding was then used as bonding for this work. After some minor iterations a repeatable method for bonding the devices was found. Typical thermal bonding processes involve bringing the plastic to near its glass transition temperature then applying high pressures to bond the layers. This method is equipment intensive and is prone to channel deformation as a result of increased plasticity of the heated plastic. To modify this process for lower forces

the plastic will be brought past the melt temperature, but only slightly and for a brief amount of time. Simple contact between layers with no applied force was found to be sufficient to produce strong bonding. The only force applied was the weight of the capping film.

The method of bonding is as follows, and is illustrated in Figure 3.13. This figure shows the fabrication process of devices from hot embossing through bonding and the pictures will be referred to below. The devices are first fabricated by hot embossing (Figure 3.13 a-c). Masking tape is placed on the feature side after demolding to prevent any accumulation of particulate contamination. Pass-throughs for the fluids are added in the pad locations with a fine tipped soldering pencil (d). A blank sheet of the same thermoplastic used for fabrication is then cut to the size of two devices. For this process two devices are bonded at the same time. If the entire four-inch wafer worth of devices are bonded at once, the sheets won't come in contact evenly across the entire area. Sets of two devices are then placed feature side down on top of the blank film (e). The temperature of the wafer is brought to the feature definition temperatures, listed by plastic in Table 3.3. Because there is no force or pressure on the plastic, the slightly molten plastic will not reflow and deform the features. After 30 sec, the wafer is transferred to an aluminum cooling block and the devices are removed from the wafer (f). A finished device can be seen in Figure 3.13 g).

Bubbling can be seen on the finished devices, but this actually isn't a problem for operation. The bubbling occurs because the COC layer entrains air as it is becoming more viscous and seals against the silicon. This air is trapped between the sealing COC layer and the silicon wafer. It will cause a global warping of any features in the bubbled regions, but the length scale of bubbling (5 mm) is much greater than the length scale of any features (0.2 mm) and this is not fluidically important.

Eliminating this bubbling is possible through two methods. The first is applying a force prior to placing the heat source on the wafer and then removing it once the plastic heats past melt temperature. This would allow the COC to be flat against the wafer, but would also prevent any channel deformation caused by forces in the plastic. Second, another gas permeable layer could be placed between the COC and the wafer. A thin spun-on film of PDMS would be ideal for this application. This would allow any bubbles formed to disperse. However, this bubbling does not affect the operation of the devices and no action is taken.

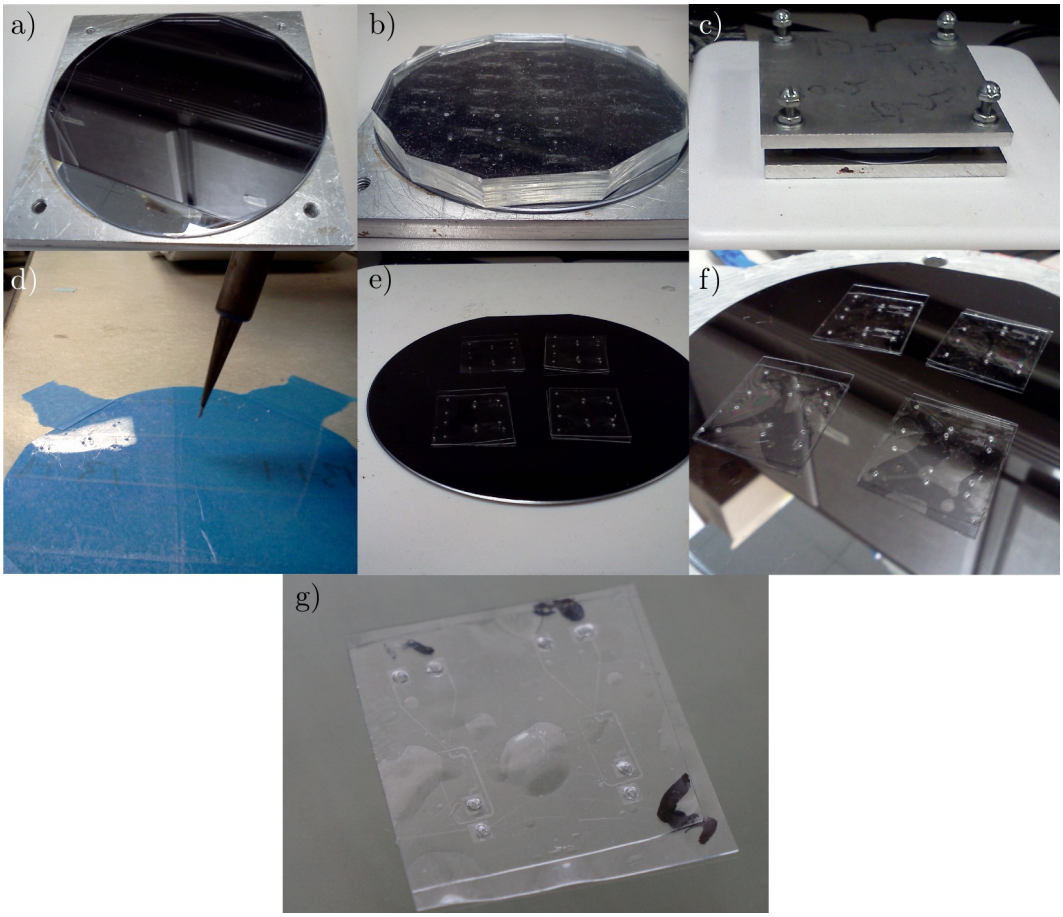

Figure 3.13: Images of Device fabrication and bonding. a) Plastic film on silicon wafer ready for embossing. b) PDMS stamp in place. c) Stamp and plastic film in fixture on hot plate. d) Completed embossing and adding fluidic pass-throughs with a soldering pencil e) Devices on another plastic film for bonding. Four sets of two devices. f) Post-bonding of devices. g) Image of two bonded devices.

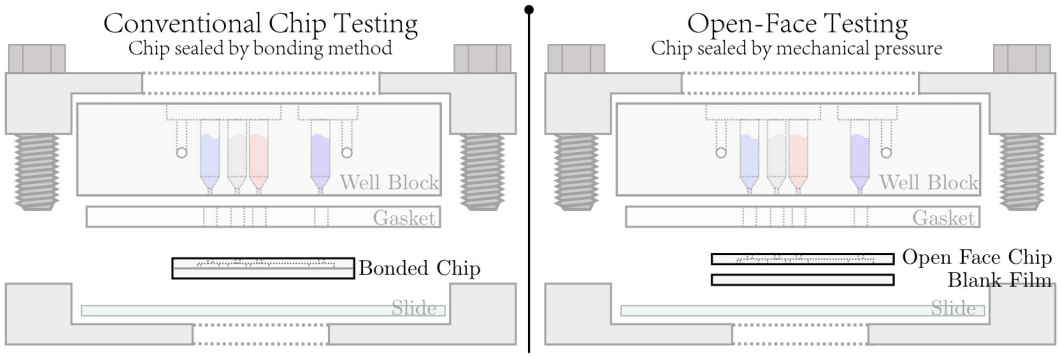

Figure 3.14: Two methods of sealing. On the left, a conventional microfluidic network of channels is formed on one piece of substrate, then bonded to another to close the channels. On the right, the proposed method foregoes the complicated bonding step and can test the open faced channels by sealing them against a flat and like substrate with mechanical pressure. The gasket used is flexible to even out the applied pressure field.

3.7 Open-faced microfluidic sealing

The devices can be tested without bonding to another surface if the fluid has a sufficiently high viscosity and high contact angle. In these cases fluid can be run through an open-faced network of channels by simply by applying mechanical pressure evenly on the top of the devices while pressing the feature side onto a flat piece of plastic, and the important differences versus conventional testing are illustrated in Figure 3.14. This operation is similar to a set of enclosed channels formed by bonding these channels with a sealing face. With high contact angles and viscosities, the capillary pressure pulling fluid into cracks between the plastic layers with features and the facing layer is low and little fluid wicks out of the channels. This is the case with the peanut oil and SPAN80 carrier oil system, so some results from a bonding-free method for sealing microfluidics is presented here.

There are some obvious benefits to this technique at a research scale. Bonding processes are time consuming to perfect, and require strict control of parameters such as resin batch, temperature, humidity, pressure, and several other parameters. By avoiding that step, considerable time can be saved on device development. Additional benefits are realized with an unbonded chip in clog-

ging and internal characterization. If an unbonded chip fouls during testing, it is possible to open the device and clear whatever is causing the problem. If post-testing analysis of channel dimensions, protein deposition, or other internal surface characteristics is important, it is trivial to open the device after testing and measure this through physical methods.

3.7.1 Microfluidic Channel Deformation under Loading

To seal the channels against a flat surface pressure (2 MPa) is applied to the back surface of the film with channels. It can be inferred that as the width of the channel increases, the center of the channel will deflect further and decrease channel height. Eventually as the channel widths increase, the center of the channel may completely collapse. To figure out what deflections will occur, COMSOL modeling of the problem is performed.

The simulation is modeled as a 2D problem of the cross section of one channel. Initially the film with channels is not in contact with the sealing face. Contact pairs are specified on the all of the channel faces and the opposing film top face. The horizontal friction force is set at zero since the plastic will slip to reach a final location. Because the simulation is run as stationary, an accurate initial guess for contact force distribution along the length of the touching faces is necessary. A distributed load of 2 MPa is applied over the channel film, as the silicon gasket keeps the force applied on the channel film uniform. The bottom sealing face is meshed much finer than the channel section to prevent numerical oscillations during contact. The boundary conditions on both the left and right sides of the simulation are symmetry conditions, and the bottom film surface is fixed in place. The boundary conditions and mesh for the problem can be found in Figure 3.16. This simulation is scripted into a MATLAB function that makes the appropriate calls to COMSOL solver libraries, and returns the normal component of the stress tensor along the contact interface as well as the deflection of the center of the channel. In this way, the simulation can be run through a variety channel heights and widths by simply modifying the MATLAB control script.

First, we are interested in the deflection of the channels under the clamping pressure required for channel sealing. If the channel deflects so far as to modify the initial geometry, the bonding-free method is not very useful to retaining rectangular cross-section channels. Worse still would be if the center of the channel deflects to the point of contacting the opposing sealing face. We can

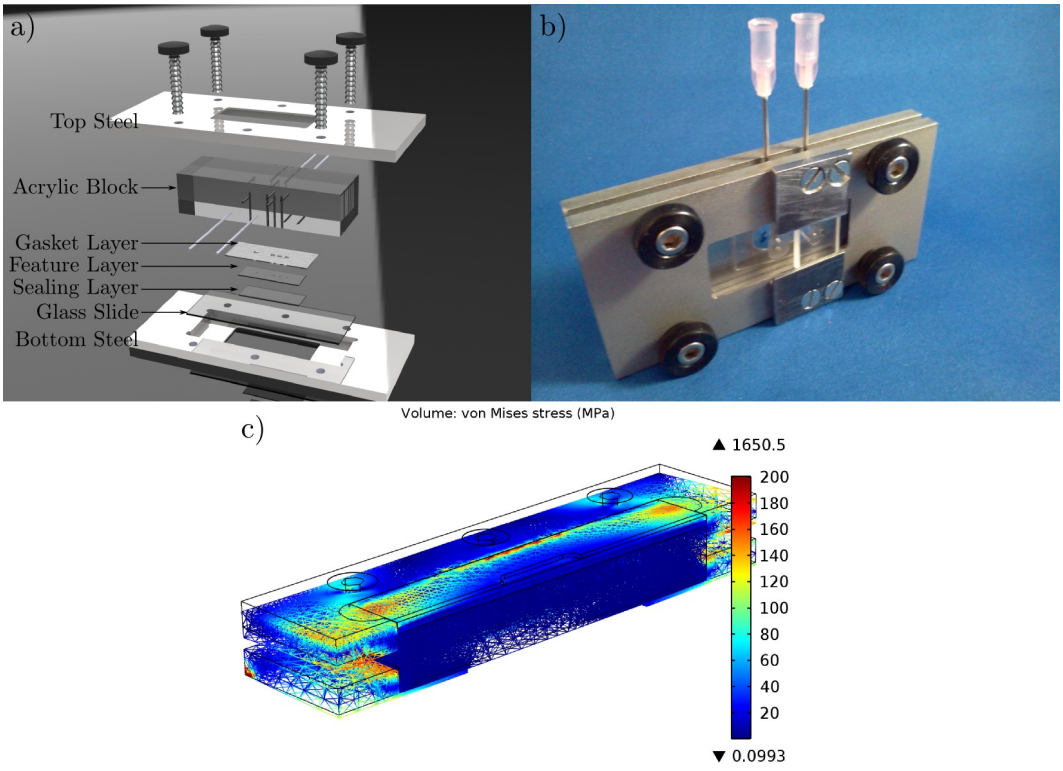

Figure 3.15: a) Rendering of the jig to seal unbonded devices together for testing. The unbonded devices face down onto a flat extruded plastic of the same type. b) Machined jig, modified slightly for pressure control of flow rates with an additional acrylic capping layer. c) Simulation of stresses in jig during max applied forces run in COMSOL. Some iteration was necessary to prevent unmanageable stresses on the glass slide which result in fracture.

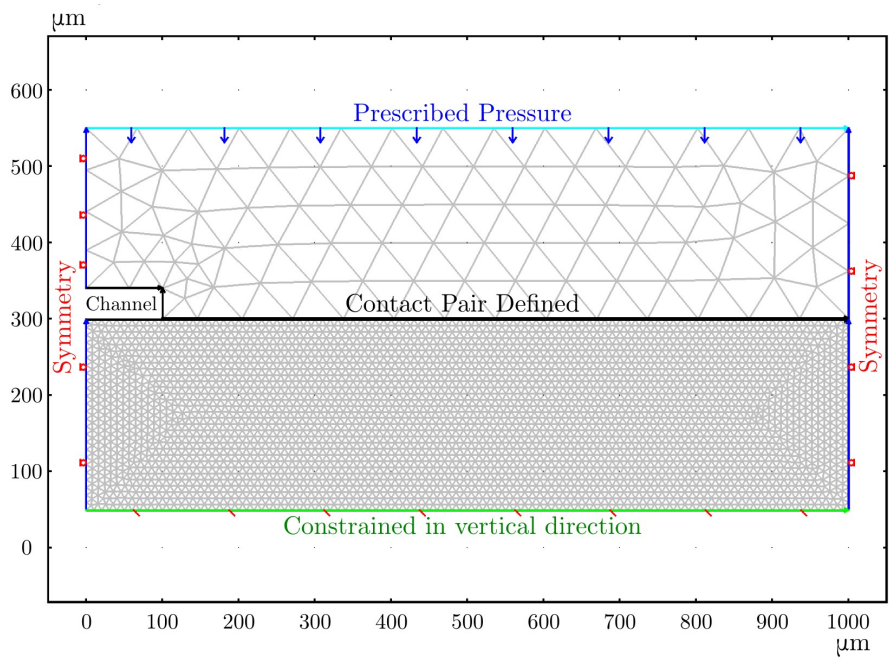

Figure 3.16: Boundary conditions and mesh applied to the simulation with a 200 μm channel. The top is applied pressure, the left and right are symmetry, and the bottom is fixed. The contact pair is defined as the channel faces and the two opposing faces. Mesh size is different top and bottom to prevent numerical oscillations.

simulate how much center channel deflection will occur over a common range of channel widths and heights in a 250 μm thick film.

To express the results of the simulations, we plot the normalized channel center height, α. This is defined as:

$$\alpha = \frac{h_{\text{center,deformed}}}{h_{\text{center}}}. \tag{3.16}$$

A visualization of these two heights can be seen in Figure 3.17 a).

The results of the simulation can be found in Figure 3.17 c). A plot of the deformed shape colored by von Mises stress can be seen in Figure 3.17 a). For channels less than 200 μm in width, α is greater than 0.9 for all channel heights used commonly in the devices (from 5 μm to 100 μm). This suggests that these are acceptable channel configurations for use in this device, as the deflection is minimal. Past 200 μm channel widths we see that channel height strongly influences the deflection of the center. For a 5 μm channel height, the channel collapses at around 800 μm. As channel height increases, the effects of the deflection is lessened

This figure also serves as a design tool to figure out where mid-channel posts should be used to minimize deflections. If a low height, wide width channel is required, posts can be added to prevent collapse of channels in the devices.

The maximum fluid pressure that the device can handle is a function of how hard the device is clamped against the sealing layer. Although an even clamping force is applied on the devices, the edges of the channels see locally higher normal clamping pressures. This is because the pressure that is applied directly above the channels is supported by the channel sides and translates into additional local pressure at the sealing corner of the channel. This works to our benefit as less pressure can be applied to seal the channels to operate at given pressures. This excess force can be correlated to normalized edge clamping pressure, and is presented in Figure 3.17a.

To test the device for leaks, the following protocol is performed. First, a single channel device has one of the two fluid passthroughs created. This allows air to enter the device, but not exit the other end of the channel. The device is then assembled as usual and sealed with the six bolts. A connection between the device and a 10 mL syringe filled with air is created. The dead volume of air inside the device, interconnect layer, acrylic block, needle, and connection line is calculated. Knowing the total air volume of the system allows the pressure inside of the device to be calculated with the new volume of the system after

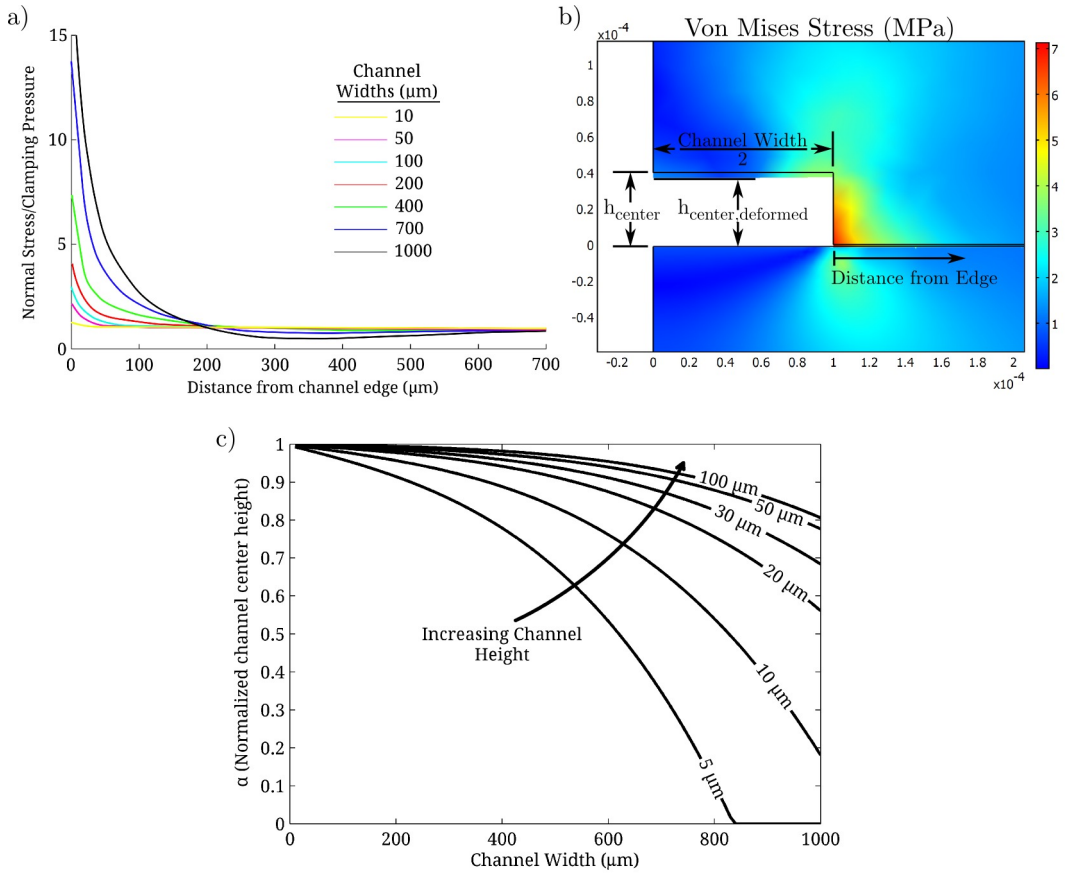

Figure 3.17: a) Normal contact pressure along the plastic contact interface as a function of distance from the channel edge for 15 μm high channels. For wider channels, the sealing pressure at the edges of the channel are many times that of the uniformly applied pressure of the clamp. b) von Mises stress plotted on the deformed shape. Graphical illustration of parameters used in analysis. c) Center channel deformation under varying channel width and heights. Deformation is plotted normalized to its starting height to show how much it deformed.

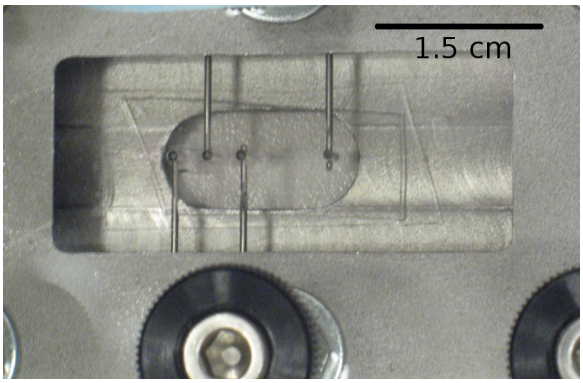

Figure 3.18: Device submerged in water and pressurized to the maximum leak test pressure of 15 bar. The rectangular device outline is free of bubbles and no leaks were detected.

syringe compression. The device is submerged in a glass dish filled with water. A syringe pump is used to increase the pressure in the device to the pumps maximum linear force, corresponding to 7 bar air pressure. Once the device is pressurized, the pressure is applied for a minute, and a picture is taken of the device to show that there are no bubbles. Once the syringe pump is maxed out, force is applied on the syringe with a vice to achieve the maximum tested pressure of 15 bar of air pressure. Even at this pressure, no leaks are observed and the syringe returned to its atmospheric pressure position, indicating no leaks. A photo of the submerged device at 15 bar is shown in Figure 3.18.

3.7.2 Fixture design

The fixture for applying mechanical pressure can be seen in Figure 3.15. It consists of a top and bottom 314 stainless steel pocket to provide mechanical integrity and clamping force, an acrylic fluid routing block, a gasket layer of silicone rubber gasket (McMaster-Carr), the unbonded device layer with features facing down onto a blank plastic film of the same type, and finally a glass slide to provide mechanical force onto the plastic devices.

To test devices, the gasket's holes are aligned with those of the fluid delivery block by eye, and the devices with fluidic passthroughs are then aligned by eye on top of this. The rest of the jig can be assembled requiring no other alignment

steps. The acrylic is held flat while the four bolts are inserted flat against the top steel pocket. A standard four bolt star pattern is used to evenly apply torque to the bolts in steps. Once tightened, the gasket can be observed to be evenly loaded around the devices. The fluidics can then be tested and discarded after use.

3.8 Injection Molding of future Devices

To move this device out of the laboratory and into actual devices only minor modifications will be necessary. For volume production embossing with a PDMS mold is not an ideal manufacturing method. Fortunately, the method is similar to and thus can be transferred to injection molding. Instead of low pressure and temperature embossing off a PDMS mold, a high pressure and temperature injection mold can be performed off of etched silicon masters. Alternatively, the mold can be machined into tool steel. The devices can also be implemented to fit into existing flow cytometers, negating the need for complicated detection systems. As such, the development of optical detection is largely ignored in this work instead opting for optical imaging with fluorescence microscopes.

3.9 Future Miniaturization of System

This device could be implemented into a traditional flow cytometer or a more recent microfluidic flow cytometer (Guava). However, if sensitivity can be disregarded in favor of portability the entire system can be miniaturized and implemented in a small standalone package.

Since the need for bulky and control intensive syringe pumps is eliminated by chip resistance flow rate control, the pumping force can be provided by small compressed gas cartridges or miniature compressors powered by lithium batteries. The optics and detection can be accomplished with modern LED filter blocks and some focusing optics onto a simple sensor. The sensitivity and accuracy as compared to a flow cytometer will be reduced by this approach, but the size of the package can be reduced to approximately 8x4x3 cm. This could then be used to assay single cells in the field for infectious diseases such as malaria.

Chapter 4

Fluidics: Design and Characterization

4.1 Background

In this section the fluidic design of the devices will be outlined. Some of these insights are commonly used in microfluidics today, and some are more optimized for this particular device. When compared to other droplet microfluidic works, this design is only functional at a specific design point with a steep drop off in functionality if any one of the parameters is allowed to vary. These parameters are fluidic (interfacial tension, surfactant diffusion speed, viscosity), geometric (shear rate in sorting channel, location of sorting spar), and motive (syringe pump versus pressure driven flow) dependent. The following sections will discuss in detail the critical features of the design.

4.2 Viscosity Measurements

Viscosity of the fluids is an important measurement with regards to the following fluidic design sections. Many works neglect the addition of surfactant, but at higher surfactant concentrations the effects cannot be ignored. Since the surfactant concentrations can be high in this system and the viscosity of the surfactants is high compared to the solvent, some increase in bulk viscosity must be measured and accounted for. In this section a method for testing the viscosity of small amounts of fluid is developed.

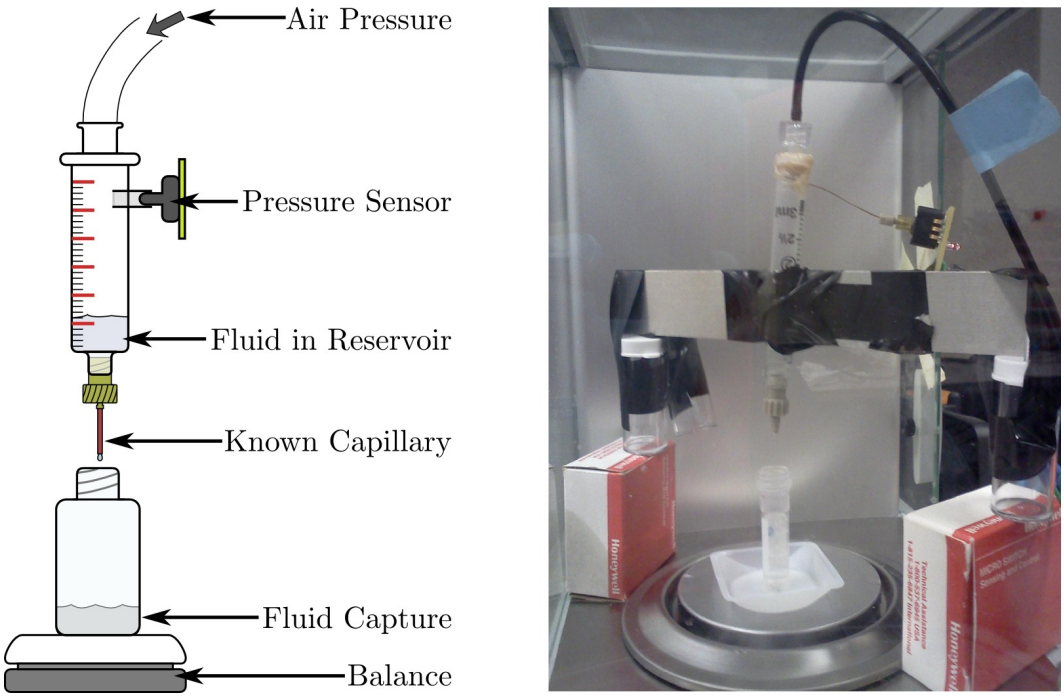

Figure 4.1: Schematic and photo of the viscosity testing apparatus.

4.2.1 Test Setup for Measurement

Many methods of testing fluid viscosity exist, but in this work a method is developed using common laboratory equipment. Several of the fluorinated oils of interest are expensive to the point that the use of small quantities for testing is preferred. The basis of this measurement is using a known pressure to force some small quantity of our liquid through a capillary of known dimensions and getting the flow rate from the mass increase on a balance catching the fluid as it comes through. Figure 4.1 shows both a photograph and a schematic of the setup.

The first component is a pressure source. This is a precision 0-100 kPa precision regulator (McMaster) connected to the building air line (≈400 kPa). This is connected to a fluid reservoir modified from a 3 mL BD plastic syringe. There is a static pressure tap leading to a Honeywell 0-100 kPa pressure sensor with 1% FS accuracy. The capillary is placed in a LabSmith capillary to Luer-

Lock fitting into the reservoir. The capillary is 150 μm ID glass capillary and is cut with a flat stone. The length of this capillary as measured with a dial caliper is 1.18 cm. It should be noted that the pressure drop of the capillary is much more dependent on the ID of the tubing vs the length of the capillary. The scale is a Denver Instruments balance with the ability to report its state via a RS232 connection. Code was written in Python to query the scale at particular time intervals and log the current mass reading to a file on an external computer. The viscosity (μ) of a sample can be determined by

$$\mu = \frac{\Delta P \pi d^4}{128 L Q} \tag{4.1}$$

where ΔP is the recorded pressure in the reservoir, d is the diameter of the capillary, L is the length of capillary, and Q is the volumetric flow rate of the fluid. The volumetric flow rate is found by dividing the mass flow rate obtained from the balance data by the density of the fluid.

4.2.2 Calibration of Setup

Since this method is sensitive to the inner diameter of the capillary (d^4) the true inner diameter is first found for meaningful results. The fluid used for calibration is DI water. It is also important to note the temperature at which the measurements were taken. To calibrate the expected values of viscosity we use data by Kestin *et al.* [65]. A single thermocouple is immersed in the liquid to take the temperature prior to testing. A summary of the data collected can be found in Table 4.1. This data is presented as processed after the diameter of the capillary is back-calculated from the expected values of viscosity. This was done by minimizing the errors from the experiments, and using the error-minimized diameter (148.7 μm) for calculations of viscosity. It should also be noted that as integration time of the data increases, the error decreases. This is expected as the liquid does come out as drops instead of a continuous function. We see from this data that further experimentation should integrate over 5 min or more if possible. Finally, the Reynolds number for the water calibration is around 100, and for the further oils it is one or less so turbulent effects are not present.

Table 4.1: Summary of water calibration results after the diameter of the capillary was determined. Pressure was near 7 kPa for each test.

Test -	T deg C	Time s	Expected Viscosity mPa·s	Measured Viscosity mPa·s	Error -
1	22.5	33	0.951	0.926	2.60%
2	22.5	61	0.951	0.967	1.64%
3	22.5	36	0.951	0.985	3.53%
4	22.5	38	0.951	0.985	3.53%
5	23.4	321	0.933	0.932	0.09%

4.2.3 Viscosity Results

Two sets of viscosity results are of interest. This data will be collected for both oil/surfactant systems at varying surfactant concentrations to be able to accurately calculate capillary number of the systems in operation. The data is presented in Table 4.2 and a plot is in Figure 4.2. At low concentrations the surfactant is not present in sufficient quantities to increase the viscosity of the entire solution. Past 2% the increase begins to become noticeable in the viscosity results. These values are an important part of determining capillary number, and without them the non-dimensional analysis performed here is less meaningful.

The relation between viscosity and weight percent of these solutions is expected to be exponential. As such, an exponential curve for both systems characterized here is also presented in Figure 4.2. The exponential model fits well, and intermediate values for viscosity can be interpolated.

4.3 Interfacial Tension Measurements

Interfacial tension is one of the most overlooked parameters in two phase microfluidics today. Even reported values of interfacial tension are ambiguous and are often just the equilibrium interfacial tension of two mixtures. This assumes that the interface is of a sufficient age for the surfactant to have fully saturated the interface to its final state. The assumption is often wrong, be-

Table 4.2: Summary of measured viscosities from capillary measurement.

Oil/Surfactant -	% Surfactant % w/w	T deg C	Measured μ mPa·s	Density kg m^{-3}
FC70/Krytox	0.00	23.2	24.8	1940
FC70/Krytox	0.10	23.2	25.0	1940
FC70/Krytox	0.25	23.3	25.1	1940
FC70/Krytox	0.50	23.3	25.8	1940
FC70/Krytox	1.0	23.3	27.8	1940
FC70/Krytox	2.5	23.3	32.7	1939
FC70/Krytox	5.0	23.4	40.3	1938
FC70/Krytox	10	23.4	56.6	1936
FC70/Krytox	25	23.4	118	1930
FC70/Krytox	50	23.4	415	1920
Peanut/SPAN80	0.00	23.8	69.1	915
Peanut/SPAN80	0.10	23.8	62.4	915
Peanut/SPAN80	0.25	23.8	68.4	915
Peanut/SPAN80	0.50	23.8	66.4	915
Peanut/SPAN80	1.0	23.9	65.8	916
Peanut/SPAN80	2.5	23.9	64.7	916
Peanut/SPAN80	5.0	23.9	70.5	918
Peanut/SPAN80	10	23.9	74.8	920
Peanut/SPAN80	25	24.0	94.4	928
Peanut/SPAN80	50	24.0	170	940

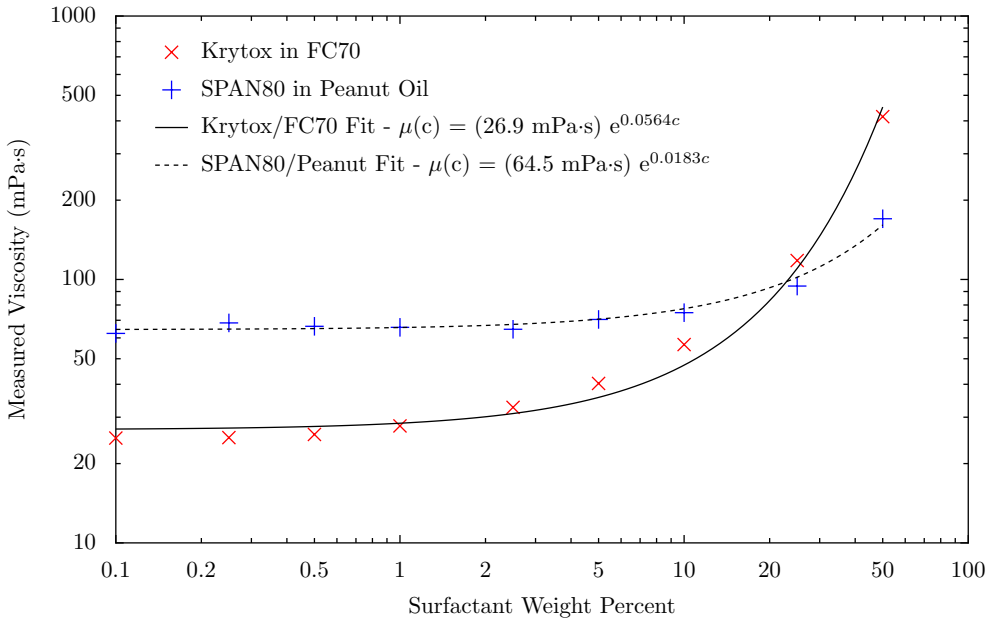

Figure 4.2: Plot of viscosity vs. weight percentage of surfactant.

cause the timescale of generation is so short for most droplet works, especially this one.

Some studies have tried to classify the dynamic effects of surfactants in droplet generation on chip, but it is an exceedingly difficult parameter to measure. Most report some sort of average interfacial tension, while not accounting for any transient effects in the system [66; 67; 68; 69; 70]. Some of these studies examine transient effects, but choose effects that are easy to measure, such as when a surfactant laden droplet enters a region of high shear. The critical surfactant migration when an interface is rapidly formed is neglected. One study stands out [71] in that they make a calibration curve with pure liquids and then compares surfactant laden systems with the calibration curve to more accurately look at effects of surfactant migration at the region of the breakup. By varying the flow rates the timescale of droplet generation can be modified and the apparent interfacial tension at breakup can be analyzed. Their results don't add much of quantitative value, but the qualitative results are important. They find that during generation the droplet size will be between the equilibrium value and pure liquid value of interfacial tension, which is somewhat intuitive. This timescale to the minimum interfacial tension can be shortened by increasing the surfactant load to decrease the distance surfactants need to travel to adsorb to the interface, increasing the Reynolds number to speed convection, or increasing the Sherwood number defined as

$$Sh = \frac{K \cdot L}{D}$$

where K is mass diffusivity, L is a length, and D is diffusive mass transport. In a microfluidic device they find that the convective terms dominate, so using a diffusive testing method such as the one covered below will overestimate the interfacial tension at the interface. It is shown however, that as a qualitative measure of speed with the interface is saturated a diffusive method of measurement is valuable.

This type of transient measurement of droplet interfacial tension at the point of breakup is a project unto itself, and a qualitative approach to interfacial tension will suffice for this application. Because of its ease of use a pendant drop measurement will be used to assess the diffusive aspects of surfactant migration. If these same time scales were used to actually generate interfacial tension values, the results would be overestimated from the actual value.

4.3.1 Setup

To take these measurements, a test fixture is created to take pendant drop measurements. In this method, a side image of a drop hanging from a flat tipped needle is taken with a camera. By calculating geometric properties of the drop, the interfacial tension can be found by balancing vertical forces across a horizontal plane. The method works on static drops and assumes no motion. Determining interfacial tension by this method can be traced back to work performed by Bashforth and Addams [72]. This work lays the groundwork for the method, but a more applied version of the work along with a measuring apparatus is offered by Andreas [73]. By equating pressure force (p) due to the pricipal radii of curvature (R and R') and interfacial tension (γ) at a location it can be seen that:

$$p = \gamma \left(\frac{1}{R} + \frac{1}{R'} \right)$$

Alternatively, this can be written as a radius of curvature of the bottom of the droplet (b) along with a height (z), gravity (g), and difference in densities of the fluid ($\Delta\rho$) as:

$$p = \frac{2\gamma}{b} - g\Delta\rho z$$

Once these are equated and the radii of curvature cancelled from the equation, a second order differential equation for the profile of the drop can be obtained. To back calculate the interfacial tension from this differential equation, one would have to know the exact interface profile and iterate over the parameters in the problem to find the interfacial tension. Instead, they pose the problem as a ratio involving an equatorial diameter (De) and shoulder diameter (Ds) on two different planes. These diameters are illustrated graphically in Figure 4.3 b) on an actual image used in this experimentation. The equatorial diameter is the largest diameter of the drop through which a horizontal plane crosses. The shoulder diameter is then calculated as the diameter of the drop at a horizontal plane that is one equatorial distance from the bottom of the drop. An effective two point profile of the drop can then be determined by the shape ratio (S) of $S = Ds/De$. A table for H ($H = \beta(De/b)^2$) is then compiled by solving the differential equation for varying values of S as a lookup table. This simplifies the equation to:

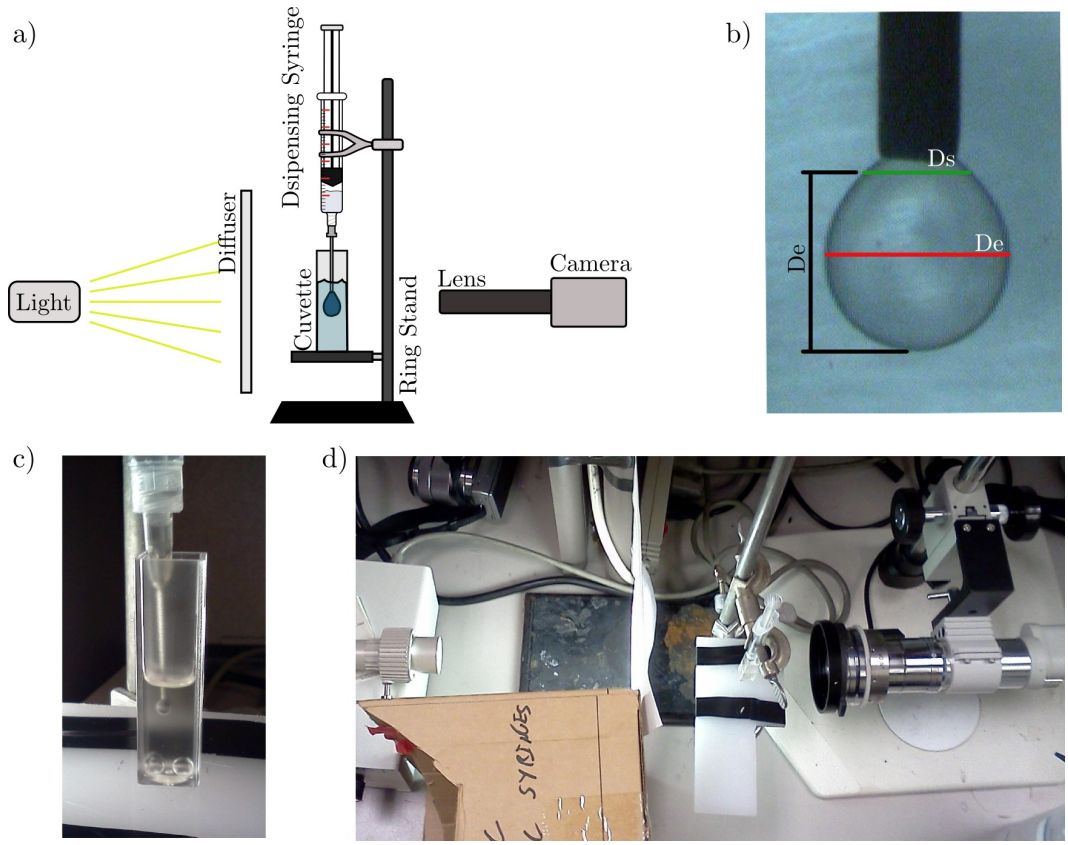

Figure 4.3: a) Schematic view of interfacial tension measurement. b) Sample image obtained during testing. The equatorial diameter (De) is marked in red, then the shoulder diameter (Ds) is one equatorial diameter up from the base of the drop. c) Image of a pendant drop in the cuvette. Note the two sides of the 2 mL cuvettes are frosted and the other two clear. d) Overall setup used for interfacial tension measurements.

$$\gamma = \frac{\Delta \rho g D e^2}{H}$$

Since we know the densities of the liquids and the value for gravity, we just need to find the equatorial diameter and H from geometric values of the pendant drop for gamma.

Experimental testing of these parameters is covered below. To obtain the geometric shape, the apparatus in Figure 4.3 is assembled. On the left is a light source shining onto a diffuser. The cuvette is placed on a ring stand below a 1 mL plastic Becton-Dickinson plastic syringe with a 22 gauge hypdoermic needle affixed. The needle tip is ground blunt with a rotating abrasive tool, then the edges sanded with 600 grit emery cloth to clean off rough corners. The tip of this needle is measured at 0.712 mm with dial calipers. This value is needed for the calibration of distances in the images. On the right of the image is a side facing camera and microscope lens. The backlighting provides good contrast for further processing of the images.

Next the cuvette is filled with 1.5 mL of the less dense liquid in the combination of immiscible fluids to be tested. If the denser phase is used instead, the droplets formed will float and not hang down from the needle. The syringe is washed with ethanol in between uses, and dried by running compressed air through it. It is then filled with the denser phase of liquid for the test. It can then be attached to the ring stand above the cuvette. The camera is set to record video at 25 FPS and the backlight turned on. While video is running, fluid is dispensed to form the largest possible droplet that will not fall off the needle from its own weight. For each aqueous/oil combination approximately 10 droplets are recorded. The video is cropped by defining the beginning as when the drop is no longer increasing in size from dispensing to the end when the drop either falls from decreasing interfacial tension or reaches its minimum interfacial tension.

To process each image of the video, first the width of the needle at the top of the frame is found in pixels. This value is converted to a scale knowing that the width of the needle is 0.712 mm. The equatorial diameter is found as the widest part of the drop, then the shoulder is calculated at one equatorial diameter up from the bottom of the droplet. The time is recorded as the frame number from the time defined as the beginning of the video multiplied by the reciprocal of the frame rate.

4.3.2 Calibration

To calibrate the data, we can look at the values we obtain for FC70 vs DI water. With no surfactant present in the system, it is assumed that the interfacial tension should be constant for the drop for all the times it is hanging. The reported value of interfacial tension between FC70 and DI water is 64 mN/m, and from our measurements we obtain 64.5±0.2 mN/m or approximately 1% error. To convert the pixels of the image into lengths, we use the pixel value of width of the needle in the image and measure the diameter with dial calipers as 0.712 mm (Nom. 0.717 mm). Since the method is most strongly dependent on geometric measurement of the droplet shape, this error is expected to be contributed from the camera and lens combination. More accuracy could be obtained with better imaging devices.

4.3.3 Results

First we are interested in a fatty acid and DI water system. The fatty acid chosen is peanut oil (Sigma) and the oil-phase surfactant used is sorbitan monooleate (SPAN80, Sigma). We can examine the effects of surfactant addition by making a serial dilution of surfactant from 50% w/v SPAN80 in peanut oil down to 0.1%. The results can be found in Figure 4.4. The interfacial tension between pure DI water and peanut oil is given by literature as 22.8±0.8 [74]. If we examine the data in Figure 4.4 we see that at time 0 s, immediately after droplet formation, the interfacial tension is approximately the same as this pure liquid value. With increasing surfactant loading, the time required for decreasing the interfacial tension decreases until a certain point (between 2.5p and 5p SPAN80). This is because with increasing surfactant concentration, more surfactant is closer to the interface and thus requires less time to diffuse to the interface and act to lower the tension. After 2.5p SPAN80, we see that the line overlays 5p. This is past the critical micelle concentration (CMC) of this system. Once enough surfactant has been added to a solvent, there is a point where it is more energetically favorable for the ampiphilic molecule to turn its head groups together to form micelles of surfactant. Once these micelles are formed and move to the interface, they will fully saturate the interface much faster, and that is the lower limit of surface tension available for that system. In this case, we can see that this lower limit of IFT is approximately 0.8 mN/m.

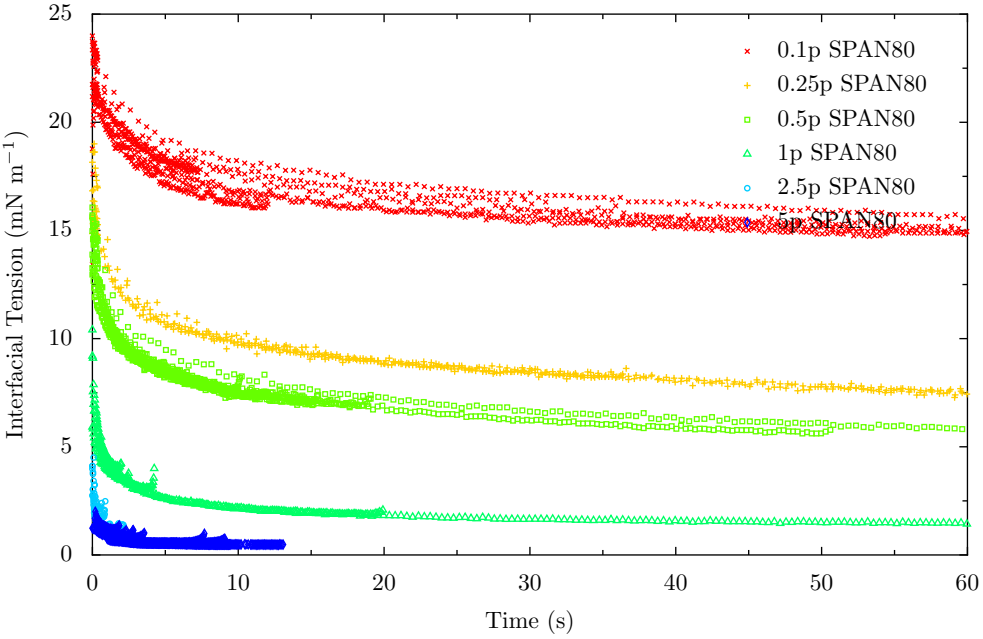

Figure 4.4: Interfacial tension versus time plot of peanut oil with varying weight percentages of SPAN80 surfactant. Aqueous phase is DI water.

It is important to note that these time scales represent mainly diffusive effects of the surfactants. Other works [71] have shown that this data is qualitatively useful, but convective effects in microfluidic devices will shorten the time constant required for the interfacial tension to drop from the pure liquids value to the final value. This data is still useful for finding the minimum possible interfacial tension, along with a qualitative comparison of some of the adsorptive mechanics of the surfactants at the interface.

One downside of the previously mentioned peanut oil/SPAN80/DI water system is that the SPAN80 is autofluorescent. This can be seen by pipetting 5 µL of both DI water and peanut oil with 10p SPAN80 onto a glass slide then putting a cover slip on top to verify that the layers are not too thick. Figure 4.5 shows that when imaged with visible light the phases can be distinctly seen, but under UV excitation and filtering of the same field of view clear autofluorescence can be seen. This is a distinct problem in that this autofluorescence may easily overpower fluorescent probes that are being used on the cells inside of drops.

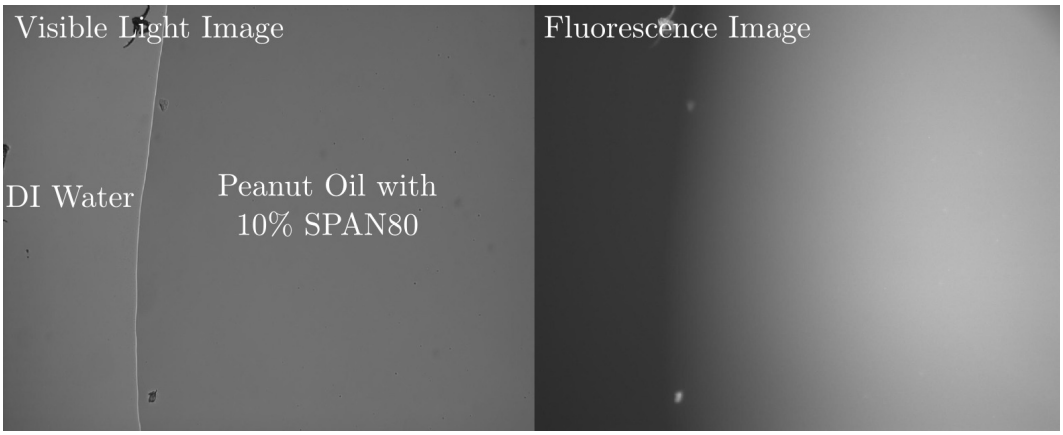

Figure 4.5: Image showing autofluorescence of peanut oil/SPAN80 mixture. The two phases are sandwiched between a glass slide and a cover slip.

The fluids were allowed to sit for 10 min on the slide and no migration of fluorescence was seen, implying that the surfactant is staying in the oil phase. We can try to mitigate this issue by achieving the same minimal interfacial tension by adding a separate, non-autofluorescent surfactant to the aqueous phase of the system.

To attempt to achieve the same lowered interfacial tension as the CMC of the SPAN80 and peanut oil system, a separate surfactant can be added to the aqueous phase. Pluronic F68 is chosen for this as a non-auto-fluorescent surfactant. Figure 4.6 shows the results of using this surfactant laden aqueous phase. The addition of this molecule shows no changes versus the system not containing F68. This indicates that the molecule is not being recruited at the interface or acting as intended. For further testing, minimizing the amount of SPAN80 use to 2.5p or less is the only action against this autofluorescence.

The other system tested is based on a fluorinated oil, Fluorinert FC70. Two surfactants are used in the different phases. Pluronic F68 (Sigma) is used as a surfactant in the aqueous phase and Krytox 157FSH (DuPont) is used for the oil phase. First the effects of just the Krytox in FC70 will be examined. The test is performed in the same manner as those done on peanut oil, and the resulting transient curves can be seen in Figure 4.7. In this case, the pure FC70 and DI water system was tested, and it can be seen that the value of interfacial tension was constant throughout the time tested. Note that this

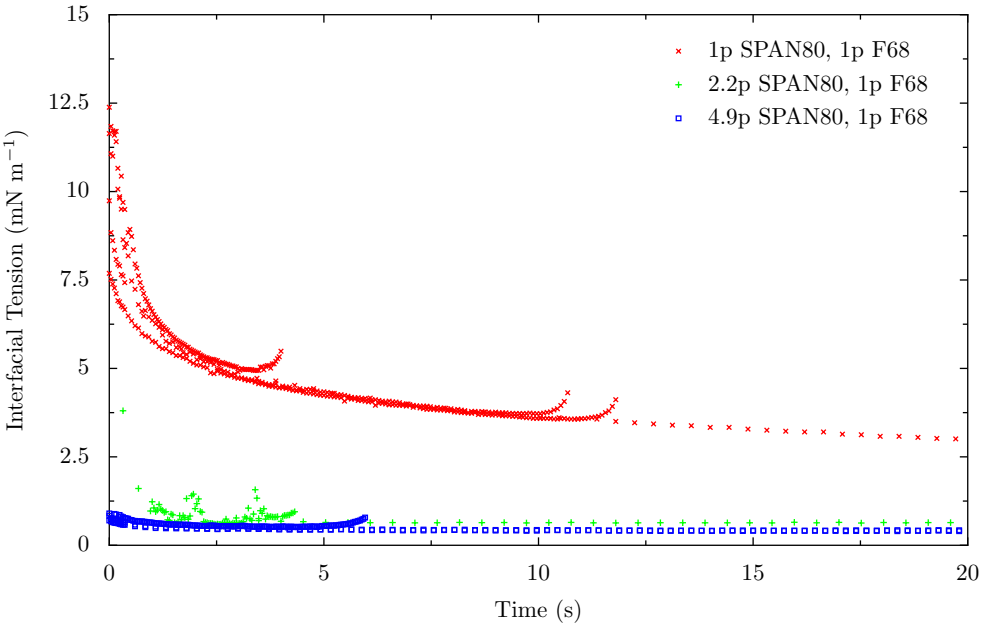

Figure 4.6: Interfacial tension versus time plot of peanut oil with varying weight percentages of SPAN80 surfactant. Aqueous phase is DI water with 1p Pluronic F68.

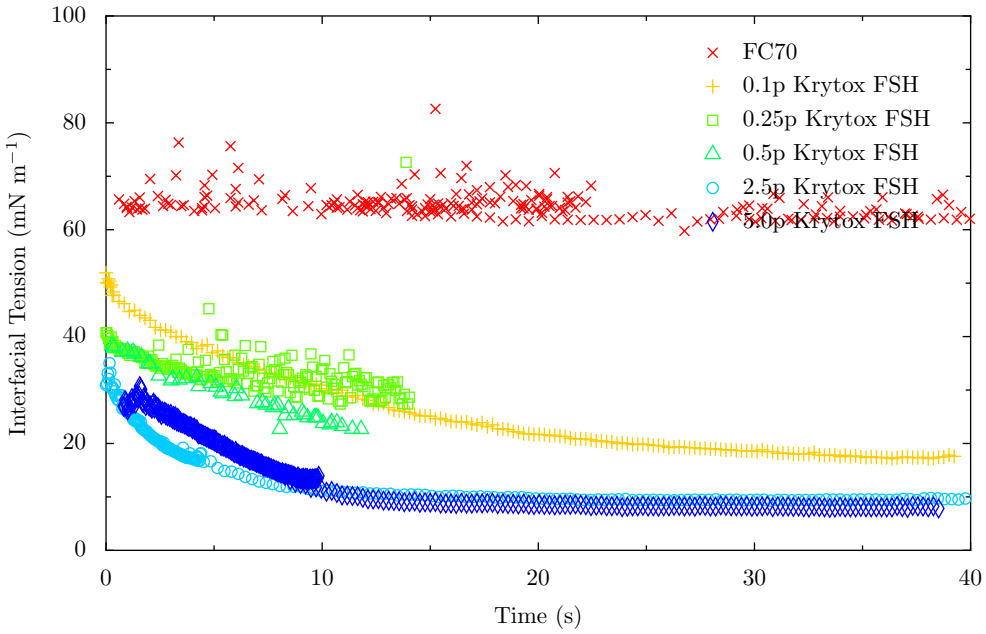

Figure 4.7: Interfacial tension versus time plot of Fluorinert FC70 with varying weight percentages of Krytox 157 FSH surfactant. Aqueous phase is DI water.

data is noisier than previous data for two reasons. First, water is placed in the cuvette instead of the oil because in this system, the oil is more dense (SG=1.940) and is placed in the syringe. This combination and similar index of refraction means the contrast of the resultant images is poorer than that with peanut oil. Second, this additional density also means that the droplets are smaller and that amplifies any geometric errors that are picked up during processing.

The resulting system with increasing amounts of Krytox surfactant shows similar trends to the peanut oil system. Increasing the surfactant concentration decreases the interfacial tension and decreases the time constant necessary to get there. The data is also of shorter length in time for these tests since the droplets that were formed often fell off the needle once the interfacial tension became too low. The CMC for this system is between 2.5 p and 5 p Krytox, and the minimum interfacial tension is approximately 8.2 mN/m.

The next sweep performed is again varying the Krytox concentration, but

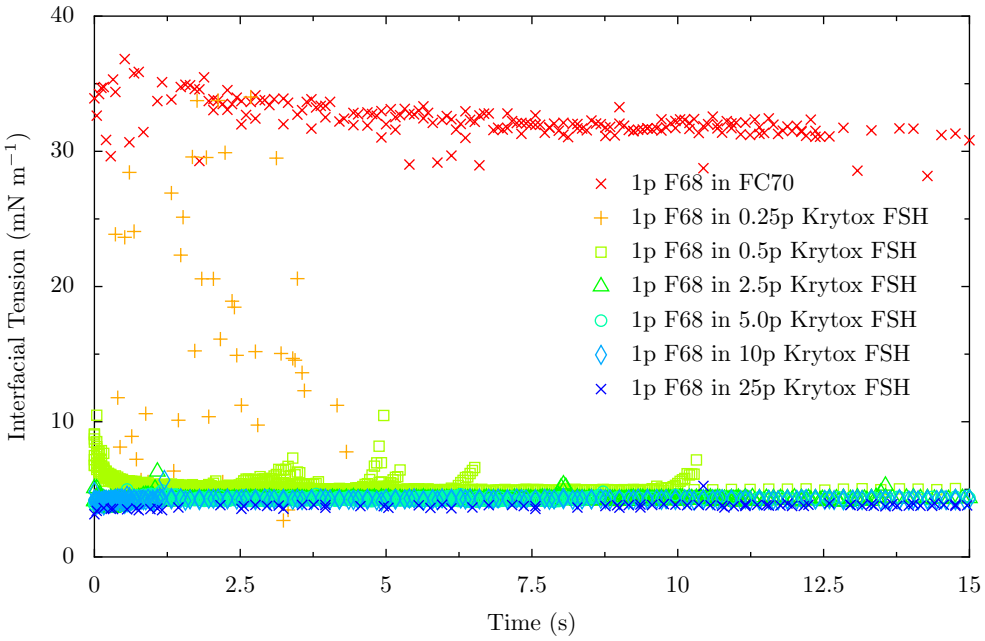

Figure 4.8: Interfacial tension versus time plot of Fluorinert FC70 with varying weight percentages of Krytox 157 FSH surfactant. Aqueous phase is DI water with 1p w/v of F68.

using a 1 p solution of Pluronic F68 in the aqueous phase. The data can be seen in Figure 4.8. For this test, the time constant is nearly too fast for this system to measure. However, when just Pluronic is present with no Krytox in the oil phase, the time constant is slow and the resultant decrease in interfacial tension is low. We can see that the Pluronic is a much faster surfactant than just Krytox alone. Some interaction between Krytox and Pluronic is also responsible for lowering the final interfacial tension to 3.5 mN/m and making the time constant extremely fast from diffusion alone.

If we then hold the amount of Krytox in a sample constant at 10p and vary the concentration of Pluronic, we can see what a reasonable value is and find the CMC. This data is given in Figure 4.9. We see that even small amounts of Pluronic (0.01p) make the system response too fast for this measurement method. It can be seen that the CMC is around 1p, but this particular test may not have tested high enough concentrations of Pluronic to actually spot

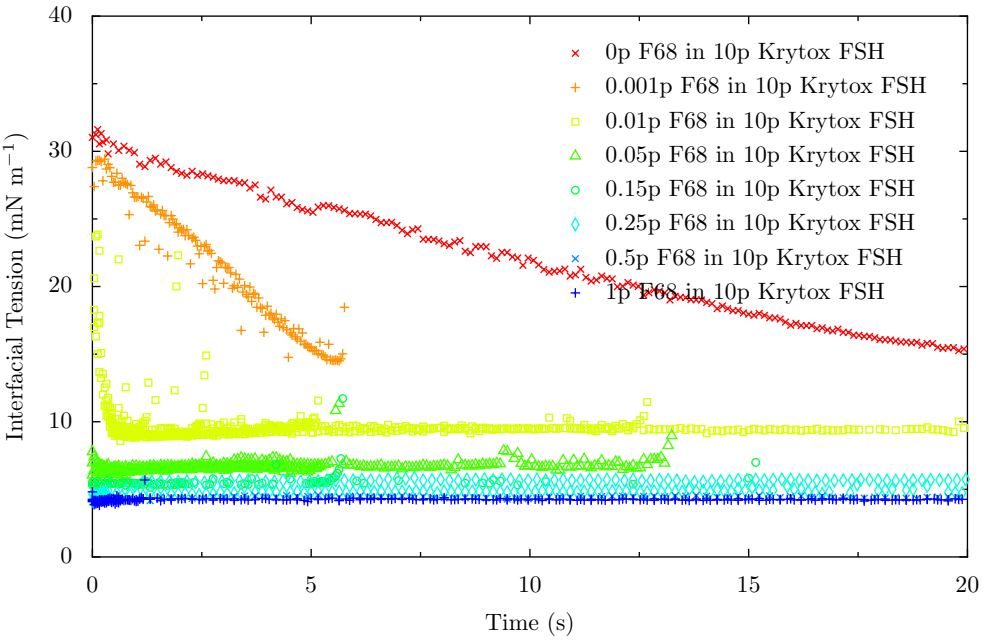

Figure 4.9: Interfacial tension versus time plot of Fluorinert FC70 with 10p by weight Krytox 157 FSH surfactant. Aqueous phase is DI water with varying weight percentages of F68.

the exact CMC. The minimum observed interfacial tension here is 4.2 mN/m.

4.3.4 Discussion of Transient Effects

The data collected here is applicable to systems where diffusion of surfactants is the only transport of surfactants to the interface. This will not be the case in a microfluidic system, but obtaining values for this in a microfluidic device has not yet been accomplished satisfactorily due to the complexity and difficulty. This simple macroscale approach allows us to judge the speed of interface surfactant saturation from a qualitative viewpoint, and strong convection in a microfluidic device will just decrease the time required for full saturation of the interface. The Sherwood number (Sh) can be calculated to verify the dominance of convection, as it is the ratio of convective to diffusive mass transport [75]:

$$\mathrm{Sh} = 1.615 \left(\frac{VH}{D} \right)^{1/3} \tag{4.2}$$

where V is the velocity of the flow, H is the characteristic length of the channel, and D is the diffusion constant of the surfactant.

Using typical values from this device, V is 8 cm s^{-1}, H is 50 μm, and a characteristic diffusion coefficient in liquids for large molecules such as surfactants is $1x10^{-6}$ cm s^{-1}. This yields Sh = 55.2. This shows that convective effects are very dominant in the droplet generation region, and the interface should stabilize rapidly. This Sherwood number is twice that in experimental literature [71] where it was shown that the timescape of interface stabilization is much more rapid than that of droplet generation.

For calculations of capillary number, we have no choice but to assume that the interface is fully saturated, and that the interfacial tension is its minimum value. This assumption is better justified in this droplet generator than others due to the geometry of the droplet breakup. Since the capillary number is so high, the interface gets stretched for a long while before the tip of the stretched region breaks off. The carrier oil is flowing rapidly past this interface at a much higher flow ratio, so by the time this breaks up from Raleigh-Taylor instabilities the interface should have had enough convection to be fully surfactant laden.

4.3.5 Surfactant Shells on Drops

An unexpected result occurs at high concentrations (greater than 25p) of SPAN80 in Peanut Oil. After a drop is allowed to remain in a constant shape with no convection for a time period of 41 s, a mechanical shell forms on the surface. This shell, once assembled, is strong enough to overcome the interfacial tension forces which are quite low at this concentration of surfactant. A visual of this phenomena is shown in Figure 4.10. Figure 4.10 a shows the shell being formed. At rest, the shell bunches in section where tension on the interface stretches the skin in only one direction, causing ripples.

When the shelled drop detaches from the needle, the shell allows it to keep a pseudo-pendant drop shape rather than returning to a circular shape. Figure 4.10 b) and c) illustrate this effect. Both of these drops were formed in the same 25p SPAN80 solution, the difference being that in b) the droplet remained static for 41 s and droplet c) detached after 1 s. It is clear that the mechanical shell enables this droplet to hold its shape.

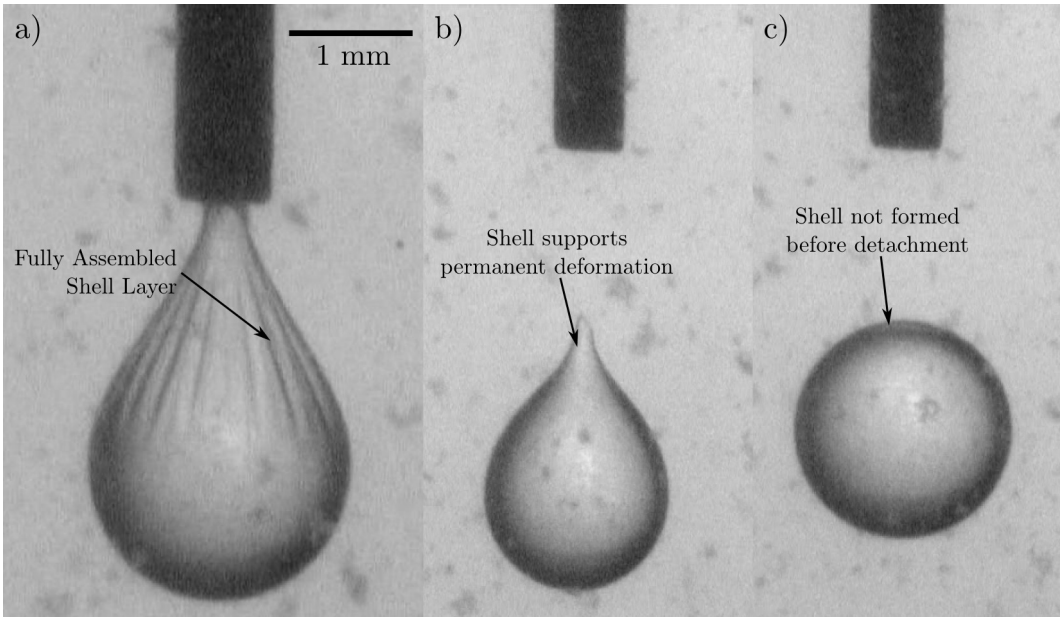

Figure 4.10: a) Shell assembled on surface of droplet after 41 s of stagnation. Droplet is DI water, oil is 25p SPAN80 in Peanut oil. b) Shell formed droplet holding deformation after release from needle. Shell can support mechanical loads. c) Same liquids, but droplet released 1 s after formation.

This phenomena is useful for droplet microfluidics for preventing recoalescence. To form this shell, it is important to keep the shear rate around the droplet low to allow for the surfactant to remained absorbed and form a lattice with its nearest neighboring surfactant molecules. The design of the devices is of such to allow the encapsulated cells to form the beginnings of these shells prior to contact with other droplets. As long as the droplets do not coalesce in the outlet wells, this shell will aid in keeping the droplets separate throughout any post-device processing steps.

4.4 Dimensional Analysis

4.4.1 Derivation to Important Parameters

The problem of the sizes of empty droplet generation can be approached from a dimensional analysis perspective. While the underlying phenomena for breakup, namely the Raleigh-Plateau instability in the necked jet [76] is complicated, this method can provide a useful method for determining the flow regime. Since the specifics of the breakup in the locally high and low pressure regions is not of interest, this analysis is more than adequate to obtain the information which we are interested in. We begin by analyzing what is important in this particular problem.

The velocity of the carrier fluid is much higher than that of the dispersed phase, and the viscosity much higher so the viscosity of the carrier fluid (μ_o) is an important parameter. The interfacial tension (γ) governs the contribution of the interface between the two fluids. It is important to note here that this parameter is not a constant, and is transient as surfactant diffuses to and saturates the interface. This effect is discussed further in the section on surfactants, but we will consider the final interfacial tension value to be the value of this parameter. The width of the shear channel (w) that the dispersed phase is entering is important to the constriction of the interface, as is the mean velocity (V) of the fluid in that channel. The mean velocity can be found by summing the flow rates of both phases and finding the average velocity in the shear channel. Finally, the parameter that will determine the empty droplet size is the diameter (d) of the dispersed phase prior to fluidic breakup. All of the parameters of interest are illustrated in Figure 4.11. The blue region represents the dispersed phase entering from the left, and the carrier phase

enters the top and bottom inlets.

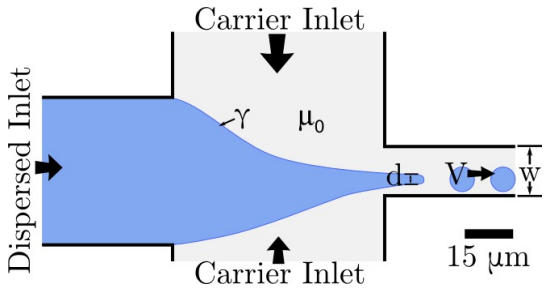

Figure 4.11: Parameters of the problem important to the dimensional analysis

Looking at these parameters we find the following dimensions of the parameters of interest.

Parameter		Units
d	:	m
w	:	m
V	:	$\frac{m}{s}$
γ	:	$\frac{N}{m} \rightarrow \frac{kg}{s^2}$
μ_c	:	Pa*s $\rightarrow \frac{kg}{ms}$

Table 4.3: Dimensions of important variables

With five parameters and three units, the Buckingham-Pi theorem tells us that we must assemble two dimensionless groupings. These are:

Examining these parameters, we see that Π_1 is actually just capillary number (Ca), or the ratio of viscous forces to interfacial tension. This is expected, as this is a number that other studies have found useful for droplet analysis. The second pi group, Π_2, is the ratio of necked diameter of the dispersed phase to the width of the shear channel. Π_2, however, is a difficult value to measure in a functioning device due to resolution limits of the camera sensors paired with objectives that allow enough light for high speed video. Instead, we can substitute a more easily measurable ratio instead. If there is a necked diameter

Pi Group		Expression
Π_1	:	$\frac{\mu V}{\gamma}$
Π_2	:	$\frac{d}{w}$

Table 4.4: Dimensionless π groups formed by Buckingham-Pi

in the shear channel in the current regime of device operation, Π_2 is ideally just the ratio of flow rates of the dispersed phase to the carrier phase. This assumes that the flow is at steady state and that the necking region is static. This condition can be broken if the droplets break up in the shear channel before the necking region (as in low Ca flow). This yields the following substitute ratio where Q_c is the flow rate of the carrier fluid and Q_d is the flow rate of the dispersed fluid:

$$\Pi_2 = \frac{d}{w} = \frac{Q_d}{Q_c} \tag{4.3}$$

Using these two parameters, a set of experiments that vary these two critical parameters can be run to figure out a design algorithm for the creation of devices. The goal of this analysis is to find a regime where the empty droplets are of a size that is different enough of a cell containing droplet to allow for sorting of the two. This is when an empty droplet diameter (a) generated is less that 0.2 of the channel hydraulic diameter (D_h), or $a/D_h < 0.2$. The capillary number can be varied in a few different ways. First, the flow rates of the dispersed and continuous phases can be increased while keeping the flow ratio between the two fixed. Second, the viscosity of the carrier phase fluid can be increased by substituting different oils. For this work, both fluorinated and fatty acid carrier fluids have been tested with viscosities varying from 1 mPa·s for FC770 to 50 mPa·s for peanut oil. Third, the interfacial tension can be reduced between the two phases to lower the amount of energy at the interface. This is accomplished with surfactants in either or both phases of the liquids.

To vary the flow rate ratio between the two phases the pressure applied to the dispersed and carrier phase inlets can be modified. To accurately determine the flow rate for the syringe driven tests, we must use video analysis to

determine the actual flow rate of the dispersed phase.

4.4.2 Discussion of Parameters

Some works [27] have found Ca to be a useful controlling parameter for droplet breakup, but not as many look at the flow rate ratio involved. Others [77] have arrived at this same set of parameters after more painstaking analysis. However, the bulk of approaches fail to look into insightful parameters and instead just report flow rates in their devices [29; 28; 78]. These parameters are device and geometry specific, and fails to convey design information for other droplet microfluidic works. Most works also don't mention this because for the most part these parameters are not important for their work. The conventional use of droplet microfluidics for "monodisperse" droplet generation just requires that parameters stay at one design point, with little insight into why that point is used. Additionally, most other droplet microfluidics operate in regimes where the capillary number is very low and disruptions in one of the two Pi groups do not influence the operation of the devices. That is not the case here, and the results of some select experiments will show how these parameters are important.

Π_1 can be modified by changing the amount of surfactant in the system, and Π_2 can be modified by changing the syringe pumps. Figure 4.12 shows the results of a swept parameter field. The capillary number was adjusted with three different surfactant systems, and the flow rate ratio was then varied within each of the three systems to get acceptably sized (less than 5 μm diameter) droplets.

4.5 Droplet Migration in Shear Flows

The previous section discussed making empty droplets small enough that there is a size difference between cell containing and non-cell containing droplets. This section will show how to exploit the size difference to provide passive sorting between these two distinct populations of droplets. It is important to note that the droplets are migrating due to deformations in the shape of the droplet. If the droplets kept a perfectly spherical shape as would be the case with high interfacial tension, no migration would occur.

The goal of this section of the device is to move large droplets to the center

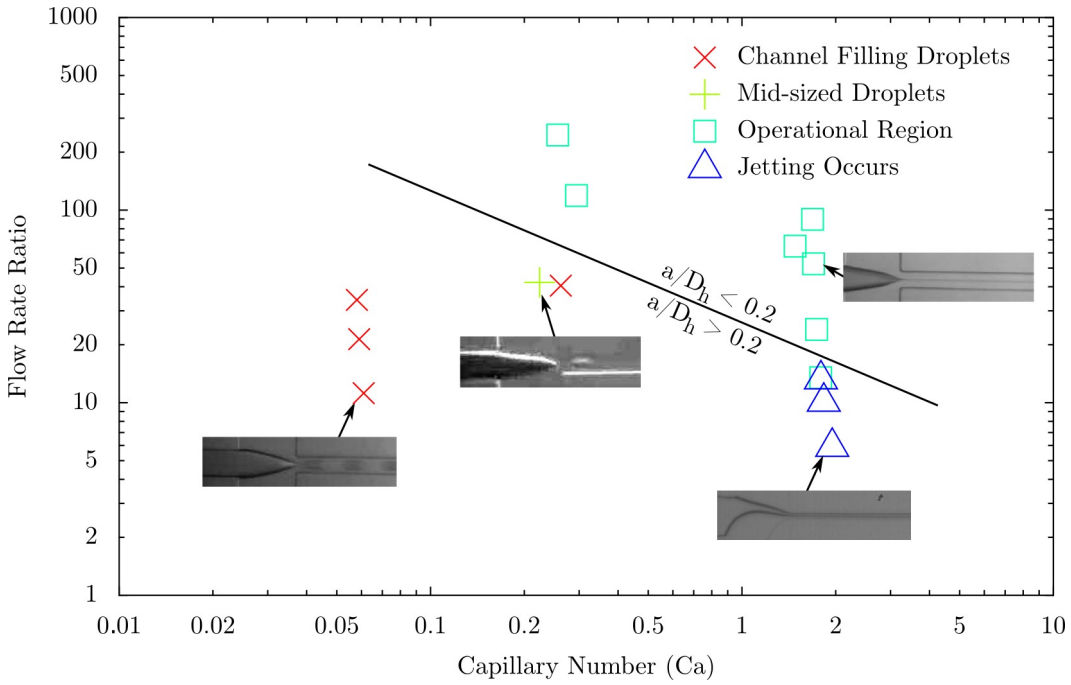

Figure 4.12: The parameters from dimensional analysis plotted with results from experiments. a is droplet diameter and D_h is hydraulic diameter of the channel.

of the shear channel while keeping smaller, empty droplets to one side. This will allow for sorting between the two populations. The migration of deformable drops in a shear flow was well characterized by Chan and Leal [79]. This work is long and tedious so the method will be summarized here. First the problem is formulated inside and outside of the drop. This work describes the motion of a non-Newtonian fluid, but neglecting the higher order fluid terms yields the Newtonian solution of interest. These are then solved to find the velocity profile of the fluid as if there were no droplets present in the channels. In this work both Poiseuille and Couette solutions are found. Using the method of reflections, the disturbed velocity profiles can be found now with droplets present in the flow. These velocity solutions can then be used to describe the deformed shape of the droplets in these flows, and also find the forces that are exerted on non-centered droplets at any given time.

Some important design notes can be found from this analysis. The migration (cross channel) velocity (U_m) of a 3D Poiseuille flow can be found from Equation 6.10 of Chan and Leal [79]:

$$U_m = -\frac{\beta\sigma}{(1+\kappa)^2(2+3\kappa)}\left[\frac{3}{14}\frac{16+19\kappa}{2+3\kappa}\left(1-\kappa-2\kappa^2\right) + \frac{10+11\kappa}{140}\left(8-\kappa+3\kappa^2\right)\right] \tag{4.4}$$

where $\beta = 4V_{max}(1-2s)\,\zeta$, $\sigma = -4V_{max}\zeta^2$, $\zeta = a/y$, $\kappa = \mu_{drop}/\mu_{carrier}$, V_{max} is the maximum velocity in the channel, s is the position of the drop in the width of the channel from 0 to 1, μ is dynamic viscosity, a is droplet radius, and y is the distance of a drop from the centerline of the channel.

Examination of Equation 4.4 gives considerable insight into how fast certain droplets will migrate inside of the shear channel. Parameter β shows that the migration velocity will increase when the flow is faster or when a droplet is closer to a wall of the channel. ζ compares the diameter of the drop to the distance from the centerline of the channel. As droplet diameter increases and as the drop is closer to the wall, the migration velocity will increase. It is difficult to see the relation for κ here, but increasing κ will lead to slower migration velocities. This is a result of either increasing the viscosity of the dispersed phase or decreasing the viscosity of the carrier phase.

This migration velocity can be integrated to get the trajectory of a specifically sized droplet in a length of channel. The result, equation 8.6 in Chan and

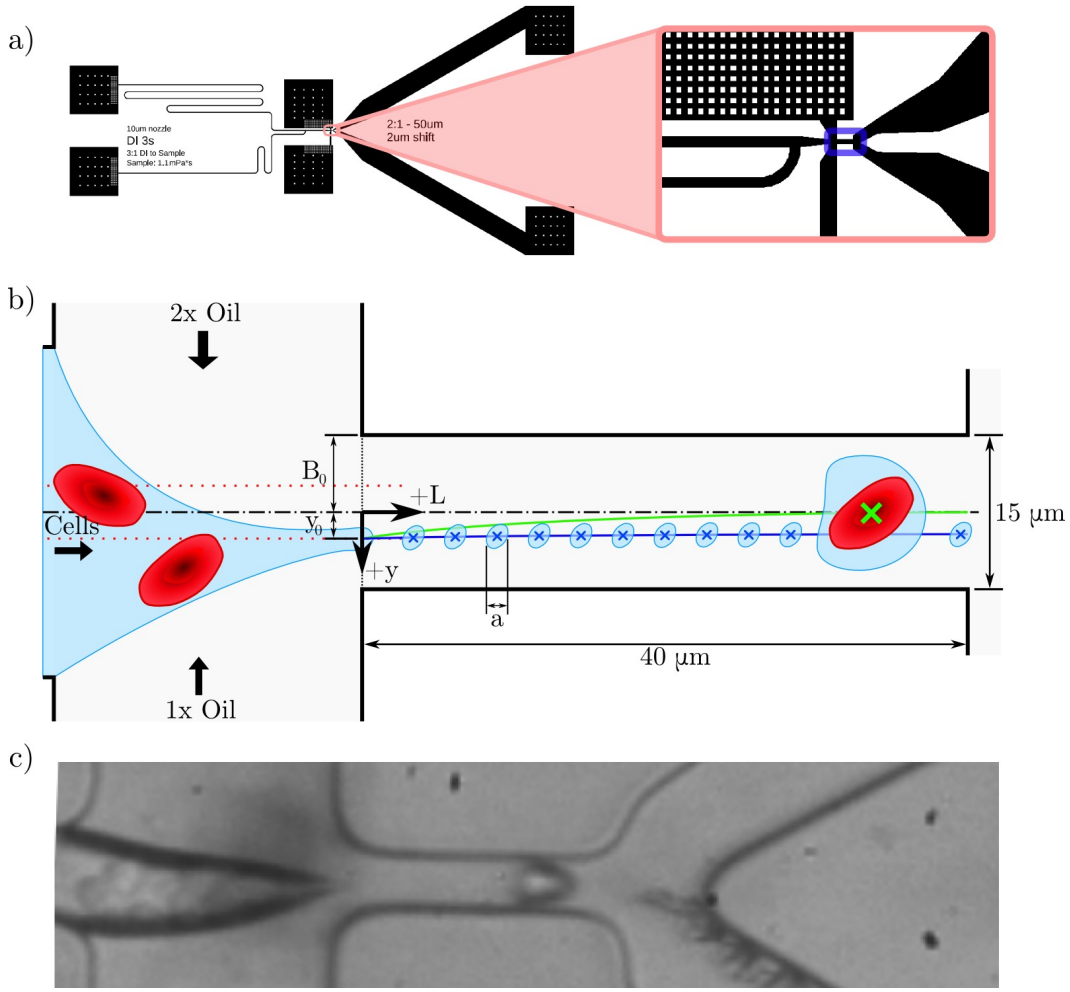

Figure 4.13: Droplet migration inside of the devices. a) Location of where migration occurs within the devices. b) A schematic illustration of important sorting parameters marked as written in Equation 4.5. Cell containing (larger a) droplets will follow the green trajectory, while empty droplets (smaller a) will follow the blue trajectory. The crosses mark the center of the droplets. c) Experimental image of droplet sorting with cells in a 10p weight SPAN80 in peanut oil system. Flow rate is 17 µL hr^{-1}.

Leal [79] is:

$$\left[\frac{y^2}{2B_0^2} - \left(1 - \frac{2\kappa}{2+3\kappa}\frac{a^2}{B_0^2}\right)\ln\frac{y}{B_0}\right] - \left[\frac{y_0^2}{2B_0^2} - \left(1 - \frac{2\kappa}{2+3\kappa}\frac{a^2}{B_0^2}\right)\ln\frac{y_0}{B_0}\right]$$
$$= \frac{2V_{max}a^3\mu_{carrier}}{B_0^4\gamma}\frac{1}{(1+\kappa)^2(2+3\kappa)}\left[\frac{3}{14}\frac{16+19\kappa}{2+3\kappa}\left(1-\kappa-2\kappa^2\right)\right.$$
$$\left.+\frac{10+11\kappa}{140}\left(8-\kappa+3\kappa^2\right)\right][L-L(0)] \tag{4.5}$$

where y is the distance of the center of a drop from the channel centerline, y_0 is the initial distance of the drop from the channel centerline, B_0 is the radius of the channel, and γ is the interfacial tension between the phases of liquid. An illustration of these trajectories along with relevant parameters can be found in Figure 4.13. A more extensive look at the results of these trajectories will now be covered.

With the previous expression for trajectories of droplets, the ending distance of droplets from the centerline of the channel can be computed for various geometries and fluids used in this system. This information is then used to ensure that the particular design point chosen will properly sort between empty and cell containing droplets.

First, some geometric parameters are fixed in the analysis, with respect to the geometry of Mask 8. The shear sorting channel is 40 μm long and 15 μm square in cross section. The viscosity of the aqueous phase is that of buffer, which is 1 mPa·s. The interfacial tension used is that of the equilibrium value for a 10p SPAN80 in peanut oil system, 0.8 mN/m which was determined in the previous interfacial tension testing section. Since there is convection and the interface has time to equilibrate before entering the shear channel this is a valid assumption. The viscosity of the oil was also found previously in the viscosity testing section as 74.8 mPa·s. The initial distance of the center of the droplet from the centerline of the shear channel is the ratio of oil coming from the separate oil inlet channels. Since the ratio between oil coming from the top to the bottom is 2:1, the droplets begin (y_0) 5 μm from the center of the channel. Using these parameters and implementing the solution of Equation 4.5 into a Python/SciPy based solver, contour plots of the can be created for a particular design, geometry, and fluidic system. In Figure 4.14 is illustrated these contours for varying oil flow rates and droplet diameters. It is plotted for both the ideal (minimized IFT) peanut oil and fluorinated system.

Looking closely at Figure 4.14, some design information can be determined. First, for the top plot of peanut oil flow rates below 8 μL hr^{-1} show that little sorting will be exhibited between any diameter droplets, and at best 12 μm droplets will end 3 μm from the channel centerline. However, from 15 to 50 μL hr^{-1} the differentiation between empty small droplets and cell containing droplets is distinct and drastic. Empty droplets stay far off the centerline and cell containing droplets are nearly perfectly centered in the channel by the end of the sorting region. This differentiation in channel position of the droplets allows for good and clean sorting once the droplets leave the shear channel. When operating in this regime, the devices work well. An example can be seen in Figure 4.13 c), for peanut oil at 17 μL hr^{-1}. Past 50 μL hr^{-1}, droplets of any diameter all end centered which also negates the purpose of the sorting channel.

Figure 4.14 bottom shows the ideal fluorinated FC70 system. Since sorting is dependent on the deformability of the droplets the vastly increased IFT of this system (4.2 mN m^{-1} *vs* 0.8 mN m^{-1}) decreases the deformability of droplets to the point that high viscous forces must be used to get the same deformations as with the peanut oil system. In this system, optimal size differentiation doesn't occur until around 110 μL hr^{-1}. At this flow rate and a viscosity of 40.3 mPa·s the pressure drop is still attainable (≈83 kPa), but the capillary number can't be further adjusted with flow rate to achieve proper empty droplet sizing. If the capillary number for generation were suitably adjusted (driving up the flow rate to 150 μL hr^{-1} or more) the sorting would then be operating in an unacceptable regime where all droplets are centered and no differentiation achieved. Proper sorting could be achieved in this case by increasing the flow rate while simultaneously decreasing the length of the channel such that proper generation capillary number and sorting occurs, but the decreased channel length could then prove problematic with where droplets are actually generated along the length of the channel.

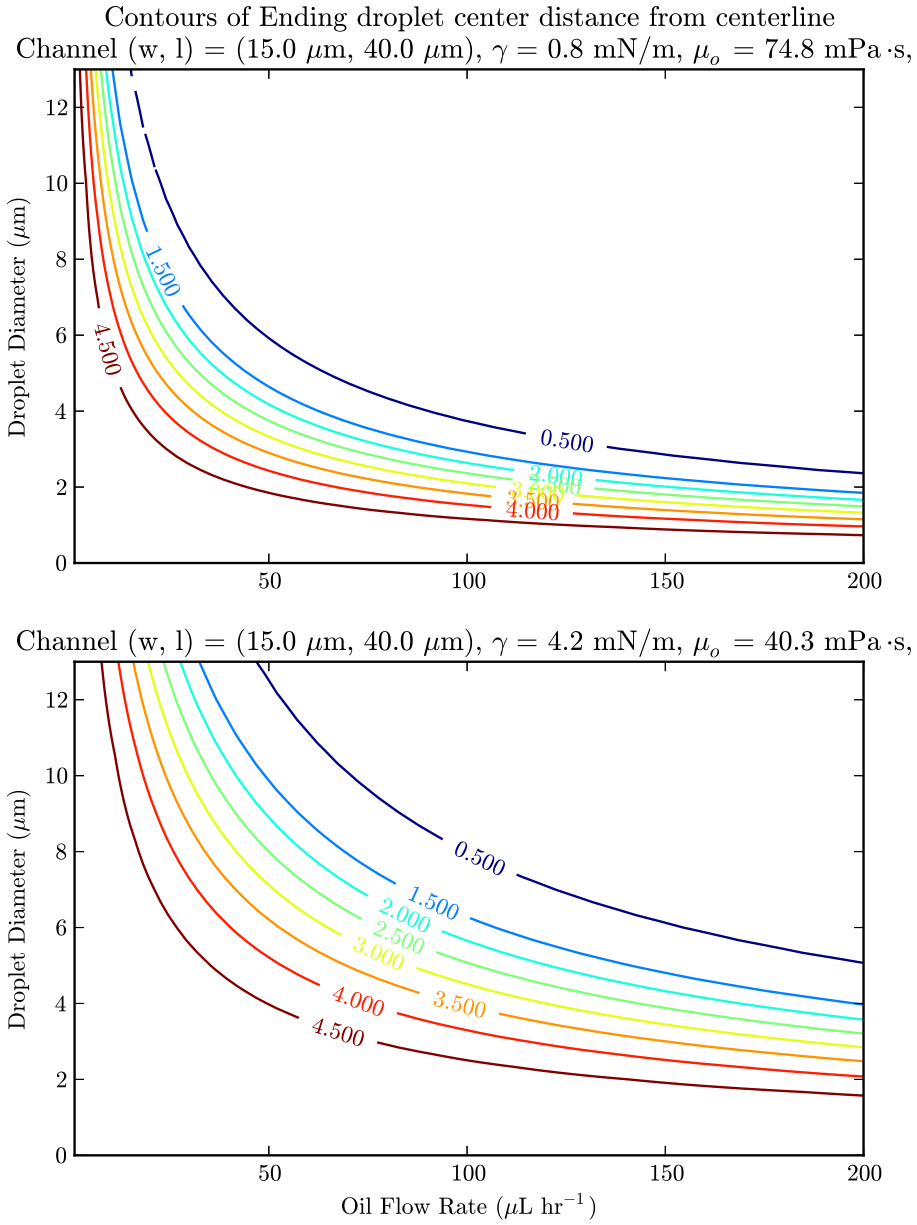

Figure 4.14: Top: Contours of distance from centerline of droplets of varying diameters for optimal peanut oil system. Bottom: Same contours for Fluorinert FC70 system. Note that for high performance sorting (within 1 μm centering of cell-containing 8 μm droplets and sub-micron motion of empty droplets), the fluorinated system must be run at higher flow rates to achieve sorting.

Chapter 5

Experimental Results: Encapsulation, Lysis, and Assay

5.1 Experimental Protocols

5.1.1 Buffer Solutions

For suspension and washing of cells, phosphate buffered saline (PBS) solution is used. This is made from tablets that are composed of the proper salts when added to the correct amount of deionized (DI) water. The buffer has an osmolarity matching the human body (300 mOsmol) and is comprised of sodium chloride, sodium phosphate, potassium chloride, and potassium phosphate to buffer the solution at a constant pH of 7.4.

For pre-swelling the cells prior to encapsulation, a reduced osmolarity buffer is made using 4-(2-hydroxyethyl)-1-piperazineethanesulfonic acid (HEPES) and sucrose. For this application a solution is prepared with DI water, 180 mOsmol HEPES, and 10 mOsmol sucrose. Since this solution is hypotonic, the cells will swell with the added water diffusion. Once swollen, the erythrocytes will possess an additional structural rigidity from increased internal pressure.

When not being used, the buffers are stored in a dark 4°C refrigerator. Buffers are stored for a maximum of two weeks before discarding. If any visible cloudiness is observed in the buffer prior to use it is immediately discarded.

5.1.2 Cell Collection

Cells were collected by medical doctors at the Children's Hospital Oakland Research Institute in 2 mL vacutainer tubes. Donors were healthy adults who had signed informed consent agreements. The collection was performed under an institutional review board-approved protocol.

5.1.3 Cell handling

It is important to note that during pipetting of red blood cells and droplets, the pipetting rate must be kept low to prevent high shear at the pipette tip from lysing cells or coalescing droplets. To prevent cell damage in a 200 μL pipette tip, the plunger is released over the course of 4 s.

5.1.4 Cell Washing

Whole blood is obtained from healthy patient volunteers in 2 mL sterile vacutainer tubes. Blood is stored in a bio-hazard fridge kept at 4°C. When needed, the sample is inverted a few times to break up the settled solid content of the blood. 1 mL is pipetted into a 1.5 mL Eppendorf Safe-Lock centrifugation tube. A second tube is filled with DI water as a counterbalance for the centrifuge.

This sample is then centrifuged at 10K RPM (18,000 g) for 5 seconds with a 10 s ramp up and 30 s ramp down. The sample is removed from the centrifuge with the erythrocytes at the bottom of the tube and supernatant (plasma, platelets, etc) on top of the solids plug. The supernatant is aspirated into a biohazardous bleach collection container. PBS buffer is added to raise the volume to the original 1 mL volume. The container is again inverted to resuspend the erythrocytes in clean PBS buffer. This centrifugation and resuspension in clean PBS is repeated twice more for a total of three centrifugation steps.

On the last centrifugation, the cells are not resuspended in PBS immediately. At this point, the cells can be resuspended in a buffer of choice at any concentration desired. Typical concentrations are between 0.4p and 5p by volume. Lower concentrations are used when the objective of the test is for single events to be recorded in a stretch of high speed video with no cell-cell interaction.

Once the cells are resuspended at their final hematocrit, they are used

within a week of suspension. During this time they are stored in a 4°C fridge when not being used. At the end of the week the cells can start to hemolyse and die, forming erythrocyte ghosts that can confound results.

5.2 Cell Lysis Methods

As previously illustrated, it is essential to be able to lyse single cells at a time to look for analytes inside of the cells. Several methods of single cell lysis have been studied in the past, and each has a specific set of constraints that must be worked around. Depending on what is intended to be measured, it is important to make sure the method of lysis will not interfere with the measurement by either modifying the analyte or even destroying it. An excellent review of several of these methods can be found by Brown and Audet [80]. Those methods and some additional are covered below.

Shear Lysis

The first method of cell lysis is application of shear. In this method of lysis, several confounding factors are at play to confuse the critical shear threshold for hemolysis of red blood cells. In studies conducted in a standard gap viscometer, there is an air interface at the top of the gap in the viscometer, large centrifugal forces, and solid interaction of the cells with the walls of the viscometer. These effects are outlined by Leverett [1] and controlled in this work. For fresh human blood on an exposure time of 2 min, a threshold shear rate of 1500 dynes/cm^2 is found for hemolysis of cells. This study shows that cell-cell interaction is not an issue by varying hematocrit in the viscometer and showing equivalent hemolysis percentage. It also accounts for lysis of cells at the interface of buffer and air by radioactive tracing. A result of this work is that a correlation between shear stress applied and the time of exposure can be found to the threshold stress that causes lysis of the red blood cell. This is illustrated in Figure 5.1.

In microfluidic devices, it will be difficult to achieve shear rates in this regime as shear rate scales with velocity times viscosity. Increasing both or either of these parameters in a small scale system results in a large pressure drop penalty across the device. On top of this, applying a pure shear flow in a microfluidic device is especially troublesome with closed, stationary channels. Additionally, since lysis in the device must be accomplished after encapsulation,

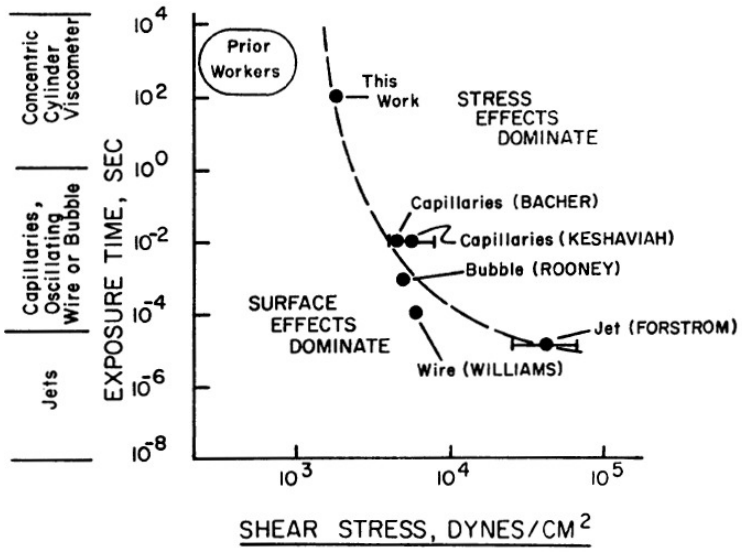

Figure 5.1: Shear damage thresholds and exposure to the shear from Leverett *et al.* [1]. With increasing exposure times, the critical stress level decreases appropriately and can be dominated more by surface and air interaction effects. At high shear stresses the ancilliary effects play less of a role in hemolysis of erythrocytes.

the large shear applied to the droplet would probably break the droplet into smaller sections along with lysing the cell. This is an unacceptable result as data will be lost in the process.

Detergent Lysis

A second option for lysing cells is the use of a detergent. The detergent molecules will diffuse into the cell membrane and by solubilizing lipids the membrane will break apart. In this method, and depending on the detergent, the final analyte can be denatured or modified prior to analysis. Thus it is important to ensure that the detergent used is proper for the application at hand [80]. In microfluidic devices this type of lysis has been performed on a variety of cell lines with different lysis agents, but mainly Triton X and SDS. Some works are outlined here.

C2C12 rat myoblast cells were lysed with 5 mM sodium dodecyl sulfate (SDS) to study the population heterogeneity in tumor cells [81]. Human lymphoblasts were lysed with with 0.1-0.2% SDS in a picoliter contained volume in a chip to prevent diffusion of contents [82]. Finally, canine kidney (MDCK) were lysed with ten different surfactants in three groups, anionic, zwitterionic, and nonionic. The purpos was to determine what effects this chemical lysis had on the resulting assay. Since a protein DNA interaction was to be studied, the effect of these lysis agents on the interaction was compared to a control group. It was found that SDS destroyed the complex, the zwitterionic surfactants modified the surface charge for later osmotic flow, and the nonionic surfactants had the least effect on the level of analyte detected [83; 84].

Optical Lysis

A third option is use of a pulsed laser beam to induce a cavitation site and resultant pressure pulse in the fluid. The beam must be focused through a lens to cause cavitation near to the site of where cells are located. Once cavitation occurs a mechanical shock can break the membranes of cells within the range. By tuning the energy of the pulse, the lysing area of cells can be made greater or finer. With extensive tuning of the lysis parameters, the ability of an expressed green fluorescent protein (GFP) inside the cell to remain intact through the lysis process is shown to be at similar levels to mechanical or electrical lysis [85]. In this work, careful tuning of the origin of the cavitation with respect to the

cell and modulation of laser energy was performed and that this tuning process would be required for any analyte or cell line changes. This would be difficult in the currently developed devices.

Li *et al.* [86] first used laser pulses to lyse single cells for capillary electrophoresis. Their system consisted of Rat basophilic leukemia (RBL) cells cultured on a glass slide. While observing the cells on the slide through a microscope, a laser pulse is applied to lyse the cells. Voltage is immediately applied to a capillary positioned near the lysed cells to collect the cytoplasmic contents before they diffuse too far. This method has the benefit of halting any biochemical reactions from proceeding post-lysis as molecules integral to these processes are rapidly removed from the lysis site by electrophoresis. Many other studies have performed lysis on stationary cultured cells [87; 88]. The main downside to this method is that it is a low throughput process and requires operator intervention to proceed. Additionally, choosing how many cells you would like to lyse from a field of adherent cells requires precise laser location and tuning, and suffers from any misalignments of the optical system.

The previous laser lysis studies have looked only at lysis of stationary, adherent cells on a surface. Though this method is convenient for looking at precise contents of a few observed cells, it does not lend itself to high throughput analysis. Two studies have attempted to perform laser lysis in a flow device for single cell analysis. The first [2] simply flows cells through a PDMS channel and fires a laser pulse as a cell is passing by the target of the laser. BAF-3 cells labeled with a membrane diffusing fluorescent dye were used to track the location of the cells. It was shown that if the cell is well centered in the 50 μm channel the lysis will be successful, however even slight misalignments of the cell only results in cell repositioning. It was also postulated that diffusion of smaller molecules (ATP, Mg+, *etc.*) migrate quickly away from the location of lysis, immediately stopping any biochemical reactions at the point of lysis. Fig. 3 from their work is shown here in Figure 5.2.

Another study looked at lysis of cells inside of closed droplet volumes [26]. In this study, optical tweezers are used to manipulate a cell through a channel to a oil-water interface to when a pressure pulse is used to encapsulate the cell. Thus, droplets containing a single cell are suspended in an oil solution. Once suspended, a laser pulse is applied inside of the droplet and the cell is lysed (verified again with fluorescently labelled cells). Little other study of the phenomena is presented.

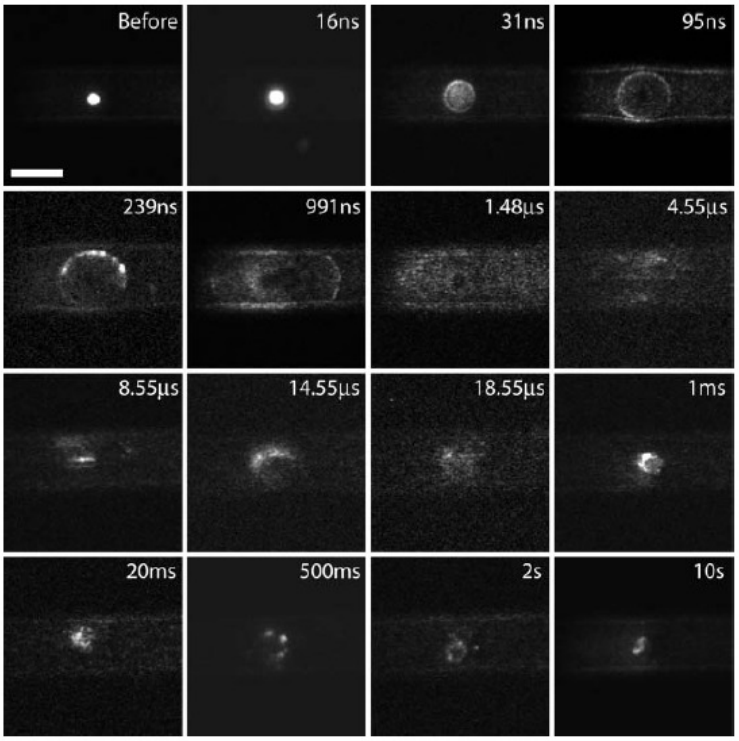

Figure 5.2: Figure of laser-based cell lysis in a channel from Quinto-Su *et al.* [2]. Before lysis the fluorescently labelled sell is seen flowing through a 50 µm PDMS channel. The times are labelled post-laser pulse and the expanding cavitation can be seen. At 239 ns deformation of the channel is seen. Post-lysis, rapid diffusion of small molecules can be seen away from the site of lysis and most of the small diffuse molecules have diffused away after 2 s, leaving little fluorescent background.

Mechanical Lysis

A single study looks at lysing cells via a mechanical means [3]. A filter-type structure of alternating 3 µm channels and 3 µm gaps is fabricated by deep reactive ion etching in silicon. By intentionally overetching each etch step a more nuanced sharp edge, often referred to as scalloping, can be formed on the side of these structures. This sharp edge from scalloping was shown to increase the lysis potential of the device. There are several drawbacks of this method. First the efficiency at releasing proteins from cells, hemoglobin in this case, is shown to be fairly poor. In their best case of high flowrate, only 7% of hemoglobin is released from cells crossing this filter. This is due to the lack of surfactants in the flow to prevent reforming of the membrane and poor lysis to begin with. This method also suffers from a number of setbacks. Cross-contamination between cells can occur if particles remain stuck on the mechanical lysis structure. They attempt to rectify this by running bovine serum albumin (BSA) through the device, but this is imperfect. The large feature size (3 µm) means that the lysis is poor in the device, especially for small deformable red blood cells. This method is also not suitable for rapid throughput or precise lysis of single cells due to its non-specific nature of lysis. The representative method of lysis can be seen in Figure 5.3.

Thermal Lysis

The use of high temperatures, often that of PCR cycling or around 90 °C, can also be used to denature the membrane of a cell. This releases the contents of the cell, and has been used in the past for bulk PCR measurements of the genetic material inside of *E. Coli* cells [89; 90]. A more recent study has extended thermal lysis into regimes that are useful for quantitative single cell analysis. NIH 3T3 Fibroblast cells were selectively lysed after attachment to a microfabricated cantilever [91]. The cantilevers are formed by utilizing highly doped electrodes and a low doped region in the silicon to act as a resistive heater. Since this must be operated under a conductive buffer solution for the cells, electrical insulation is required. This is a problem for many insulating layers such as silicon oxide, but the authors use a ultrananocrystalline diamond coating to provide this layer. With cells affixed and cultured on the cantilever, the device is heated to 93 °C and the cells are lysed. By multiple stains the lysis is observed. This approach is limited to affixed cells, and is not conducive

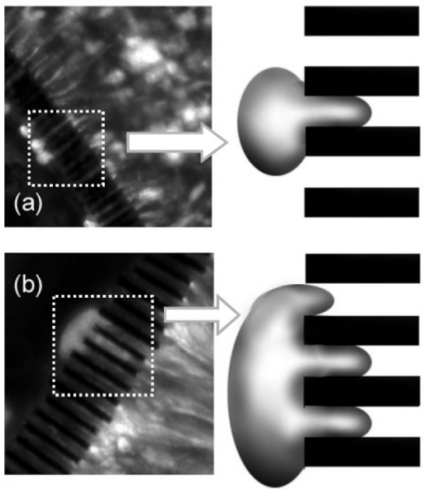

Figure 5.3: Figure of mechanical lysis from Carlo *et al.* [3]. Two ways that erythrocytes go through the mechanical lysing method. The cells are fluorescently stained in the visible images on the left. It is apparent why low quantities of cytosol are released during lysis, knowing that the cell reforms into vesicles after the lysing barbs.

to high throughput analysis. Adding heating to a flow through system would be incredibly complex and require high power heating systems.

Ultrasonic Lysis

Ultrasonic lysis can be used to lyse cells. In one study of large granular lymphocytes [92] it was shown that a single cell could be lysed at the beginning of a capillary electrophoresis tube by exposure to ultrasonics for greater than 50 s. The resultant CE analysis showed widening of the peaks and it was assumed that the heating from the ultrasonic lysis had denatured the protein of interest of the study. They then showed that by permeabilizing the membrane with digitonin prior to injection that the lysis time required could be reduced to 3 s with no resulting denaturization.

Electrical Lysis

Electrical lysis is accomplished by applying more field across the membrane than is used in electroporation. The mechanics of this process are not well

understood, but it is assumed that the most applicable model is proposed by Zimmerman [93]. In this model, it is assumed that when a cell is present in a sufficient electric field, charge accumulates on the inner and outer surface of the cell membrane. This applies a compressive force across the membrane which causes it to thin, and regions of impurities in the membrane causes pores to open. If the transmembrane potential is sufficient, theses pores will expand and cause the membrane to breakup. Several works [94; 95; 96; 97; 24; 98] demonstrate this electrical lysis in a variety of cells. This method is most useful in devices where the cells are stationary and not flowing, as the electrodes must be close together to prevent the applied potential from being too high. If the cells are moving, the time constant for lysis can be higher than the time that the cells reside in the high field region. This is a problem since high voltage at electrodes can cause electrolysis of water and the resulting vapor bubbles can cause problems with fluidic resistance and flow rates in the devices.

Cytolysis

In the case of human erythrocytes, lysis can be performed simply by osmotic pressure. Since erythrocytes do not have a cell wall and have no built in mechanism for regulating water diffusion across their cell membranes it is simple to lyse these cells by exposing them to a hypotonic environment. This method is simple and rapid with a time constant of around 3 s, and the addition of DI water adds no contaminants to the assay system. In the case of the devices presented here, the osmolarity of the solution can be decreased part of this time constant before the cells are encapsulated to allow the cells to pre-swell and eliminate some of that time constant.

5.3 Cell Fouling

Some attention was given to the shortcomings of traditional microfluidic materials earlier, particularly PDMS, and in this section it is shown how non-ideal it really is. Here a clotting test is performed on the same physical test structure but fabricated out of three different materials.

5.3.1 Test Structure

The test structure used for this testing is a single channel of overall dimensions of 4.7 mm by 1.0 mm. It is fabricated to be 10 μm deep in PDMS by using traditional soft lithography off of an SU8 (MicroChem) photoresist master. Using the hot embossing process and parameters detailed in Chapter 2, it was also fabricated in polymethylpentene (PMP) and polyvinylidene fluoride (PVDF). The channel shape is shown in Figure 5.4 and consists of a tortuous geometry intended to cause contact between biological cells and the plastic walls. The cells are also elongated in periodic comb structures which vary in separations from 22 μm at the first comb to 6 μm at the last. The comb structures are meant to activate any shear-based clotting mechanisms of the cells to promote their natural clotting factors. This structure is a worst case microfluidic scenario, and is designed this way to truly elucidate materials problems.

It is hypothesized that due to the lower surface energy and lower porosity of the thermoplastics that the clogging of biological cells will be less of an issue. The contact of biological cells and material will be identical, but problems with adherence of biological molecules on PDMS will cause clogging of the channels.

5.3.2 Cell Preparation and Test Protocol

Samples of human whole blood are washed according to the cell-washing protocol detailed at the beginning of this chapter. After washing, they are resuspended at a 40% hematocrit in PBS buffer. This results in a erythrocyte containing solution at hematocrits near whole blood. It is important to note that most of the clotting cascade is removed by the wash process. Most of the platelets are removed during centrifugation and aspiration due to their lower separation speed as compared with larger erythrocytes. The great majority of other clotting factors in the plasma are also removed and replaced with PBS buffer. This means that the cell solution used will be less able to form clots as compared with human whole blood, but in reality few if any microfluidic devices can work with whole blood. Because most of the clotting factors have been removed, cell adherence to the material used is interactions between erythrocytes and the material being tested.

Once the erythrocyte solution is prepared it is loaded into a single-use plastic 1 mL syringe (Becton-Dickinson). The issues with using plastic syringes

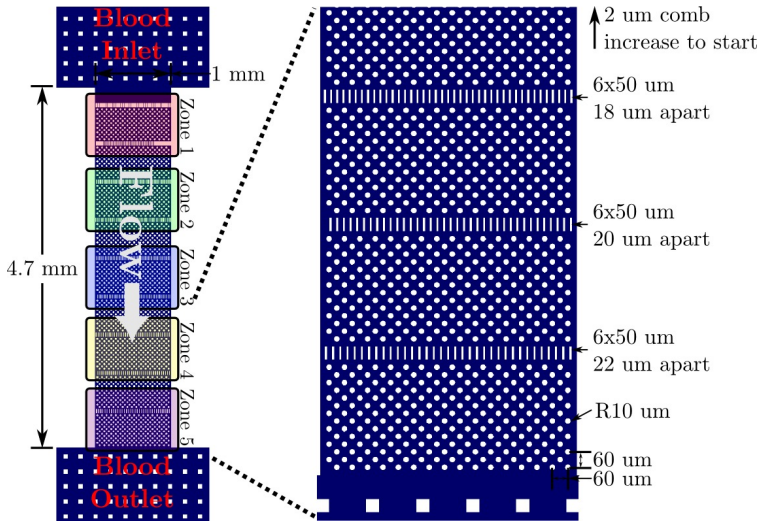

Figure 5.4: Schematic showing the clogging test structure that is used to compare different materials for microfluidic construction. A tortuous path and high flow rate is used to promote contact between cells and the wall materials. Images are taken at each of the five zones listed here for time constants.

in continuous flow syringe pumps are well known and covered in Chapter 2, but do not pose much of a problem here owing to the high flow rates used and low fluidic resistance of the test structure. This syringe is loaded into a syringe pump (New Era, NE-500) controlled via a python script for flow rate. The cells will settle over time in this syringe, but for the timeframe of the testing (less than 10 min) the hematocrit of delivered cells should remain close to intended. For the tests with PDMS, interconnects are 22 gauge needles that are inserted into pre-cored holes in the PDMS. Cracks from the press fit into the PDMS are sealed by using liquid PDMS around the shaft of the needle as its inserted into the PDMS. For the tests with PVDF and PMP, the plastics are sealed in the jig developed for these devices. They are not bonded devices, and are just open faced channels that are sealed with mechanical pressure. As a result, some dust and other particles are visible in sections of the channel. This excess particulate contamination has since been fixed by sealing the channels against a like thermoplastic directly after fabrication.

Once everything is connected, the syringe pump rate is set to 1000 μL hr^{-1}. This flow condition is held until the device fails or further testing flow shows no changes. Every 2 min, pictures of the five zones listed in Figure 5.4 are obtained with visible light.

5.3.3 Clogging Results

A view of the entirety of the PMP channels for all 6 min of testing is shown in Figure 5.5. The test was stopped after this amount of time because although the deposition of cells was enlarging, open channels were staying in the depositions to allow flow through. The flow was not blocked by the deposited cells, and paths were formed between the cells that did deposit on the surface of the PMP. This is expected, as there is little compliance in the channel system so excess pressure cannot deform the plastic. Instead, this excess pressure can force its way through the cellular depositions. It should be noted that the shadows in sections occur from tubing or other occlusions of the light source behind the devices. Most of the occlusions occur only in non-essential areas of the channel. All of these materials are hydrophobic, so some areas between posts are not filled with liquid since the contact angle is greater than 90. The PVDF test material fared similarly to PMP, in that though cellular deposition occurred the devices did not fail as a result of it. A view of the zones in PVDF can be found in Figure 5.7.

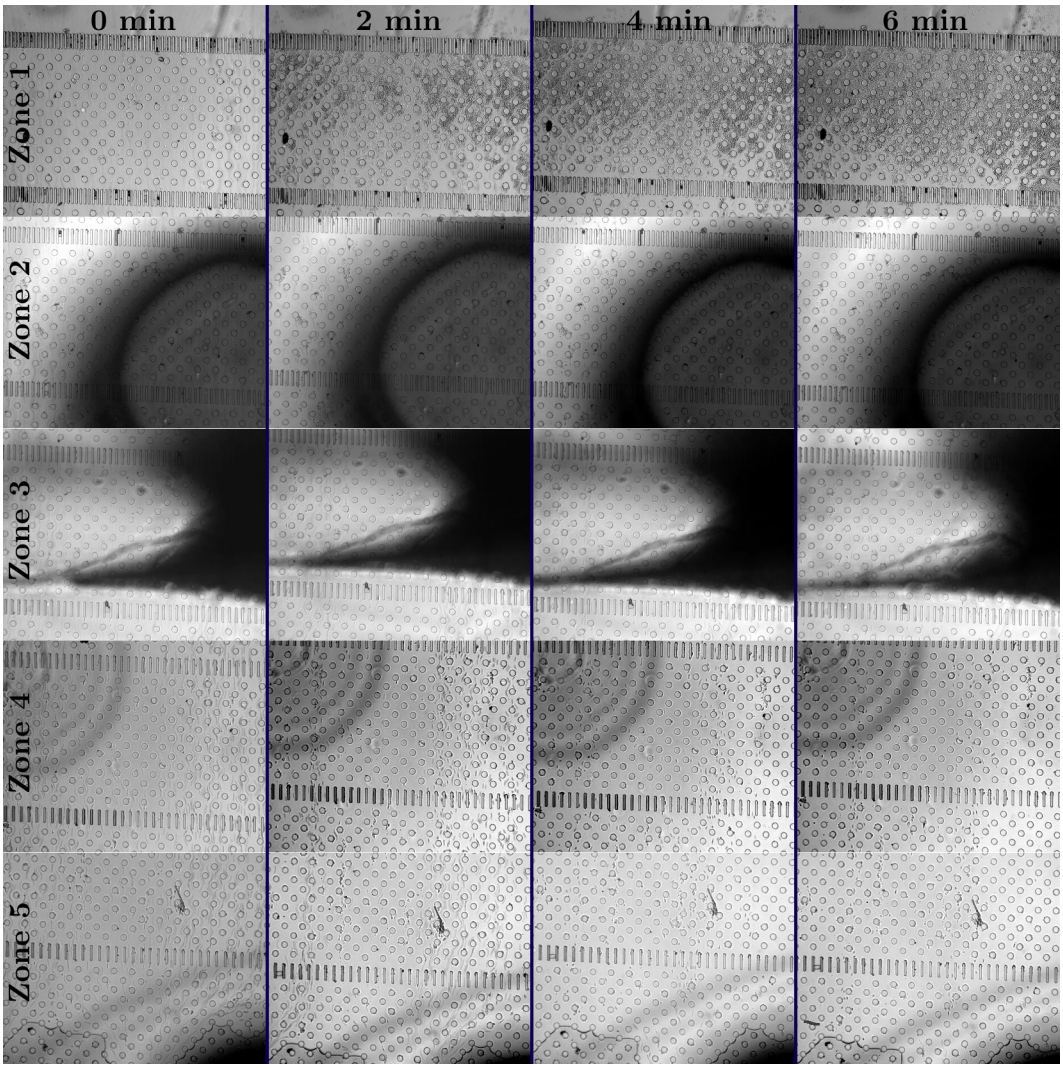

Figure 5.5: A compilation of testing images for the PMP clogging test channel. The columns are by time and the rows are by zone in the channel. The zones locations are shown in Figure 5.4. Cell buildup in PMP occurs only in Zone 1 and the liquid keeps flowing even as clogging occurs.

The PDMS devices faired much worse. Of the four devices tested, three failed before 2 minutes had elapsed. Erythrocytes begin depositing immediately on the PDMS and form an impenetrable mass of biological material that causes the enitre device to delaminate to relieve the building pressure. The PDMS device that lasted longest (4 min) has its channel length shown in Figure 5.6. Between 2 and 4 min little excess deposition of cells can be seen because the flow is becoming blocked. Due to the excess porosity of PDMS the cells can adhere to the locations between the posts that was not a binding area for the PMP devices. This clogging and device failure illustrates an important stumbling point for PDMS microfluidics.

5.3.4 Material Conclusions

This test was initially run after PDMS devices were failing in such large numbers that testing of the devices was not possible. The use of stiffer thermoplastics with lower porosity and fewer of the drawbacks associated with use of PDMS shows true promise in testing microfluidics more effectively. Their simpler fabrication means that less time is wasted during fabrication of devices, and disposal of devices after use with biohazardous materials is not prohibitive by either cost or wasted time. Though deposition occurred on all three materials, only in PDMS did the clots actually form device disrupting blockages. It appears that cells will adhere to both the posts and flat top and bottom surfaces of PDMS, while in the thermoplastics more physical contact is required. Once some cells have adhered to a post in PMP or PVDF, the blockage can build from these adhered cells but doesn't seem to adhere to many other surfaces on the chip.

5.4 Encapsulation and Sorting

5.4.1 Mechanism

The device operation is dependent on getting cell containing droplets of a different size than droplets. This is a difficult task for small and flexible cells such as erythrocytes. Another work that has attempted this [29] has only done so with cancerous large Jurkat cells. As a result their cells are structurally rigid, and resist the fluidic forces during breakup to affect the droplet generation size.

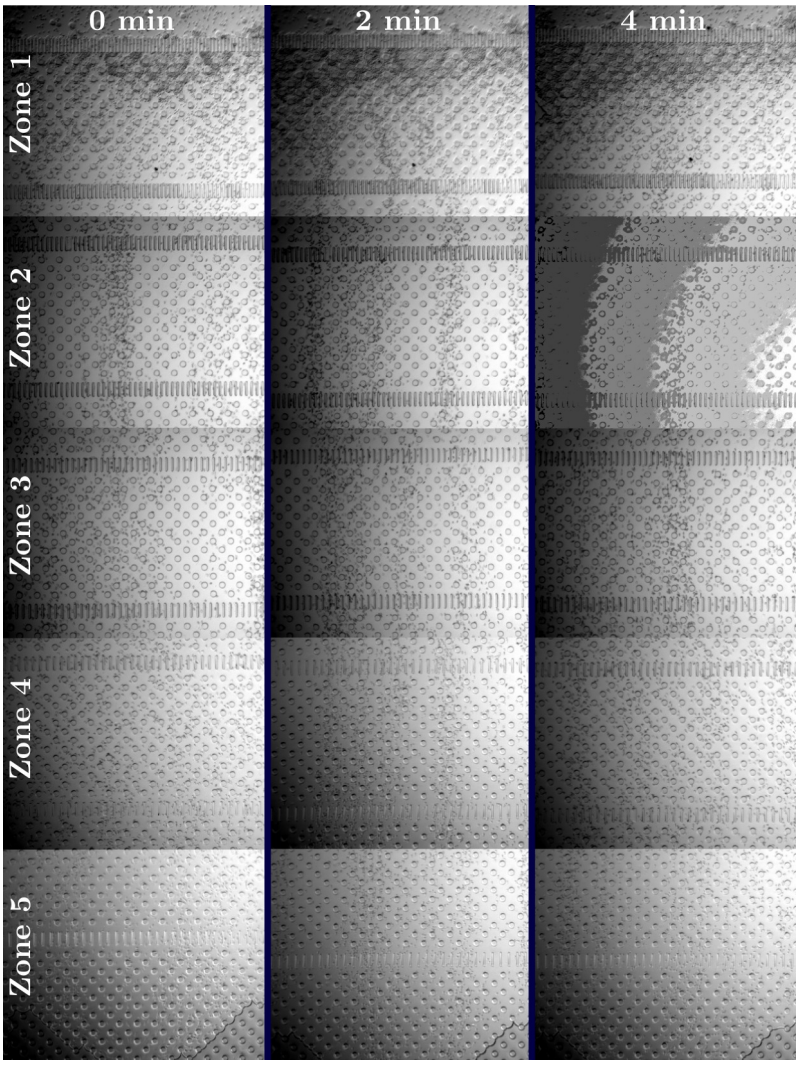

Figure 5.6: A compilation of testing images for the PDMS device that lasted more than 2 min. The last image is prior to the device delaminating to relieve pressure. Cell buildup is limited as flow is nearly fully occluded at 2 min, and PDMS deformation leading to delamination takes up the flow rate set.

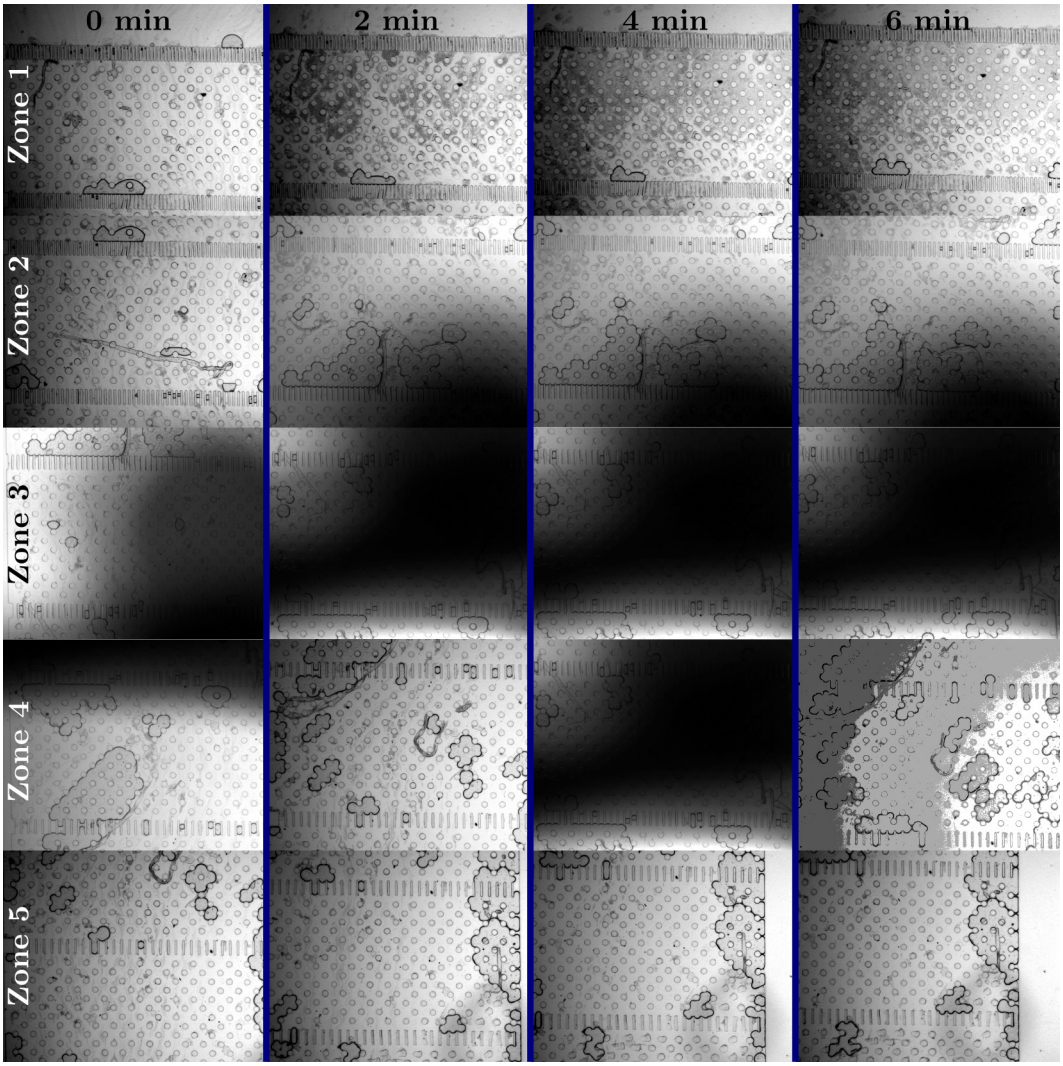

Figure 5.7: Results of testing clotting in the PVDF devices. The results are similar to that of PMP, as the devices never fail even though cells do deposit in certain areas.

This lack of rigidity in the cells means that the interfacial tension, the main force opposing rigidity of cells, must be lowered. Refer to Chapter 3 for a discussion of the typical interfacial tensions in this system.

A calculation of modified pressure in the two phase breakup column can show the maximum interfacial tension we can tolerate in this encapsulation. The change in pressure (ΔP) in a region of the droplet breakup tube can be expressed by the Young-Laplace Equation. In this case, the addition of a cell causes the radius in the lateral (R_1) and the longitudinal direction (R_2) to be equal:

$$\Delta P = \gamma \left(\frac{1}{R_1} + \frac{1}{R_2} \right) = \frac{2\gamma}{R} \tag{5.1}$$

The elastic modulus of a human erythrocyte has been found experimentally [99] to be around 860 Pa. Equating this value and Equation 5.1 while setting the radius of curvature of the same diameter of the cell-containing droplets (R =5 μm), we can solve for the max interfacial tension that can be tolerated without excess cell deformation. This value of maximum interfacial tension is 4.3 mN/m.

A visual of the mechanism creating larger cell containing droplets is given in Figure 5.8. This encapsulation is run at the same conditions that will be outlined further in the next section for peanut oil. While passing through the necking region of the device, it can be seen exerting force on the shape of the interface to deform the shape of breakup. Once this droplet breaks up, its size centers it in the shear channel while the empty droplets stay off center. At the end of the shear channel it exits the positive droplet outlet.

5.4.2 Encapsulation Efficiency and throughput

Of interest in this work is how efficiently the device can encapsulate and separate positive and negative events. The intent is to send cell containing droplets (true positives) in one stream and empty droplets (true negatives) into a different stream. Several issues can prevent this fluidic phenomena from working as intended. If cells get to the necking region of the device in a cluster stuck together there is a good chance the increased shear will break them apart and they will encapsulate as intended. However, there is also a small chance they will become encapsulated in the same droplet. If the flow fluctuates suddenly, the capillary number can be so altered that an empty droplet is large

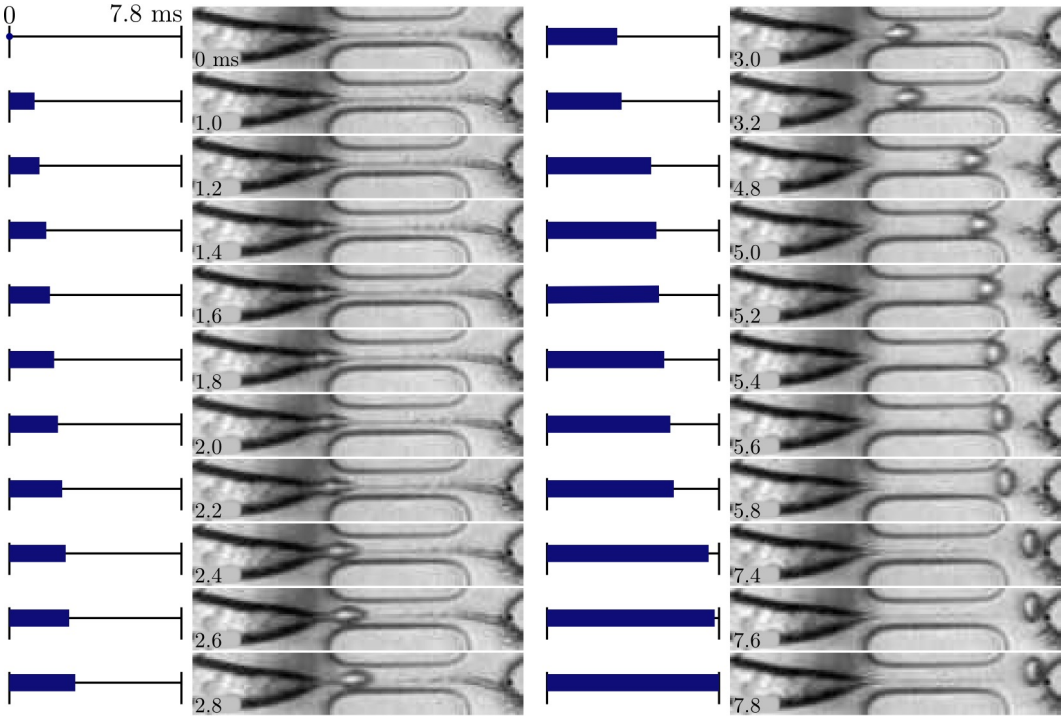

Figure 5.8: 7.8 ms clip showing encapsulation of a erythrocyte in a peanut oil carrier phase. Some frames are omitted and the bars show where in the clip the image is. Initially the droplet neck can be seen expanding as a result of the cell passing through it. Once the droplet breaks off containing this cell the larger size of the droplet centers it in the shear channel. After exiting the shear channel it bumps the slightly offset divider and enters the positive outlet channel.

Table 5.1: Summary of encapsulating and sorting efficiency in different systems and at different flow conditions.

System	*Ca*	Flow Ratio	Positives True	Positives False	Negatives False	2+	f cells/s
Peanut/SPAN80	3.52	52.3	71	3	21	2	71
			73.2%	3.1%	21.6%	2.1%	
FC70/Krytox	0.39	65.4	51	0	0	0	51
			100%	0%	0%	0%	
FC70/Krytox	0.78	81.8	53	14	28	0	53
			55.8%	14.7%	29.5%	0%	

enough to enter the positive outlet stream as a false positive. This is an issue more with syringe pumps, as pressure driven flow gives very constant flow rates. Occasionally and more often in low capillary number systems, a cell will lack the rigidity to form a large droplet around itself during encapsulation, causing the droplet to mistakenly be sent to the waste stream (false negative). This is less problematic than other failed separation as it will do little but lower the throughput of the device. To quantify this efficiency of sorting, a long video of cellular encapsulation must be taken and the results observed. In this context of high speed imaging, long is a relative term and is very limited by the memory of the camera and ranges from 1.1 s to 5.7 s of observation.

For this, devices are placed in the jig for testing. The cells, lysis agent, and oil are loaded into the device and flow rates set. For this test, the pressure was set such that the oil flow was 30 μL hr^{-1} and the cell buffer flow was 0.6 μL hr^{-1}. A summary of encapsulation events can be seen in Table 5.1.

The first system consists of peanut oil and 5p SPAN80 as the continuous phase and washed cells in PBS buffer as the dispersed phase. An image from this encapsulation and sorting can be seen in Figure 5.9 a). In this image, the encapsulation and sorting is very clean. A lot of this is due to reduced interfacial tension, since with this system the IFT is approximately 0.8 mN m^{-1}. This means that when a cell enters the necked region, the resulting cell containing droplet is larger than the empty droplets. Also, any satellite droplets or debris formed as a result of this process is of a very small diameter and thus

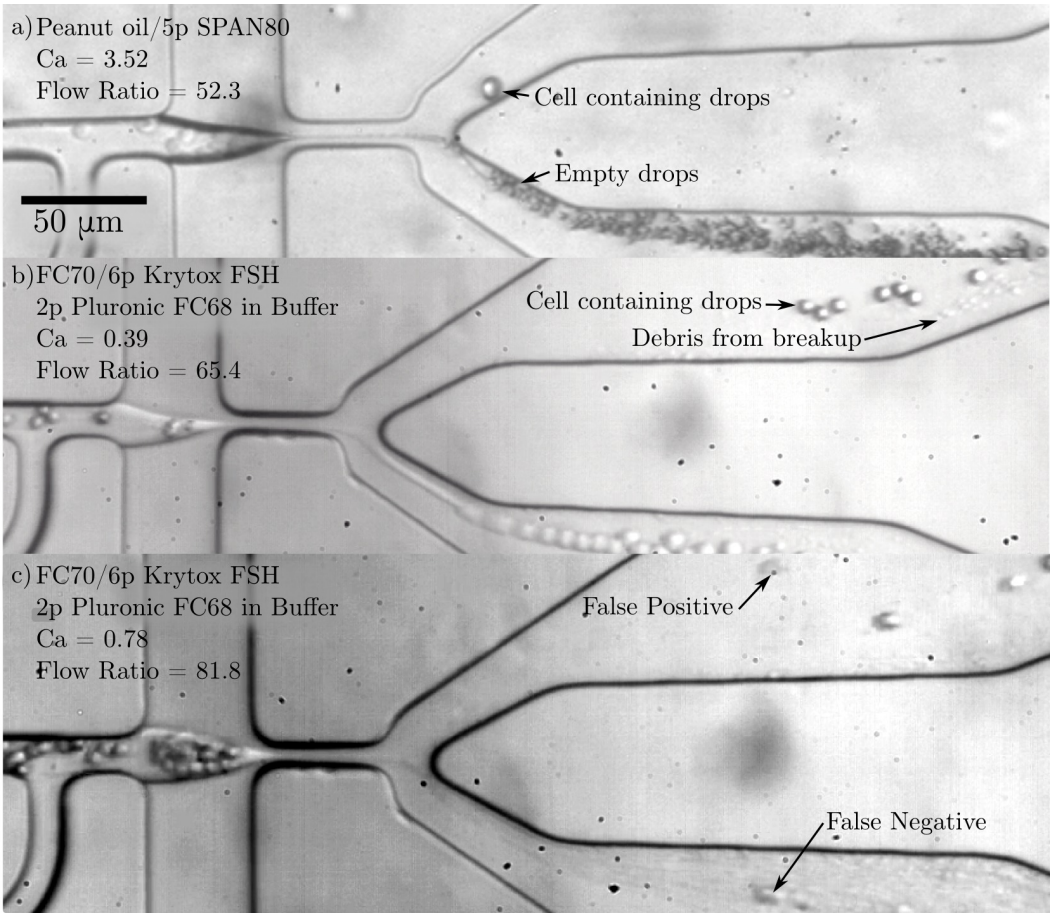

Figure 5.9: Cell-containing droplet sorting at three different flow conditions. a) High capillary number, low interfacial tension encapsulation and sorting in a peanut oil/SPAN80 system. b) Encapsulation and sorting at lower capillary numbers in Fluorinert FC70 and Krytox. Debris can be seen in the positive channel from droplet breakup. c) Doubling the capillary number from b).

is correctly sorted into the waste stream. This effect of the low capillary number is effectively communicated in the capillary number of this breakup, since the reason the capillary number is so high compared to the FC70/Krytox 157 results is that the interfacial tension is so much lower.

The peanut oil statistics for positives and negatives are also fairly promising. The system in this configuration operates at a throughput of around 71 true positive cells per second, but this figure can be easily increased by increasing the hematocrit of the inlet cell solution. A small number of false positives are observed (3.1%), and these generally occur due to disturbances in the flow rate of the dispersed phase. A sudden increase in the dispersed phase flow rate causes a large empty droplet to be formed which will then be sorted into the positive channel. Empty droplets are slightly less damaging to resulting data quality because they will exhibit no fluorescence, and if a second fluorescent tag is used to see if a cell is present it will immediately sort out these empty droplets. What is more damaging to data quality is droplets that contain multiple cells (2.1%). This was occurring because the cells used were at the end of their useful life, and were near to the week mark of their collection and washing. Some of the erythrocytes had lysed and are now just simply ghost membranes which tend to cluster. These ghosts also lack structural rigidity, and most likely contributed for some if not many of the false negatives.

The second system that is tested is FC70 and 6p Krytox 157 FSH by weight. Additionally Pluronic FC68 is in the cell containing buffer at a concentration of 2p by weight. In this system, the interfacial tension is much higher than peanut oil at approximately 3.5 mPa·s. This added interfacial tension is detrimental to the encapsulation and sorting, and can be expressed through the decreased capillary numbers of 0.39 and 0.78 as compared to the peanut oil system at 3.52. These two conditions are seen in Figure 5.9 in b) and c).

In the case of lower capillary number(Figure 5.9 b), the empty droplet stream can be seen to contain droplets nearly equal in size to the cell containing droplets. While this condition is on the razor edge of stability inferred from the dimensional analysis performed and summarized in Figure 4.12 it comes along with a few problems. While cells are not being encapsulated, there is no problem of debris from satellite breakup present. However, when a cell breaks the stream a satellite droplet is formed of sufficient size to enter the positive stream of droplets. These debris particles are not summarized in Table 5.1 as false positives because during a flow cytometry run of the droplets, they would easily be detected due to the drastic size difference on the forward scatter sensor

of the laser.

For the higher capillary number (Figure 5.9 c) the empty droplets are much smaller, but the sorting and debris problems are more visible than at lower capillary number. Even though the droplets are now the correct size, the increased interfacial tension means that the migration velocity of the drops is much lower than for the peanut oil case.

5.4.3 Encapsulation Conclusion

This testing illustrates what is important for reliable and clean encapsulation. The interfacial tension has to be near 1 mN m^{-1} and the capillary number in the range as set by the device specifications (Table 2.1) to get good separation of sizes of droplets once formed. The fluorinated system, while offering many benefits from a materials and autofluorescence standpoint would require additional work on surfactants to make it a promising candidate with sufficiently low interfacial tension.

5.5 Lysis

Many types of lysis are outlined at the beginning of this chapter, but most require complicated external equipment, small on-chip features, or large electrical fields. In the interest of keeping the system compact and simple, a logical approach for cell lysis is cytolysis. In this approach, the osmolarity of the buffer is dropped just prior to encapsulation to cause the cells to swell and burst after encapsulation. This approach is outlined in Figure 5.10. Lysis agent is added to the dispersed phase directly before the cross to cause cell lysis after droplet breakup. This approach can be extended other forms of chemical lysis if the cells to be analyzed are not red blood cells.

The downside to this method, as hinted at in Figure 5.10, is that there is a time constant involved with cytolysis. For DI water and erythrocytes, this time constant for lysis is a few seconds. Two minor modifications of the design of the devices can be implemented to negate any temporal effects of having such a long time between lysis agent addition and actual cell lysis. First, the outlet channels are widened post-encapsulation after the surfactant has had time to fully saturate the surface of the droplets. If this widening happens before the interfaces of the droplets are fully saturated with surfactants droplets will

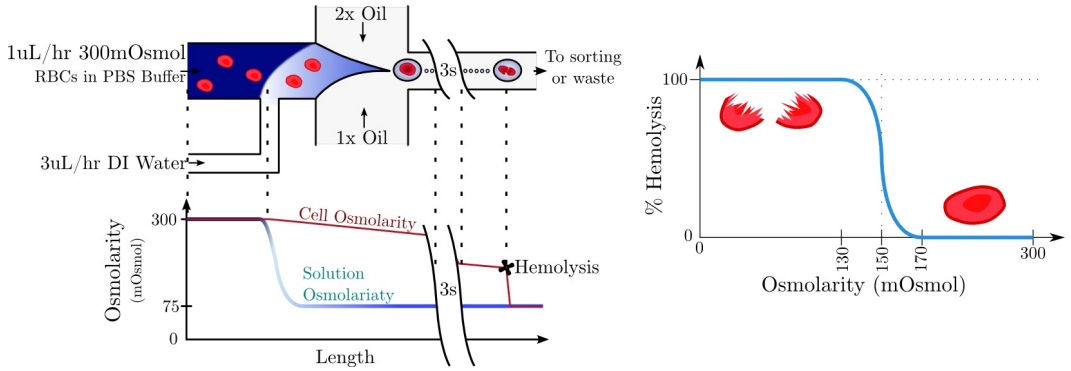

Figure 5.10: Method of lysis in the devices. At left a schematic view of how the lysis is accomplished. The osmolarity (plotted beneath the schematic) is lowered by addition of DI water prior to encapsulation of cells. Once encapsulated, the cell begins swelling in the hypotonic solution that surrounds it. After some time the cell is swollen to the point that it bursts and releases it's contents into the droplet. At right, an equilibrium plot showing approximate percentage of lysed cells at different osmolarities.

coalesce with one another. As designed, an encapsulated droplet will remain in the outlet channel for 4.1 s with this widening feature while the pressure drop remains manageable from lower velocities in this large channel.

Second, the location where the buffer osmolarity is changed prior to encapsulation can be tailored to the specific lysis agent used in the system. Knowing the design point of velocity of the dispersed phase means that simple calculation of distance gives a time that the osmolarity will be dropped before encapsulation. Because the flow rate of the cell solution is very low (1 μm hr^{-1}) compared with the post-encapsulation velocity of droplets even a slight tailoring of this distance allows for an addition to the time cells are exposed to hypotonic solution. Three distances prior to encapsulation are designed into devices, and they are shown in Figure 5.11 a. Comparing the residence time of cells in this pre-encapsulation section to the post-encapsulation section, it is evident that time constant is less of an issue than would otherwise be expected. Just 775 μm of pre-encapsulation channel length equates to 3 s, while 6900 μm of post-encapsulation channel length is only 4.1 s. Since the inlet channel of the dispersed channel is approximately 24 mm long, any lysis buffer can be used with a time constant to lysis up to 90 s successfully in this type of chip

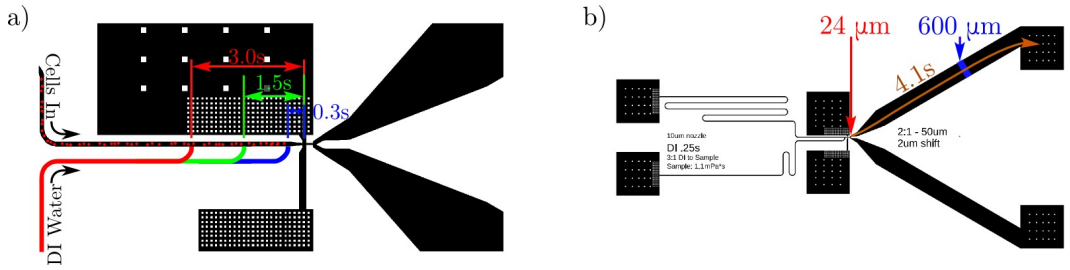

Figure 5.11: Two methods of negating time constant of cytolysis. a) Lower buffer osmolarity 0.3, 1.5, or 3.0 s before encapsulation. b) Decrease fluid velocity by geometric enlargement after surfactant saturation. Residence time design 4.1 s.

layout.

High speed imaging is used to show that cell lysis is indeed occuring in these devices. A video is made by panning the microscope stage holding the entire testing fixture to follow droplets after they have been encapsulated. Single cell-containing droplets can be tracked in this manner, and the resulting time of lysis can be seen. The video is taken at a rate of 300 FPS to allow for longer videos to be taken of these cells without running out of memory in the high speed camera. The time of each frame can be determined by the time that the droplet has formed with a cell inside and the corresponding frame number of the image. It should be noted that many other cell containing droplets are present in this video, and these offer just a subset of that group. In this video, the carrier fluid is Fluorinert FC70 with 3p Krytox 157 FSH. The buffer fluid is PBS with 2p Pluronic F68, and cells are suspended at 5p hematocrit. The results can be seen in Figure 5.12. This figure tracks four cells with time to lysis marked from their generation. The times observed correspond with the time scales that have been reported previously for cytolysis. The time for lysis is approximately 2 s after cell encapsulation in these devices.

This is the last component of these devices to function properly, and completes the design intent. Once the cells are lysed in the exit channels of the devices, fluorescent assays can be performed in the device or with a flow cytometer. Since the droplets are stable against re-coalescence, they can also be removed from the device and transported to other assays.

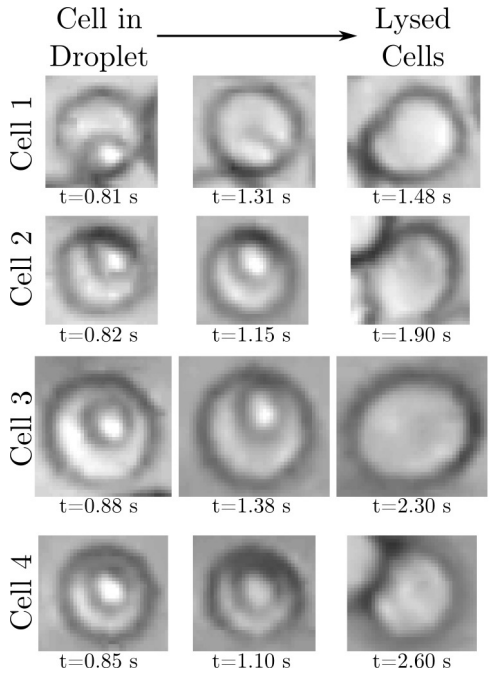

Figure 5.12: Images of four different droplets with cells pre- and post-lysis. The cells were tracked by panning the microscope stage while recording at 300 fps to watch the same droplets over a time period that is longer than the residence time of a droplet in the microscope field of view. Each droplet has three frames captured.

Chapter 6

Conclusion

The main contributions of this work are threefold: the fabrication of microfluidics was improved, effects of surfactants and their affect on fluidic parameters were categorized, and single cells were shown to be lysed inside of droplets for the first time in a high-throughput, passive sorting system. The work established a new tool for cellular analysis. The specific achievements will be outlined below.

6.0.1 Device Function

The devices were able to perform the encapsulation and sorting of human erythrocytes, with high yields (55 to 100% true positives, depending on fluidic system) at rates near 70 cells s^{-1}. The system was optimized through detailed analysis of droplet generation with cells present, passive hydrodynamic sorting, and biological interaction on chip. This throughput can be increased by increasing the hematocrit of the cell containing buffer in the system. If even higher throughputs are desired, parallelizing this system on a chip is trivial, and in a similar on-chip footprint many sets of this device can operate together. Since no external hardware is required for device operation, it is possible to make several copies of the device on a single chip. While not as fast as current commercial tools for flow cytometry, this throughput is approaching the throughput required to get statistically meaningful results from populations of cells.

The importance of single cell assay is emphasized as the path forward for future biological understanding. There are many phenomena from gene expression to disease progression where complete understanding can only be accom-

plished with an understanding of how stochasticity presents itself in individual cells in a population. Flow cytometry, while powerful, is limited in its ability to provide this information in a rapid and efficient manner. By providing physical access to the contents of cells, the technique is easily extensible to non-traditional assays on intracellular components of cells.s

6.0.2 Device fabrication

In this work, several aspects of microfluidic design are improved upon and implemented. It was shown that a plastic device can successfully extend flow cytometry to biological realms that were previously beyond assay. It should be noted that this microfluidic design places strict constraints on the fabrication and operation of these devices. Operating with small channels and high flow rates of very viscous carrier fluids results in high pressures and problems that normally are not issues in microfluidics. Much of this work was designing microfluidics to be more robust and easily manufacturable. This robustness is important going forward when control of microfluidic devices must attain the repeatability and precision that will enable the microfluidics field to successfully transition from academic curiosities to true functioning diagnostic devices.

The fabrication and testing of plastic devices is presented as a viable and preferable alternative to the traditional PDMS soft lithography used in research-scale testing. Realized benefits are numerous and include the following. Thermoplastic devices can be made in larger quantities with no additional time requirements which enables used devices to be discarded with other biohazardous waste after testing. The pressure handling ability and prevention of biofouling is much improved over PDMS and was demonstrated experimentally on the devices designed in this thesis.

Clogging and biological fouling of devices was addressed with an on-chip filter. These filters were located on all of the fluidic inlets, and the addition of the filter posts successfully prevented clogging that was previously observed. The chips themselves were also used for flow metering of the carrier and dispersed phases by tailoring the resistances of the channel network produced. This is a solid departure from conventional microfluidic design where flow rates are set at the syringe pumping location, and enable a much more constant pressure source to meter the flow in the chips. In this work the characteristic channel dimensions are much smaller (15 μm) and the capillary number of operation much higher (around 4) than similar works, and metering a sensitive flow with

syringe pumps is not an option. Initial designs utilized syringe pumps until it was realized that instabilities in the syringe pumps were causing fluctuations of such magnitude that it was interfering with droplet generation.

6.0.3 Fluidics Classification

To operate in a fairly sensitive droplet generation mode, the fluidics of the system must be characterized and understood. To this extent dimensional analysis was used to find an operating regime where the device will operate as intended based on parameters of the fluidic system. To characterize these parameters experimentally, tests were developed for viscosity using a capillary of known dimension and interfacial tension using a side mounted camera and a syringe. Two fluidic systems were characterized, both a fluorinated system (FC70 with Krytox 157 FSH and Pluronic FC68 as surfactants) and a fatty acid system (peanut oil with SPAN 80 and FC68). Despite being more appropriate for this application in other metrics such as surfactant auto-fluorescence, the fluorinated system could not achieve an interfacial tension low enough to be useful for cell encapsulation.

The devices that were fabricated were tested for biological fouling, and it was found that PDMS was not only unsuitable for this high flow-rate application but that it also would delaminate after a short amount of time. The thermoplastic devices could operate for indefinite time intervals, even when handling high hematocrit solutions of human blood.

6.0.4 Future Direction

The next logical step for this work is to implement the chip onto an insert used in a microfluidic flow cytometer. It has been demonstrated as a simple and low cost method to encapsulate, sort, and lyse cells in droplets, and a flow cytometer has all the necessary optical hardware to analyze the fluorescent results of each single cell as it passes through the detector. In this way, biological researchers will be given a tool to further analyze stochasticity of cells in a larger population.

Chapter 7

Appendix

7.1 Channel Resistance Code

7.1.1 Class TBChannel.py

```
'''
Created on Jul 26, 2011

@author: tim brackbill
'''

from scipy import *

class TBChannel:
    def __init__(self, mu, rho, depth):
        self._mu = mu
        self._rho = rho
        self._depth = depth

    def channelPD(self, width, length, q):
        bwidth = width
        bdepth = self._depth
        blength = length
        rho = self._rho
        mu = self._mu
```

```
# Tim Brackbill 2009 - from MATLAB
# Calculate parameters of given channel width and height
#function [bdP bdPpsi dP] =
#    single_channel(bwidth, blength, q, bdepth)
# channel area - meters squared
barea = bwidth * bdepth;
#channel perimeter meters
bperim = 2*bwidth + 2*bdepth;
#channel hydraulic diameter
bDh = 4*barea/bperim;
#volume flow in uL/hr with conversion to m**3/s
bQ = q * 2.777777e-13;
#average channel velocity
bv = bQ / barea;
#reynolds number
bRe = rho * bv * bDh / mu;
# Aspect ratio must always be less than one
if bdepth < bwidth:
    #aspect ratio
    balpha = bdepth / bwidth;
else:
    balpha = bwidth / bdepth;
# fanning (1/4 darcy)friction factor *re
bfRe = 24*(1 - 1.3553*balpha + 1.9467*balpha**2 -
           1.7012*balpha**3 + 0.9564*balpha**4 -
           0.2537*balpha**5);
# Friction factor For Rectanular...problems with too low RE
bf = bfRe / bRe;
 #Pressure Drop
bdP = 2 * bf * rho * bv**2 * blength / bDh;
#Pressure drop psi
bdPpsi = bdP*0.000145037738;
#inches - radius of syringe
bsyringerad = .1;
#force the syringe pump must generate
bsyringeforce = bdPpsi * (bsyringerad**2*pi);
```

```
        #dont neglect entrance region
        Kinf = (0.6796 + 1.2197*balpha + 3.3089*balpha**2 -
                9.5921*balpha**3 + 8.9089*balpha**4 -
                2.9959*balpha**5);
        dP = (2 * bf * blength *bRe * mu *
              bv) / bDh**2 + (Kinf * rho * bv**2) / 2;
        dPpsi = dP*0.000145037738;

        if __name__ == '__main__':
            print('dP is '+str(dP)+' Pa')

        return dP, dPpsi, bv

if __name__ == '__main__': #test the class
    width = 100e-6
    depth = 100e-6
    length = 1000e-6
    mu = .001
    rho = 998
    q = 70
    tbc = TBChannel( mu, rho, depth)
    tbc.channelPD(width, length, q)
    tbc.channelPD(width, 2000e-6, q)
```

7.1.2 Script ChnNetwork.py

```
'''
Created on Oct 21, 2011

@author: tim
'''


from scipy import *
from TBChannel import *
```

```
#Debug options
SampleDebug = False
DIDebug = SampleDebug
OilDebug = SampleDebug

#Design parameters
QSample = .1
QDI = .3
QOilTop = 100.
QOilBot = QOilTop / 3.
 #uL/hr, total flow rate through exit
Qoutlet = QSample + QOilTop + QOilBot + QDI
# psi difference between reg 1 and reg 2 for the inlets
reg2diff = 1.395
# convert to Pa
reg2diff = reg2diff * 6894

#Dimensions
#Depth of channels in device
depth = 15e-6
lOilTop = 100e-6
wOilTop = 50e-6
# Width of sample channel
wSample = 30e-6
#lDI = 25e-3
# Width of di channel
wDI = 30e-6
#width of one side of outlet channel
outWidth = 500e-6
 #length of one side of outlet channel
outLength = 6e-3
 #width of constriction
constWidth = 15e-6
 #length of constriction
constLength = 50e-6

#Constants
```

```
gamma = 0.003 #N/m assumed
Atm = 101135 #Pa, atm pressure
oilRho = 1940 #SI
sampleRho = 998 #SI
oilMu = 0.040 #Pa*s
sampleMu = .0011 #Pa*s
DIRho = 998
DIMu = 0.001

#list of pressure of sections of device
Pressures = list()
#list of names of the segments
Sections = list()

#Setup channel query
topOil = TBChannel(oilMu, oilRho, depth)
botOil = TBChannel(oilMu, oilRho, depth)
sample = TBChannel(sampleMu, sampleRho, depth)
const = TBChannel(oilMu, oilRho, depth)
separator = TBChannel(oilMu, oilRho, depth)
DI = TBChannel(DIMu, DIRho, depth)

#Set outlet pressure drop based on flow rate desired
press = separator.channelPD(outWidth, outLength, Qoutlet/2)
Pressures.append(press[1])
outVel = press[2]
Sections.append('Outlet (psi)')

#Get constriction
press = const.channelPD(constWidth, constLength, Qoutlet)
Pressures.append(press[1])
 #this is constriction velocity for capillary num
avgVelCa = press[2]
Sections.append('Constriction (psi)')

#Oil Top
press = topOil.channelPD(wOilTop, lOilTop, QOilTop)
```

```
targetPress = press[0]
Pressures.append(press[1])
Sections.append('Oil Top (psi)')

#Find Oil Bottom Length iterative
Stopper = 1
Mult = -1e-8
Tol = 1e-6
itWid = lOilTop
while Stopper == 1:
    press = botOil.channelPD(wOilTop, itWid, QOilBot)
    curPress = press[0]
    diff = curPress - targetPress
    if abs(diff) >= Tol:
        itWid = itWid + Mult*diff
    else:
        Stopper = 0
    if OilDebug:
        print('Sample Debug: itwid %.2f' % (itWid*10**6))
Pressures.append(press[1])
Sections.append('Oil Bottom (psi)')
BotOilWid = itWid
print('Bottom Channel must be %.2f um long for flow ratio'
      % (BotOilWid*10**6))

#Find Sample Width iterative
Stopper = 1
Mult = -1e-6
Tol = 1e-3
itWid = 30e-3
targetPressSubFix = targetPress - reg2diff
while Stopper == 1:
    press = sample.channelPD(wSample, itWid, QSample)
    curPress = press[0]
    diff = curPress - targetPressSubFix
    if abs(diff) >= Tol:
        itWid = itWid + Mult*diff
```

```
    else:
        Stopper = 0
    if SampleDebug:
        print('Sample Debug: itwid %.2f' % (itWid*10**6))
        print('targetPress is %.2f and reg2diff is %.2f'
              % (targetPress, reg2diff))
Pressures.append(press[1])
Sections.append('Sample (psi)')
SampleLen = itWid

print('\nSample avg Vel is %.2f um/s'
      % (1000000*press[2]))
print('Sample and DI addition velocity is %.2f um/s'
      % (1000000*(press[2] * (QDI + QSample) / QSample)))

print('\nSample length must be %.2f mm for correct sample flow '
      % (SampleLen*10**3))


#Find DI Width iterative
Stopper = 1
Mult = -1e-6
Tol = 1e-3
itWid = 20e-3
targetPressSubDI = targetPress - reg2diff
while Stopper == 1:
    press = DI.channelPD(wDI, itWid, QDI)
    curPress = press[0]
    diff = curPress - targetPressSubDI
    if abs(diff) >= Tol:
        itWid = itWid + Mult*diff
    else:
        Stopper = 0
    if DIDebug:
        print('DI Debug: itWid %.2f' % (itWid*10**6))
Pressures.append(press[1])
Sections.append('DI (psi)')
```

```
SampleLen = itWid
print('DI length must be %.2f mm for correct sample flow'
      % (SampleLen*10**3))
print('Reg Difference is %.2f psi' % (reg2diff/6894.))

#Print pressures
devSumPress = 0
print('\nPressures(psi) and their sections')
for i, section in enumerate(Sections):
    print('%s - %.2f' % (section, Pressures[i]))
    if i <= 2:
        devSumPress += Pressures[i]

print('\nTotal pressure drop of device is %.2f psi'
      % devSumPress)
print('Flow Ratio/Cap: %.1f / %.2f '
      % (((QOilTop+QOilBot)/(QSample+QDI)) ,
          ((oilMu * avgVelCa)/gamma)) )
print('Residence time in outlet is %.2f s'
       % (outLength/outVel))
```

Bibliography

[1] L. B. Leverett, J. D. Hellums, C. P. Alfrey, and E. C. Lynch, "Red blood cell damage by shear stress," *Biophysical Journal*, vol. 12, pp. 257–273, Mar. 1972. PMID: 50161125016112 PMCID: 1484094.

[2] P. A. Quinto-Su, H.-H. Lai, H. H. Yoon, C. E. Sims, N. L. Allbritton, and V. Venugopalan, "Examination of laser microbeam cell lysis in a PDMS microfluidic channel using time-resolved imaging," *Lab on a Chip*, vol. 8, pp. 408–414, Mar. 2008. PMID: 18305858.

[3] D. D. Carlo, K.-H. Jeong, and L. P. Lee, "Reagentless mechanical cell lysis by nanoscale barbs in microchannels for sample preparation," *Lab Chip*, vol. 3, pp. 287–291, Aug. 2003.

[4] M. Kaern, T. C. Elston, W. J. Blake, and J. J. Collins, "Stochasticity in gene expression: from theories to phenotypes," *Nat Rev Genet*, vol. 6, pp. 451–464, June 2005.

[5] H. B. Fraser, A. E. Hirsh, G. Giaever, J. Kumm, and M. B. Eisen, "Noise minimization in eukaryotic gene expression," *PLoS Biol*, vol. 2, p. e137, Apr. 2004.

[6] B. Ian R, "Stress and the single cell: Intrapopulation diversity is a mechanism to ensure survival upon exposure to stress," *International Journal of Food Microbiology*, vol. 78, pp. 19–30, Sept. 2002.

[7] M. Thattai and A. van Oudenaarden, "Stochastic gene expression in fluctuating environments," *Genetics*, vol. 167, pp. 523–530, May 2004. PMID: 15166174.

[8] N. Q. Balaban, J. Merrin, R. Chait, L. Kowalik, and S. Leibler, "Bacterial persistence as a phenotypic switch," *Science*, vol. 305, no. 5690, pp. 1622 –1625, 2004.

[9] K. Lewis, "Programmed death in bacteria," *Microbiology and Molecular Biology Reviews*, vol. 64, no. 3, pp. 503 –514, 2000.

[10] P. Simpson, "Notch signalling in development: on equivalence groups and asymmetric developmental potential," *Current Opinion in Genetics & Development*, vol. 7, pp. 537–542, Aug. 1997. PMID: 9309187.

[11] T. Hoang, "The origin of hematopoietic cell type diversity," *Oncogene*, vol. 23, no. 43, pp. 7188–7198, 2004.

[12] T. Enver, C. Heyworth, and T. Dexter, "Do stem cells play dice?," *Blood*, vol. 92, pp. 348 –351, July 1998.

[13] D. A. Hume, "Probability in transcriptional regulation and its implications for leukocyte differentiation and inducible gene expression," *Blood*, vol. 96, pp. 2323 –2328, Oct. 2000.

[14] S. V. Avery, "Microbial cell individuality and the underlying sources of heterogeneity," *Nat Rev Micro*, vol. 4, no. 8, pp. 577–587, 2006.

[15] I. R. Henderson, P. Owen, and J. P. Nataro, "Molecular switches–the ON and OFF of bacterial phase variation," *Molecular Microbiology*, vol. 33, pp. 919–932, Sept. 1999. PMID: 10476027.

[16] A. Hernday, B. Braaten, and D. Low, "The intricate workings of a bacterial epigenetic switch," *Advances in Experimental Medicine and Biology*, vol. 547, pp. 83–89, 2004. PMID: 15230094.

[17] P. Etienne, "Regulation of antigen gene expression in trypanosoma brucei," *Trends in Parasitology*, vol. 21, pp. 517–520, Nov. 2005.

[18] D. Horn and J. D. Barry, "The central roles of telomeres and subtelomeres in antigenic variation in african trypanosomes," *Chromosome Research*, vol. 13, no. 5, pp. 525–533, 2005. PMID: 16132817.

[19] T. S. Voss, J. Healer, A. J. Marty, M. F. Duffy, J. K. Thompson, J. G. Beeson, J. C. Reeder, B. S. Crabb, and A. F. Cowman, "A var gene promoter controls allelic exclusion of virulence genes in plasmodium falciparum malaria," *Nature*, vol. 439, pp. 1004–1008, Feb. 2006.

[20] S. A. Ralph and A. Scherf, "The epigenetic control of antigenic variation in plasmodium falciparum," *Current Opinion in Microbiology*, vol. 8, pp. 434–440, Aug. 2005.

[21] M. J. Fulwyler, "Electronic separation of biological cells by volume," *Science*, vol. 150, pp. 910 –911, Nov. 1965.

[22] W. M. Dittrich and W. H. Gohde, "Flow-through chamber for photometers to measure and count particles in a dispersion medium," Sept. 1973.

[23] A. Schwartz, A. K. Gaigalas, L. Wang, G. E. Marti, R. F. Vogt, and E. Fernandez-Repollet, "Formalization of the MESF unit of fluorescence intensity," *Cytometry. Part B, Clinical Cytometry*, vol. 57, pp. 1–6, Jan. 2004. PMID: 14696057.

[24] M. A. McClain, C. T. Culbertson, S. C. Jacobson, N. L. Allbritton, C. E. Sims, and J. M. Ramsey, "Microfluidic devices for the high-throughput chemical analysis of cells," *Anal. Chem.*, vol. 75, no. 21, pp. 5646–5655, 2003.

[25] H. Wu, A. Wheeler, and R. N. Zare, "Chemical cytometry on a picoliter-scale integrated microfluidic chip," *Proceedings of the National Academy of Sciences of the United States of America*, vol. 101, no. 35, pp. 12809 –12813, 2004.

[26] M. He, J. S. Edgar, G. D. M. Jeffries, R. M. Lorenz, J. P. Shelby, and D. T. Chiu, "Selective encapsulation of single cells and subcellular organelles into picoliter- and femtoliter-volume droplets," *Anal. Chem.*, vol. 77, no. 6, pp. 1539–1544, 2005.

[27] C.-H. Choi, J.-H. Jung, Y. Rhee, D.-P. Kim, S.-E. Shim, and C.-S. Lee, "Generation of monodisperse alginate microbeads and in situ encapsulation of cell in microfluidic device," *Biomedical Microdevices*, vol. 9, pp. 855–862, Dec. 2007.

[28] H. Shintaku, T. Kuwabara, S. Kawano, T. Suzuki, I. Kanno, and H. Kotera, "Micro cell encapsulation and its hydrogel-beads production using microfluidic device," *Microsystem Technologies*, vol. 13, pp. 951–958, May 2007.

[29] M. Chabert and J.-L. Viovy, "Microfluidic high-throughput encapsulation and hydrodynamic self-sorting of single cells," *PNAS*, vol. 105, pp. 3191–3196, Mar. 2008.

[30] T. Konry, M. Dominguez-Villar, C. Baecher-Allan, D. A. Hafler, and M. Yarmush, "Droplet-based microfluidic platforms for single t cell secretion analysis of IL-10 cytokine," *Biosensors and Bioelectronics*, vol. 26, pp. 2707–2710, Jan. 2011.

[31] X. Zhang, A. Ohta, and D. Garmire, "Rapid monodisperse microencapsulation of single cells," in *Engineering in Medicine and Biology Society (EMBC), 2010 Annual International Conference of the IEEE*, pp. 6518–6521, 2010.

[32] J. W. Swanson, J. E. Lebeau, J. W. Swanson, and J. E. Lebeau, "The effect of implantation on the physical properties of silicone rubber, the effect of implantation on the physical properties of silicone rubber," *Journal of Biomedical Materials Research, Journal of Biomedical Materials Research*, vol. 8, 8, pp. 357, 357–367, 367, Nov. 1974.

[33] M. W. Toepke and D. J. Beebe, "PDMS absorption of small molecules and consequences in microfluidic applications," *Lab on a Chip*, vol. 6, no. 12, p. 1484, 2006.

[34] J. N. Lee, C. Park, and G. M. Whitesides, "Solvent compatibility of poly(dimethylsiloxane)-based microfluidic devices," *Anal. Chem.*, vol. 75, no. 23, pp. 6544–6554, 2003.

[35] Y. S. Heo, L. M. Cabrera, J. W. Song, N. Futai, Y.-C. Tung, G. D. Smith, and S. Takayama, "Characterization and resolution of evaporation-mediated osmolality shifts that constrain microfluidic cell culture in poly(dimethylsiloxane) devices," *Anal. Chem.*, vol. 79, no. 3, pp. 1126–1134, 2006.

[36] M. A. Eddings, M. A. Johnson, and B. K. Gale, "Determining the optimal PDMSPDMS bonding technique for microfluidic devices," *Journal of Micromechanics and Microengineering*, vol. 18, p. 067001, June 2008.

[37] A. M. Christensen, D. A. Chang-Yen, and B. K. Gale, "Characterization of interconnects used in PDMS microfluidic systems," *Journal of Micromechanics and Microengineering*, vol. 15, no. 5, pp. 928–934, 2005.

[38] M. L. Kovarik and S. C. Jacobson, "Attoliter-scale dispensing in nanofluidic channels," *Anal. Chem.*, vol. 79, no. 4, pp. 1655–1660, 2007.

[39] Y. S. Shin, K. Cho, S. H. Lim, S. Chung, S.-J. Park, C. Chung, D.-C. Han, and J. K. Chang, "PDMS-based micro PCR chip with parylene coating," *Journal of Micromechanics and Microengineering*, vol. 13, pp. 768–774, Sept. 2003.

[40] G. T. Roman, T. Hlaus, K. J. Bass, T. G. Seelhammer, and C. T. Culbertson, "SolGel modified poly(dimethylsiloxane) microfluidic devices with high electroosmotic mobilities and hydrophilic channel wall characteristics," *Anal. Chem.*, vol. 77, no. 5, pp. 1414–1422, 2005.

[41] C. Ahn, J.-W. Choi, G. Beaucage, J. Nevin, J.-B. Lee, A. Puntambekar, and J. Lee, "Disposable smart lab on a chip for point-of-care clinical diagnostics," *Proceedings of the IEEE*, vol. 92, pp. 154 – 173, Jan. 2004.

[42] D. A. Mair, E. Geiger, A. P. Pisano, J. M. J. Frechet, and F. Svec, "Injection molded microfluidic chips featuring integrated interconnects," *Lab on a Chip*, vol. 6, no. 10, pp. 1346–1354, 2006.

[43] S. Kaka, R. K. Shah, and W. Aung, *Handbook of single-phase convective heat transfer*. Wiley, Oct. 1987.

[44] T. Ahmad and I. Hassan, "Experimental analysis of microchannel entrance length characteristics using microparticle image velocimetry," *Journal of Fluids Engineering*, vol. 132, no. 4, p. 041102, 2010.

[45] C. L. Wiginton and C. Dalton, "Incompressible laminar flow in the entrance region of a rectangular duct," *Journal of Applied Mechanics*, vol. 37, no. 3, pp. 854–856, 1970.

[46] M. Renksizbulut and H. Niazmand, "Laminar flow and heat transfer in the entrance region of trapezoidal channels with constant wall temperature," *Journal of Heat Transfer*, vol. 128, no. 1, pp. 63–74, 2006.

[47] M. Weiss, M. Hug, T. Neff, and J. Fischer, "Syringe size and flow rate affect drug delivery from syringe pumps," *Canadian Journal of Anesthesia / Journal canadien d'anesthsie*, vol. 47, no. 10, pp. 1031–1035, 2000.

[48] D. F. Capes, K. R. Dunster, V. B. Sunderland, D. McMillan, P. B. Colditz, and C. McDonald, "Fluctuations in syringe-pump infusions: association with blood pressure variations in infants," *American journal of health-system pharmacy*, vol. 52, pp. 1646–1653, Aug. 1995. PMID: 7583827.

[49] R. Ferrari and D. Beech, "Infusion pumps: guidelines and pitfalls," 1995.

[50] M. Weiss, O. Bnziger, T. Neff, and S. Fanconi, "Influence of infusion line compliance on drug delivery rate during acute line loop formation," *Intensive Care Medicine*, vol. 26, no. 6, pp. 776–779, 2000.

[51] Z. Xia, H. L. Goldsmith, and T. G. van de Ven, "Kinetics of specific and nonspecific adhesion of red blood cells on glass," *Biophysical journal*, vol. 65, pp. 1073–1083, Sept. 1993. PMID: 8241388.

[52] M. Heckele and W. K. Schomburg, "Review on micro molding of thermoplastic polymers," *Journal of Micromechanics and Microengineering*, vol. 14, pp. R1–R14, Mar. 2004.

[53] H. Becker and C. Gartner, "Polymer microfabrication methods for microfluidic analytical applications," *Electrophoresis*, vol. 21, pp. 12–26, Jan. 2000.

[54] J. Rossier, F. Reymond, and P. E. Michel, "Polymer microfluidic chips for electrochemical and biochemical analyses," *Electrophoresis*, vol. 23, pp. 858–867, Mar. 2002.

[55] C. G., L. S.M., and L. M., "Polydimethylsiloxane thermal degradation part 1. kinetic aspects," *Polymer*, vol. 42, no. 6, pp. 2395–2402, 2001.

[56] J.-H. Chang, F.-S. Cheng, C.-C. Chao, Y.-C. Weng, S.-Y. Yang, and L. A. Wang, "Direct imprinting using soft mold and gas pressure for large area

and curved surfaces," *Journal of Vacuum Science & Technology A: Vacuum, Surfaces, and Films*, vol. 23, pp. 1687–1690, Nov. 2005.

[57] G. S. Fiorini, G. D. M. Jeffries, D. S. W. Lim, C. L. Kuyper, and D. T. Chiu, "Fabrication of thermoset polyester microfluidic devices and embossing masters using rapid prototyped polydimethylsiloxane molds," *Lab on a Chip*, vol. 3, no. 3, pp. 158–163, 2003.

[58] J. Narasimhan and I. Papautsky, "Polymer embossing tools for rapid prototyping of plastic microfluidic devices," *Journal of Micromechanics and Microengineering*, vol. 14, pp. 96–103, Jan. 2004.

[59] W. M. Choi and O. O. Park, "The fabrication of submicron patterns on curved substrates using a polydimethylsiloxane film mould," *Nanotechnology*, vol. 15, pp. 1767–1770, Dec. 2004.

[60] Y. Luo, Z. Zhang, X. Wang, and Y. Zheng, "Ultrasonic bonding for thermoplastic microfluidic devices without energy director," *Microelectronic Engineering*, vol. 87, pp. 2429–2436, Nov. 2010.

[61] R. Truckenmller, R. Ahrens, Y. Cheng, G. Fischer, and V. Saile, "An ultrasonic welding based process for building up a new class of inert fluidic microsensors and -actuators from polymers," *Sensors and Actuators A: Physical*, vol. 132, pp. 385–392, Nov. 2006.

[62] D. A. Mair, E. Geiger, and A. P. Pisano, "Fr chet, JMJ, and svec, f," *Lab Chip*, vol. 6, p. 13461354, 2006.

[63] C. W. Tsao, L. Hromada, J. Liu, P. Kumar, and D. L. DeVoe, "Low temperature bonding of PMMA and COC microfluidic substrates using UV/ozone surface treatment," *Lab on a Chip*, vol. 7, no. 4, p. 499, 2007.

[64] Y. Liu, D. Ganser, A. Schneider, R. Liu, P. Grodzinski, and N. Kroutchinina, "Microfabricated polycarbonate CE devices for DNA analysis," *Analytical Chemistry*, vol. 73, no. 17, pp. 4196–4201, 2001.

[65] J. Kestin, M. Sokolov, and W. A. Wakeham, "Viscosity of liquid water in the range -8C to 150C," *J. Phys. Chem. Ref. Data*, vol. 7, no. 3, pp. 941–948, 1978.

[66] J. H. Xu, S. W. Li, W. J. Lan, and G. S. Luo, "Microfluidic approach for rapid interfacial tension measurement," *Langmuir*, vol. 24, no. 19, pp. 11287–11292, 2008.

[67] C. Pigot and A. Hibara, "Surface tension measurement at the microscale by passive resonance of capillary waves," *Anal. Chem.*, 2012.

[68] S. D. Hudson, J. T. Cabral, W. J. Goodrum, K. L. Beers, and E. J. Amis, "Microfluidic interfacial tensiometry," *Applied Physics Letters*, vol. 87, pp. 081905–081905–3, Aug. 2005.

[69] H. Gu, M. H. Duits, and F. Mugele, "Interfacial tension measurements with microfluidic tapered channels," *Colloids and Surfaces A: Physicochemical and Engineering Aspects*, vol. 389, pp. 38–42, Sept. 2011.

[70] J. D. Martin, J. N. Marhefka, K. B. Migler, and S. D. Hudson, "Interfacial rheology through microfluidics," *Advanced Materials*, vol. 23, pp. 426–432, Jan. 2011.

[71] M. L. J. Steegmans, A. Warmerdam, K. G. P. H. Schroen, and R. M. Boom, "Dynamic interfacial tension measurements with microfluidic y-junctions," *Langmuir*, vol. 25, no. 17, pp. 9751–9758, 2009.

[72] F. Bashforth and J. C. Adams, *An attempt to test the theories of capillary action: by comparing the theoretical and measured forms of drops of fluid.* University Press, 1883.

[73] J. Andreas, E. Hauser, and W. Tucker, "Boundary tension by pendant dropts," *J. Phys. Chem.*, vol. 42, no. 8, pp. pp 1001–1019, 1938.

[74] L. R. Fisher, E. E. Mitchell, and N. S. Parker, "Interfacial tensions of commercial vegetable oils with water," *Journal of Food Science*, vol. 50, no. 4, pp. 1201–1202, 1985.

[75] J. Berthier and P. Silberzan, *Microfluidics for Biotechnology.* Artech House, Dec. 2009.

[76] O. Breslouer, "Droplet breakup of falling jet," final report, Princeton University, Jan. 2010.

[77] L. Mntrier-Deremble and P. Tabeling, "Droplet breakup in microfluidic junctions of arbitrary angles," *Physical Review E*, vol. 74, no. 3, p. 035303, 2006.

[78] S.-Y. Teh, R. Lin, L.-H. Hung, and A. P. Lee, "Droplet microfluidics," *Lab on a Chip*, vol. 8, no. 2, pp. 198–220, 2008.

[79] P. C.-H. Chan and L. G. Leal, "The motion of a deformable drop in a second-order fluid," *Journal of Fluid Mechanics*, vol. 92, no. 01, pp. 131–170, 1979.

[80] R. B. Brown and J. Audet, "Current techniques for single-cell lysis," *Journal of The Royal Society Interface*, vol. 5, pp. S131–S138, Oct. 2008.

[81] A. Zarrine-Afsar and S. N. Krylov, "Use of capillary electrophoresis and endogenous fluorescent substrate to monitor intracellular activation of protein kinase a," *Anal. Chem.*, vol. 75, no. 15, pp. 3720–3724, 2003.

[82] D. Irimia, R. G. Tompkins, and M. Toner, "Single-cell chemical lysis in picoliter-scale closed volumes using a microfabricated device," *Anal. Chem.*, vol. 76, no. 20, pp. 6137–6143, 2004.

[83] Z. Pang, A. AlMahrouki, M. Berezovski, and S. N. Krylov, "Selection of surfactants for cell lysis in chemical cytometry to study proteinDNA interactions," *Electrophoresis*, vol. 27, pp. 1489–1494, Apr. 2006.

[84] M. V. Berezovski, T. W. Mak, and S. N. Krylov, "Cell lysis inside the capillary facilitated by transverse diffusion of laminar flow profiles (TDLFP)," *Analytical and Bioanalytical Chemistry*, vol. 387, pp. 91–96, Oct. 2006.

[85] R. B. Brown and J. Audet, "Sampling efficiency of a single-cell capillary electrophoresis system," *Cytometry. Part A*, vol. 71, pp. 882–888, Oct. 2007. PMID: 17680706.

[86] C. E. Sims, G. D. Meredith, T. B. Krasieva, M. W. Berns, B. J. Tromberg, and N. L. Allbritton, "LaserMicropipet combination for single-cell analysis," *Anal. Chem.*, vol. 70, no. 21, pp. 4570–4577, 1998.

[87] H. Li, C. E. Sims, H. Y. Wu, and N. L. Allbritton, "Spatial control of cellular measurements with the laser micropipet," *Anal. Chem.*, vol. 73, no. 19, pp. 4625–4631, 2001.

[88] K. R. Rau, P. A. Quinto-Su, A. N. Hellman, and V. Venugopalan, "Pulsed laser microbeam-induced cell lysis: Time-resolved imaging and analysis of hydrodynamic effects," *Biophysical Journal*, vol. 91, pp. 317–329, July 2006. PMID: 16617076 PMCID: 1479069.

[89] L. C. Waters, S. C. Jacobson, N. Kroutchinina, J. Khandurina, R. S. Foote, and J. M. Ramsey, "Microchip device for cell lysis, multiplex PCR amplification, and electrophoretic sizing," *Analytical Chemistry*, vol. 70, pp. 158–162, Jan. 1998. PMID: 9463271.

[90] C. Ke, A.-M. Kelleher, H. Berney, M. Sheehan, and A. Mathewson, "Single step cell lysis/PCR detection of escherichia coli in an independently controllable silicon microreactor," *Sensors and Actuators B: Chemical*, vol. 120, pp. 538–544, Jan. 2007.

[91] N. Privorotskaya, Y.-S. Liu, J. Lee, H. Zeng, J. A. Carlisle, A. Radadia, L. Millet, R. Bashir, and W. P. King, "Rapid thermal lysis of cells using silicondiamond microcantilever heaters," *Lab Chip*, vol. 10, pp. 1135–1141, Mar. 2010.

[92] H. Zhang and W. Jin, "Determination of different forms of human interferon-gamma in single natural killer cells by capillary electrophoresis with on-capillary immunoreaction and laser-induced fluorescence detection," *Electrophoresis*, vol. 25, pp. 1090–1095, Apr. 2004. PMID: 15095451.

[93] U. Zimmermann, "Electrical breakdown, electropermeabilization and electrofusion," *Reviews of physiology, biochemistry and pharmacology*, vol. 105, pp. 176–256, 1986. PMID: 3541139.

[94] B. Gabriel and J. Teissi, "Time courses of mammalian cell electropermeabilization observed by millisecond imaging of membrane property changes during the pulse," *Biophysical Journal*, vol. 76, pp. 2158–2165, Apr. 1999.

[95] F. Han, Y. Wang, C. E. Sims, M. Bachman, R. Chang, G. P. Li, and N. L. Allbritton, "Fast electrical lysis of cells for capillary electrophoresis," *Anal. Chem.*, vol. 75, no. 15, pp. 3688–3696, 2003.

[96] S.-W. Lee and Y.-C. Tai, "A micro cell lysis device," *Sensors and Actuators A: Physical*, vol. 73, pp. 74–79, Mar. 1999.

[97] K.-Y. Lu, A. M. Wo, Y.-J. Lo, K.-C. Chen, C.-M. Lin, and C.-R. Yang, "Three dimensional electrode array for cell lysis via electroporation," *Biosensors and Bioelectronics*, vol. 22, pp. 568–574, Oct. 2006.

[98] N. R. Munce, J. Li, P. R. Herman, and L. Lilge, "Microfabricated system for parallel single-cell capillary electrophoresis," *Anal. Chem.*, vol. 76, no. 17, pp. 4983–4989, 2004.

[99] R. M. Hochmuth, N. Mohandas, and P. L. Blackshear, "Measurement of the elastic modulus for red cell membrane using a fluid mechanical technique," *Biophysical Journal*, vol. 13, pp. 747–762, Aug. 1973. PMID: 4726877 PMCID: PMC1484338.